

Development of an improved State-of-Charge Sensor  
for the All-Vanadium Redox Flow Battery

Dissertation  
zur Erlangung des Grades  
des Doktors der Naturwissenschaften  
der Naturwissenschaftlich-Technischen Fakultät  
der Universität des Saarlandes

von  
Jan Nicholas Geiser

Saarbrücken  
2019

---

---

---

Tag des Kolloquiums: 11.09.2019

Dekan: Prof. Dr. Guido Kickelbick

Berichterstatter: Prof. Dr. Dr. h.c. Rolf Hempelmann  
Prof. Dr. Michael Springborg

Vorsitz: Prof. Dr. Christopher Kay

Akad. Mitarbeiter: Dr. Bernd Morgenstern

---

---

---

*Learn from yesterday, live for today, hope for tomorrow.*

*The important thing is not to stop questioning.*

**Albert Einstein**

---

---

---

## Abstract

A solution to balance the fluctuating renewable electricity generation is the application of stationary energy storages like the all-vanadium redox flow battery (VRFB). In the VRFB the electric energy is chemically stored using vanadium redox couples in both half-cell electrolytes. Crucial potential for improvement is located in the determination of the battery's state-of-charge (SOC). Thus, two approaches for improved in-situ state-of-charge sensing in the VRFB are presented. Therein, central aspects are the half-cell and oxidation state specific SOC monitoring as well as the sensor's long-term use. One approach applies potentiometric titration coupled with UV/Vis/NIR spectroscopy. Several  $V^{2+}$  solutions within the total vanadium concentration range of  $0.2 \text{ mol L}^{-1}$  to  $1.6 \text{ mol L}^{-1}$  are titrated with  $0.2 \text{ mol L}^{-1}$   $\text{KMnO}_4$  solution. With simultaneously conducted in-situ UV/Vis/NIR spectroscopy the absorption coefficients of  $V^{2+}$  at  $\lambda = 850 \text{ nm}$  and  $V^{3+}$  at  $\lambda = 400 \text{ nm}$  are obtained by fitting the related absorption maxima. Hence, the  $V^{2+}$  and  $V^{3+}$  concentrations and the anolyte's SOC are accessible. In the other approach the in-situ open-circuit-voltage (OCV) measurements of a pristine  $1.6 \text{ mol L}^{-1}$  VRFB electrolyte are related to SOC via a Nernst-based fit. Then, in-situ UV/Vis/NIR spectroscopy is calibrated to SOC with the SOC-related OCV values. Thus, via photometry the SOC of both VRFB anolyte ( $V^{3+}$  at  $\lambda = 400 \text{ nm}$ ) and catholyte ( $V^{5+}$  at  $\lambda = 440 \text{ nm}$ ) can be monitored separately and in-operando.

---

---

---

## Zusammenfassung

Stationäre Energiespeicher wie die All-Vanadium Redox Flow Batterie (VRFB) ermöglichen die Ausbalancierung der fluktuierenden Stromerzeugung durch erneuerbare Energien. In der VRFB wird die elektrische Energie chemisch in den Vanadium-Redoxpaaren der Halbzellen-Elektrolyte gespeichert. Deutliches Verbesserungspotential liegt bei der Bestimmung des State-of-Charge (SOC). Daher werden zwei Ansätze zur verbesserten SOC-Detektion in der VRFB präsentiert. Zentrale Aspekte sind neben halbzellen- und oxidationszustandsspezifischen SOC-Messungen auch die Sensor-Langzeitstabilität. Ein Ansatz kombiniert hierfür potentiometrische Titration mit UV/Vis/NIR-Spektroskopie.  $V^{2+}$ -Lösungen mit einer Gesamtvanadiumkonzentration zwischen  $0,2 \text{ mol L}^{-1}$  und  $1,6 \text{ mol L}^{-1}$  werden mit  $0,2 \text{ mol L}^{-1}$   $\text{KMnO}_4$ -Lösung titriert. Mit simultaner in-situ UV/Vis/NIR-Spektroskopie werden die Absorptionskoeffizienten von  $V^{2+}$  bei  $\lambda = 850 \text{ nm}$  und  $V^{3+}$  bei  $\lambda = 400 \text{ nm}$  durch Fitten ihrer Absorptionsmaxima bestimmt. Dadurch werden die  $V^{2+}$ - und  $V^{3+}$ -Konzentrationen und der SOC im Anolyt erhalten. Im anderen Ansatz werden die in-situ Open-Circuit-Voltage-Messungen (OCV) in balanciertem  $1,6 \text{ mol L}^{-1}$  VRFB-Elektrolyt mit einem auf der Nernst-Gleichung basierenden Fit SOC-verknüpft. Dann wird die in-situ UV/Vis/NIR-Spektroskopie mit den SOC-verknüpften OCV-Werten auf SOC kalibriert. Folglich ist die photometrische SOC-Bestimmung im VRFB-Betrieb und separat für den Anolyt ( $V^{3+}$  bei  $\lambda = 400 \text{ nm}$ ) und Katholyt ( $V^{5+}$  bei  $\lambda = 440 \text{ nm}$ ) möglich.

---

---

---

## Contents

<b>Abstract .....</b>	<b>vii</b>
<b>Zusammenfassung .....</b>	<b>ix</b>
<b>1. Introduction.....</b>	<b>1</b>
1.1 Present situation and challenges .....	1
1.2 General composition and aims of the project “OptiCharge” .....	4
<b>2. Theory section .....</b>	<b>7</b>
2.1 General aspects of redox flow batteries .....	7
2.2 The all-vanadium redox flow battery .....	9
2.2.1 Operating principle .....	9
2.2.2 Electrode material .....	11
2.2.3 Bipolar plate material.....	12
2.2.4 Ion-selective membranes .....	13
2.3 VRFB-Electrolyte .....	14
2.3.1 Vanadium chemistry in aqueous solution .....	14
2.3.2 Common vanadium sources.....	17
2.3.3 Vanadium electrolyte production .....	18
2.3.4 Vanadium species solubilities and their impact on electrolyte composition.....	20
2.4 Definition of the State-of-Charge .....	22
2.5 State-of-the-art SOC determination techniques .....	23
2.5.1 Electrochemical techniques.....	24
2.5.2 Optical strategies .....	26
2.5.3 Additional approaches.....	29
2.6 Research objective.....	30
<b>3. In-situ spectrometric State-of-Charge determination.....</b>	<b>31</b>
<b>3.1 Experimental.....</b>	<b>31</b>
3.1.1 Electrolyte .....	31
3.1.2 Membrane.....	31
3.1.3 Electrode felts and current collectors.....	32
3.1.4 Construction material .....	32

---

3.1.5	VRFB single cell.....	32
3.1.6	Laboratory VRFB set-up.....	33
3.1.7	UV/Vis/NIR spectroscopic set-up.....	35
<b>3.2</b>	<b>Results and discussion .....</b>	<b>36</b>
3.2.1	Description of OCV values with the Nernst equation .....	36
3.2.2	SOC determination for the negative half-cell of the VRFB .....	41
3.2.3	SOC determination for the positive half-cell of the VRFB .....	45
3.2.4	Conclusion .....	48
<b>4.</b>	<b>Potentiometric titration coupled in-situ spectroscopy.....</b>	<b>49</b>
<b>4.1</b>	<b>Experimental.....</b>	<b>49</b>
4.1.1	Electrolyte .....	49
4.1.2	Spectroscopic coupled potentiometric titration set-up.....	50
<b>4.2</b>	<b>Results and discussion .....</b>	<b>52</b>
4.2.1	Potential measurements during the titration .....	52
4.2.2	Simultaneous in-situ UV/Vis/NIR spectroscopy .....	57
4.2.3	Clear assignment of potential measurements to UV/Vis/NIR spectral data.....	70
4.2.4	Determination of species-specific absorption coefficients.....	71
4.2.5	Conclusions .....	78
<b>5.</b>	<b>Comparison of both techniques.....</b>	<b>79</b>
<b>6.</b>	<b>Summary and outlook.....</b>	<b>81</b>
<b>7.</b>	<b>References .....</b>	<b>85</b>
<b>8.</b>	<b>Appendix .....</b>	<b>93</b>
<b>A.</b>	<b>List of figures.....</b>	<b>93</b>
<b>B.</b>	<b>List of abbreviations.....</b>	<b>97</b>
<b>C.</b>	<b>Scientific publications.....</b>	<b>99</b>
	<b>Acknowledgements .....</b>	<b>101</b>

---

---

---



# 1. Introduction

## 1.1 Present situation and challenges

In the Climate Change Report published by the Intergovernmental Panel on Climate Change (IPCC) in 1992 cause analysis for the evolution of the global climatic conditions was conducted. Therein, greenhouse gases, such as carbon dioxide (CO<sub>2</sub>), chlorofluorocarbons (CFC), ozone (O<sub>3</sub>) and methane (CH<sub>4</sub>) are identified as originators for increased global absorption of solar radiation [1]. Due to their mode of action, a larger share of the heat produced by the solar radiation absorption is retained on the terrestrial surface and in the atmosphere compared to the absence of the greenhouse gases. This phenomenon, which partly prevents the heat's release from earth and consequently furthers a continuous atmospheric temperature increase, is also referred to as the greenhouse effect. International efforts are made to reverse or at least reduce the greenhouse effect as trigger of the global warming and the subsequently induced climate change [1].

In case of the German ecopolitical orientation, a national energy transition from fossil fuels like coal, lignite and natural gas towards renewable energy sources (e.g. solar, wind, biomass and hydro power) is in progress. This energy transition is usually denoted as the German Energiewende. One of the central objectives of the German Energiewende is a continuously progressing decarbonization of the energy generation [2]. This CO<sub>2</sub>-free energy production is regarded as an essential contribution to limit global warming and climate change respectively. Therefore, a proportion of 50 percent of the German gross electricity consumption is aimed at to be covered by renewable energies until 2030. This share should be increased to 80 percent by 2050 according to the Federal Ministry for Economic Affairs and Energy (Bundesministerium für Wirtschaft und Energie, BMWi) [2].

Beginning at 3.4 % share in 1990, the amount of renewables was strongly elevated to 36.2 % at the end of the year 2017. Thus, during the period from 1990 until 2017, the renewable electricity share with respect to Germany's gross electricity consumption was increased more than tenfold (see Fig. 1, above) [3]. For this purpose, solar, wind and biomass electricity generation were extended. Solely the hydro power remained at the same level as indicated in 1990. Within the last 27 years, the gross electricity generation increased from 18.9 billion kilowatt hours (kWh) to 217.9 billion kWh (see Fig. 1, below) [3].

Thus, substantial expansions of solar power plants and wind turbines have been progressed. A principal challenge of these renewables is their fluctuating energy supply depending on the daytime, the season and the weather [4,5]. For proper functionality of the electrical grid, electricity supply and demand must be temporally and spatially harmonized. The intensified use of renewable energies is leading to a rising demand of flexibility in the grids. Consequently, the average discrepancy between electricity supply and demand is increasing. Traditionally, the excess or lack of electric energy is compensated by balancing power. These measures have to be initiated in the short term. Additionally, a spacial compensation has to proceed, because generally renewable electricity generation and demand are distributed differently across the German federal territory [6].

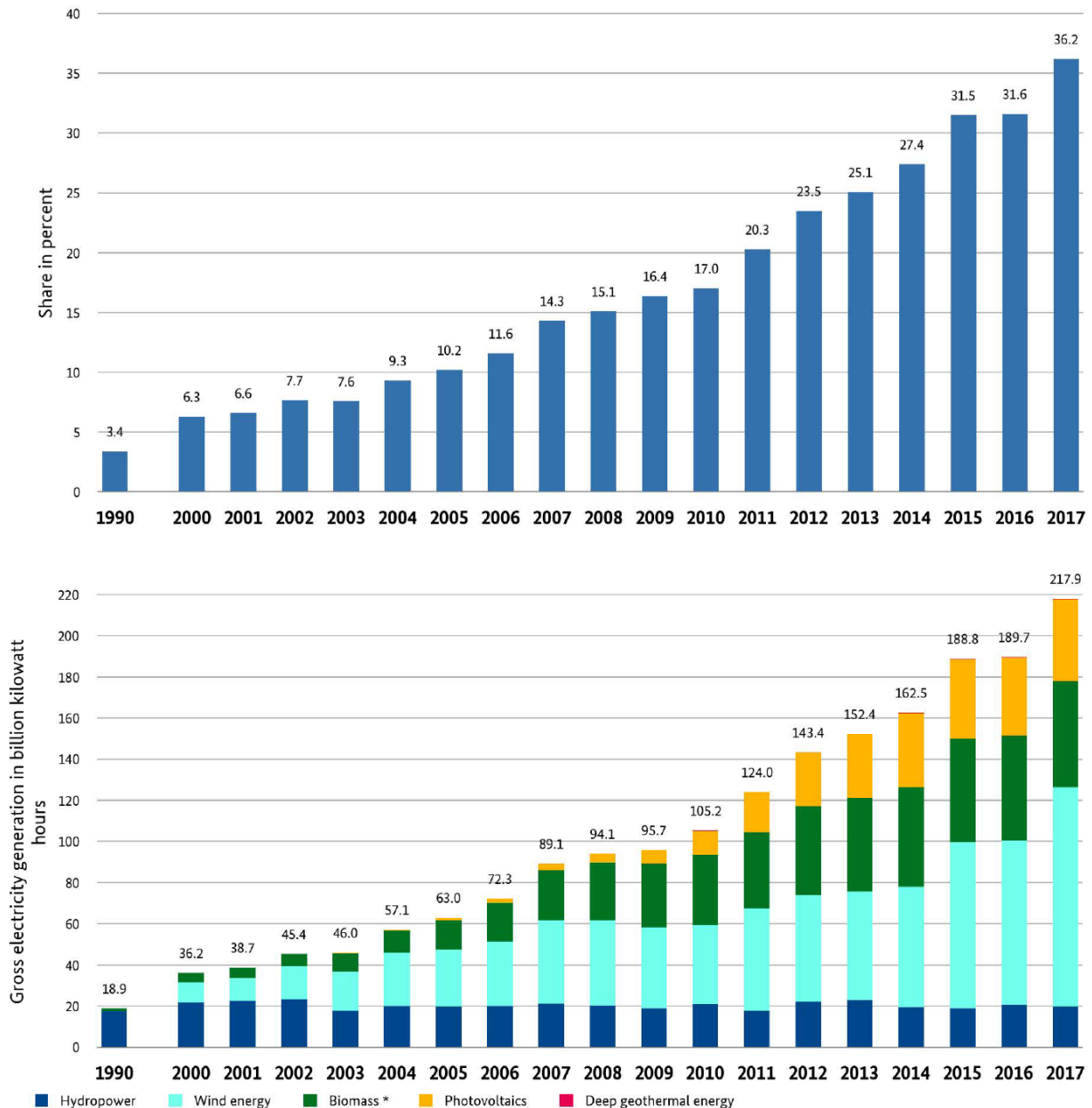


Fig. 1. Development of the renewable energy share of the gross electricity consumption in Germany (above), contributions of the miscellaneous renewable sources (below) [3].

While the need of flexibility is steadily increasing due to every new renewable power plant which is connected to the electric network the amount of possibilities for grid balancing is decreasing. The reason for the decreasing balancing capacities is the shutdown of fossil power plants due to the CO<sub>2</sub> reduction targets of the German Energiewende. Insufficient balancing capabilities will lead to considerable problems like temporal interruptions or complete breakdowns of the power supply [7]. To prevent these malfunctions the application of temporary energy storage systems is necessary [8-9]. Depending on the scope of electrical energy storages (EES) two different types of tasks can be generally distinguished with regard to load levelling/peak shaving and seasonal energy storage.

The profile of requirements concerning load levelling/peak shaving applications includes a high energy efficiency of the battery system. Additionally, a high power density of the energy storage media and the support of frequent deep discharges are necessary. Compromises like only medium capacity as well as moderate self-discharge are tolerable in case of this certain application. Contrarily, seasonal energy storages request large storage capacities combined with a minimal self-discharge. Less important are a medium energy efficiency and power density. Compared to the peak shaving procedure the occurrence of deep discharges is much rarer [10]. Electrical energy storage technologies can be divided in potential energy storages (pumped hydro, compressed air), kinetic energy storage systems (flywheels) and electrochemical systems like batteries or flow cells [11]. Among different types of traditional potential or kinetic energy storages, novel electrochemical systems like flow batteries are investigated as promising technology. As a prominent representative, the all-vanadium redox flow battery (VRFB) exhibits the ability to function as seasonal energy storage [12-13]. One potential area of application is e.g. as a buffer for small grids [14].

Furthermore, traffic exhaust gases contribute a considerable share to the worldwide CO<sub>2</sub> emissions and to the air pollution in general. Thus, another part of the decarbonization process of the German Energiewende is the continuous replacement of fossil-fueled cars powered by gasoline or diesel engines with electrically driven vehicles. Since the last 27 years, a continuously growing amount of greenhouse gas emission has been avoided, starting with 27.8 million tons of CO<sub>2</sub>-equivalents in 1990 and reaching 178.6 million tons of CO<sub>2</sub>-equivalents in 2017 (see Fig. 2) [3]. Beside the significant CO<sub>2</sub>-reduction in the electricity generation, the heat sector and especially the transport sector exhibit elevated CO<sub>2</sub>-reduction potential. Only a small, but continuously increasing proportion of the transport is powered by renewable electricity so far. Consequently, a significantly greater reduction of transport related greenhouse gases can be realized as a substantial part to meet the German decarbonisation targets.

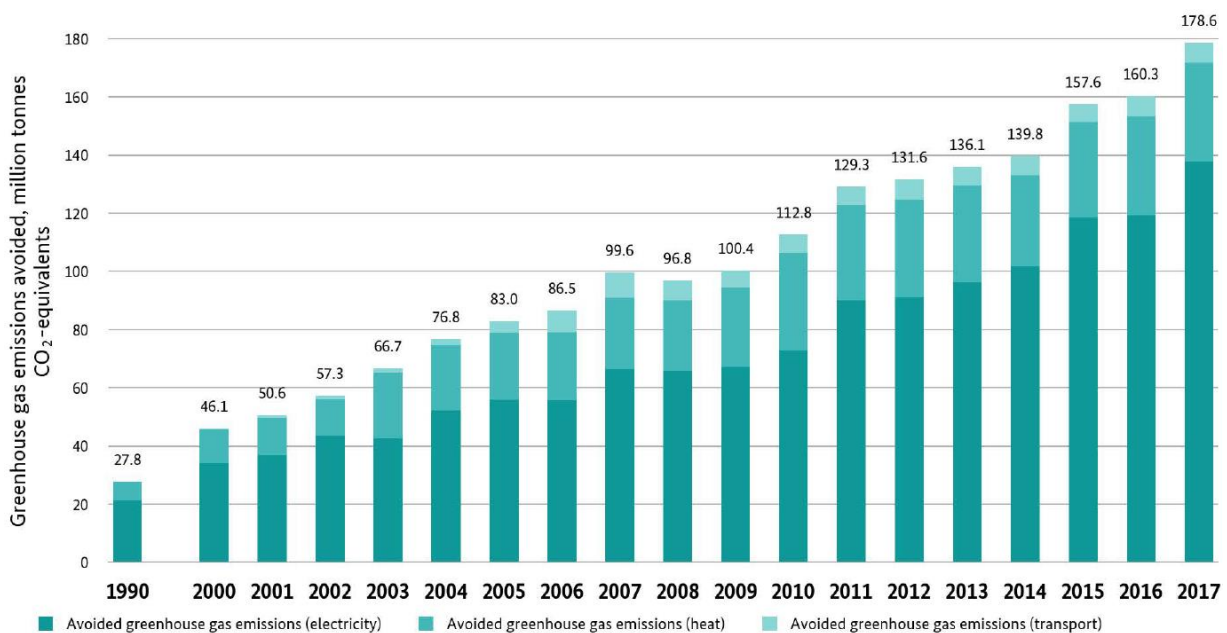


Fig. 2. Evolution of avoided greenhouse gas emissions by means of renewable energies [3].

The expected market launch for electric cars within the next decade will entail an increasing demand for recharging capacities. This challenge is combined with a heightened load of the grid due to fast charging of the electric vehicles (EVs) [15]. In this case, the surplus renewable energy obtained by peak shaving can be beneficially utilized for recharging the EVs with green electricity. Flow batteries like the VRFB can be applied as a connecting link for load balancing between the electrical grid and the charging stations. Thus, they can reduce the strain on the grid and consequently prevent its malfunction until it is reinforced [16-17]. Combined with a sufficient power output of renewable energy sources the VRFBs are able to release their dependency on the power from the grid. Consequently, the establishment of insular solutions for electricity storage and delivery, e. g. uninterruptable power supplies as well as insular charging stations becomes feasible [18]. Besides continuing research, numerous VRFB storage units have already been installed around the globe during the last decade, inter alia in Asia, Europe and the US [19].

### **1.2 General composition and aims of the project “OptiCharge”**

Within the framework of the project “OptiCharge” a quasi-autarchic, regeneratively powered EV solar charging station combined with a VRFB electric energy storage buffer solution is investigated. The project affiliated activities comprise conception, construction, operation and optimization of the charging station infrastructure. “OptiCharge” is funded by the Federal Ministry for Economic Affairs and Energy (Bundesministerium für Wirtschaft und Energie, BMWi) due to a decision of the German Bundestag. The technical and administrative supervision of the project “OptiCharge” is performed by the institution Projekträger Jülich (PtJ).

In the interdisciplinary cooperation the subsequent project partners have participated:

- Institut für ZukunftsEnergie- und Stoffstromsysteme gGmbH (IZES)
- SCHMID Group GmbH – SCHMID Energy Systems GmbH (SCHMID)
- Technical University of Kaiserslautern – Junior professorship for Electromobility
- Saarland University – Transfercenter Sustainable Electrochemistry

Besides of being in charge of the project management, IZES is responsible for the assembly, monitoring and operation of the pilot plant. The computer-based modeling and simulation concerning the test facility are conducted to develop methods for conception and dimensioning of future EV charging solutions. Furthermore, the supply of the EVs for test purposes, the EV related data acquisition and the reservation system are within the competence of IZES.

The construction of the VRFB system and the technical implementation of the associated enhanced components and materials are undertaken by SCHMID. The Junior professorship for Electromobility is developing the related algorithms for prediction and control concerning the operation of the VRFB equipped charging station. Thus, the experiences and functionalities obtained by means of these algorithms, like an advanced battery management system (BMS), are used to improve the simultaneously developed overall energy management system (EMS).

The Transfercenter Sustainable Electrochemistry is focused on the chemical issues of the project. Central working fields are covering the functional materials and the additional performance relevant components of the VRFB. Therefore, the research is addressing the further improvement and evaluation of the membranes and electrode materials. Furthermore, a novel improved state-of-charge (SOC) sensor has been developed to determine accurate SOC values of the VRFB. Due to the access to these enhanced state-of-charge estimations, more detailed insights into the VRFB electrolyte's chemical condition are facilitated. Thus, based on these valid pieces of information, the resulting decisions of the energy management system will increase both the entire VRFB efficiency and durability.

Since its completion in autumn 2017 the overall system is situated at the location of the IZES gGmbH in Saarbrücken/Burbach in Germany. An outer impression of the "OptiCharge" station is given in Fig. 3. Concerning its general design, the EV charging station consists of a carport equipped with 48 solar panels (surface area ca. 61 m<sup>2</sup>) providing approximately 10 kW peak. Below the carport, four charging points with parking lots are situated. Excess photovoltaic energy due to the fluctuating solar power generation is stored in a VRFB system (battery power: 30 kW, battery capacity: 100 kWh) equipped with a battery management system.

The system components are interlinked with each other and supervised by the advanced energy management system. During operation, the EMS evaluates the data of the system components like the present photovoltaic output power, the status of the VRFB supplied by the BMS and the current as well as the future energy demands of the customers. In the following, the EMS optimizes the EV charging procedure with respect to the maximization of the share of directly used solar energy. Consequently, events of unnecessary application of the VRFB are minimized to avoid losses referring to energy conversions.



*Fig. 3. EV charging station "OptiCharge" at Saarbrücken/Burbach in Germany [20].*

As outlined before, for the efficient VRFB operation the knowledge of the battery's state-of-charge is of crucial interest. To ensure reliable SOC monitoring the determination of the half-cell specific as well as the vanadium species specific state-of-charge is required. Besides, the used SOC sensor's part with direct contact to the vanadium electrolyte has to be long-term resistant in this chemically aggressive environment. To address these demands, this PhD thesis is focused on the development of an improved state-of-charge sensor. Therefore, two different approaches are discussed in this dissertation. The first approach combines in-situ UV/Vis/NIR absorbance spectrometry with in-situ open-circuit-voltage measurements for in-operando partial SOC monitoring. Besides, the second approach is dealing with potentiometric titration coupled with simultaneously conducted UV/Vis/NIR absorbance spectroscopy for the determination of the vanadium species specific absorption coefficients. A detailed introduction of the latter is given in chapter 2.6.

## 2. Theory section

### 2.1 General aspects of redox flow batteries

In contrast to other commonly applied accumulators, redox flow batteries (RFB) use liquid chemical energy carriers instead of solid-state storages like i.e. lithium ion batteries [21-22]. Two solutions of liquid energy carrier containing the electrochemical active species, usually called electrolytes, are stored separately from the RFB energy converter unit in external tanks [22-23]. The RFB energy converter single cell (lab size) consists of two half-cells with flow-through electrodes separated by an ion-selective polymeric membrane to ensure charge balancing and to prevent electrolyte cross-over among the half-cells [22-24].

During operation of the RFB the flow-through electrodes mainly deliver the electrochemically active surface area to ensure unhindered electrolyte flow and the procedure of the expiring redox reactions. Porous carbon electrodes consisting of carbon fibers, felts or nanotubes meet these requirements. Graphitic bipolar plates ensure the electrical contact to the porous carbon electrodes. The bipolar plates are electrically contacted via two metal current collectors. Both half-cells are isolated from each other using insulating spacers. Mechanically robust end plates mounted at the front sides guarantee the structural stability of the VRFB. Flow fields attached to the electrolyte inlet as well as outlet improve the electrolyte distribution in the porous carbon electrodes [21]. The electrolyte solution present at the RFB anode is called anolyte, while the designation catholyte corresponds to the cathodic electrolyte [22-25]. In accordance with convention the battery's electrode on which the oxidation takes place during the discharging process is defined as the anode.

Both redox flow battery and electrolyte tanks are interconnected via tubings equipped with pumps. In case of electricity demand, the electrolyte is circulated separately through the half-cells of the RFB energy converter by pumping to transform the electrolyte's chemically stored energy into electric energy [22-23]. The electric energy is supplied by redox reactions due to the electrochemical potential difference between the electrochemical active species of the two half-cells [21,26]. Therefore, redox flow batteries show similarities to the general set-up of polymer electrolyte membrane fuel cells (PEMFC) and are treated as attractive devices for stationary electrical energy storage (EES) of renewable energies [21,27-29].

While the PEMFC is only utilized for the generation of electrical energy from chemical energy, it requires an additional electrolyzer for the reversed reaction. Contrarily, resulting from the reversible redox reactions taking place in the rechargeable RFB, it is able to work as both energy supply and EES or electrolyzing unit respectively [22-24,28,30]. Referring to the reversible RFB redox reactions also encountered in solid-state batteries, redox flow batteries are also described as regenerative/rechargeable fuel cells [22, 24,31]. The general structure and working principle of a redox flow battery is shown in Fig. 4.

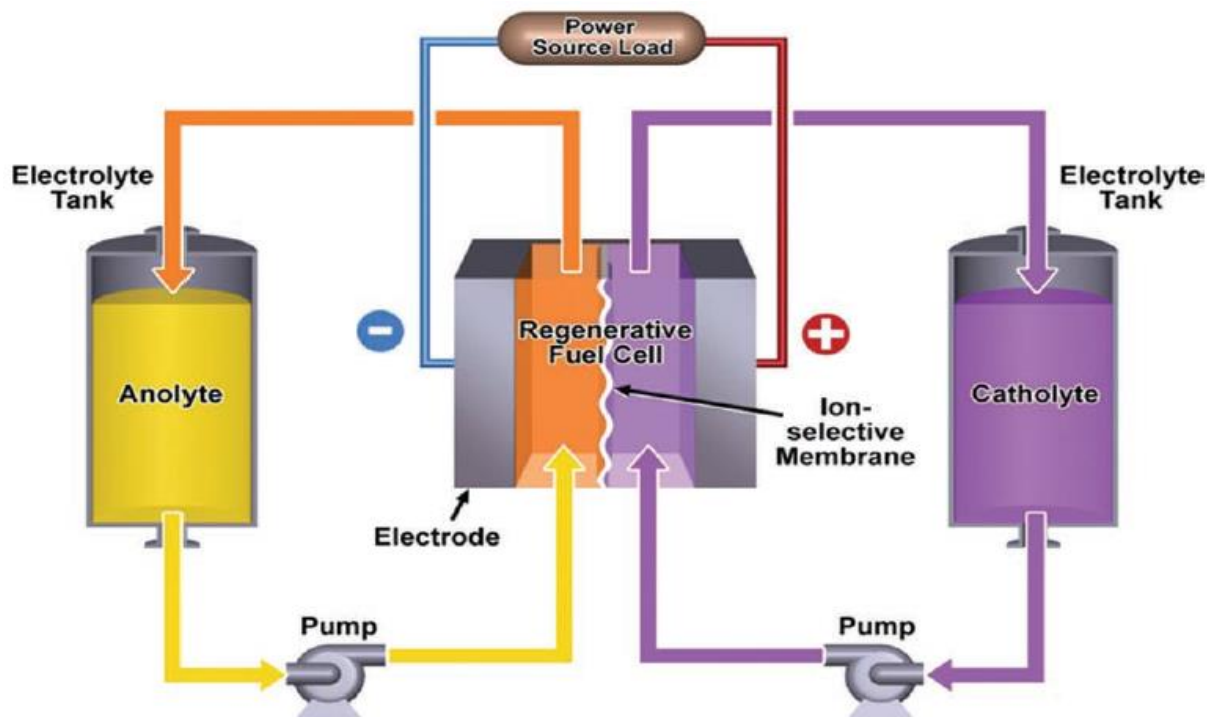


Fig. 4. General structure and working principle of a redox flow battery [22].

Due to the modular design of the RFB, its capacity can be adjusted independently from the RFB's power output [22-25,31]. Thus, the electrolyte volume and the corresponding concentration of the electrochemical active species are directly proportional to the RFB's capacity. The power of the RFB increases with the graphite felt's active surface area and the number of installed RFB single cells, thus its stack size [22,24]. Accordingly, commercial RFB systems can be individually tailored considering the customer's requirements. A simple cell- and stack-architecture facilitates scale-ups to large RFB plants as well as small power supplies for private users [22,24]. Thus, redox flow batteries are dealt as both electrical energy storage solutions directly connected to the electricity grid and insular EES applications. Generally, RFBs exhibit short response times to meet the rapidly changing electricity demand. Elaborate installations for temperature control can be diminished, because of the continuous removal of heat from the RFB stacks by the electrolyte [22,25-26].

Various RFB redox chemistries have been investigated in the last decades. Among the first modern systems is the iron-chromium redox flow battery developed by the National Aeronautics and Space Administration (NASA) in the 1970 [32]. Other inorganic systems combined with protic electrolytes were studied like the zinc/bromine flow battery [33], the all-vanadium redox flow battery [34] and the all-lead redox flow battery [35], for instance. The all-chromium RFB utilizes chromium complexes with ethylenediaminetetraacetic acid (EDTA) for energy storage [36]. Dipolar aprotic electrolytes were also examined like the vanadium(III)-acetylacetonate system. Due to the absence of water higher open-circuit voltages (OCV) are achieved [37]. Another possibility is the application of organic substances e.g. redox active polymers [38]. Furthermore, the usage of highly concentrated ionic liquids together with water is a novel promising method to increase the cell voltage and energy density of the RFB [39].

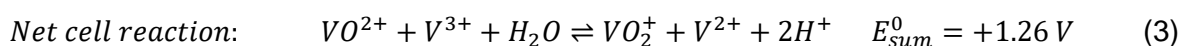
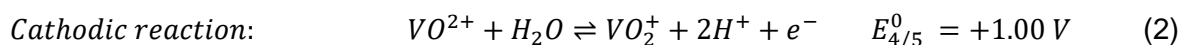
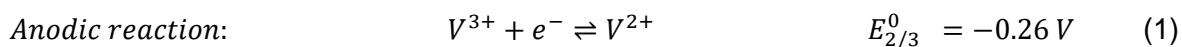
## 2.2 The all-vanadium redox flow battery

### 2.2.1 Operating principle

Until now, all-vanadium redox flow batteries (VRFB) belong to the most investigated RFB systems. At the beginning of the research activities, electrochemical measurements were conducted on vanadium ions in solution by means of mercury and platinum electrode materials [40-42]. Further examination within the NASA redox flow battery project was first excluded due to the reactivity of the platinum electrodes with the vanadium electrolyte. Additionally, slow kinetics of the positive half-cell reactions at the applied carbon felt electrodes as well as irreversibility for the negative half-cell reactions combined with elevated costs made further studies unattractive [43].

In 1986 Skyllas-Kazacos et al. proved the applicability of the differently oxidized and acid soluble vanadium ion species [44]. Sum et al. demonstrated the dependence of redox reaction rate and reversibility on the electrode preconditioning. A key element is the oxidation state of the carbon atoms on the electrode surface, which is defining the irreversibility and the reversibility, respectively [45-47]. A crucial benefit of the all-vanadium redox flow battery is the application of the identical element in both half-cells. This minimizes the loss of energy and capacity triggered by cross-contamination due to undesirable electrolyte components [24]. Additional RFB chemistries with redox couples incorporating at least three oxidation states are only described for chromium, uranium, neptunium and lead [21].

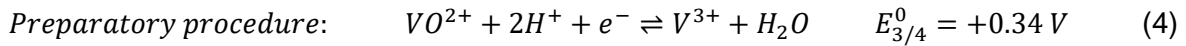
Generally, the VRFBs electrolytes consist of 1.5-2.0 mol L<sup>-1</sup> vanadium ions dissolved in 2.0 mol L<sup>-1</sup> sulfuric acid. The resulting energy density reaches a theoretical maximum at 38 Wh L<sup>-1</sup> [21]. Therefore, an application of the VRFB in fields with high demands on space requirement and weight are excluded, e.g. a direct integration in electric cars [31]. Favored scopes for the VRFB are for example stationary energy storages to store fluctuating renewable energy and reduce the load of the electricity grid [23,48]. The conversions from chemical to electrical energy and vice versa are achieved by alterations of the vanadium ions valance state. The redox reactions taking place in operation of the VRFB are specified in the following.



During charging, the reduction of trivalent V<sup>3+</sup> to bivalent V<sup>2+</sup> takes place in the negative half-cell. Simultaneously, in the positive half-cell the oxidation of the tetravalent vanadium in form of the VO<sup>2+</sup>-species to the pentavalent vanadium ion incorporated in the VO<sub>2</sub><sup>+</sup> species is observed. Additionally, two protons are formed in the positive half-cell during charging. One of them is transferred through the ion-selective membrane from the positive to the negative half-cell of the VRFB for charge balancing.

Commonly before operation begins, both the anodic and the cathodic half-cell of the VRFB are equipped with electrolyte of the same composition. It consists of a 50:50 mixture of  $V^{3+}$  cations and the  $V^{4+}$  species  $VO^{2+}$ . Prior to the actual operation of the VRFB during the preparatory procedure, the  $VO^{2+}$  content of the anolyte is entirely reduced to  $V^{3+}$ . Simultaneously, the  $V^{3+}$  share of the catholyte is completely oxidized to  $VO^{2+}$  (see Eq. 4). With this measure the preferential operational mode of the VRFB is reached.

The favored electrolyte composition is located within the potential range of  $V^{2+}$  to  $V^{3+}$  for the anolyte and  $V^{4+}$  to  $V^{5+}$  for the catholyte (see Eq. 1-3). It is featured by a low potential drop and efficient VRFB operation. Contrarily, the direct operation without the preparatory procedure for the electrolytes leads to considerable higher potential drops and therefore significant losses in the battery's efficiency. After completion of this preparatory procedure the VRFB electrolyte is ready for the actual charging/discharging process as described before by means of Eq. 1-3.



In presence of standard conditions (total vanadium ion concentration =  $1 \text{ mol L}^{-1}$  at  $T = 298.15 \text{ K}$  and  $p = 1013 \text{ hPa}$ ) the difference between the positive and the negative half-cell potential of the VRFB single cell is located at  $E_{sum}^0 = 1.26 \text{ V}$  (see Eq. 3) [26].  $E_{sum}^0$  is representatively utilized for the VRFB single cell open circuit voltage (OCV) at standard conditions.

Due to the absence of standard conditions during ordinary VRFB operating mode (increased total vanadium ion concentration, deviations in temperature and pressure), the  $E_{sum}^0 / \text{OCV}$  value lies at approximately  $1.4 \text{ V}$  at a state-of-charge (SOC) of  $0.5$  [26]. A schematic set-up of an all-vanadium redox flow battery is depicted in Fig. 5. The redox active vanadium species and their associated redox reactions are assigned to the appropriate half-cell for the discharge reaction.

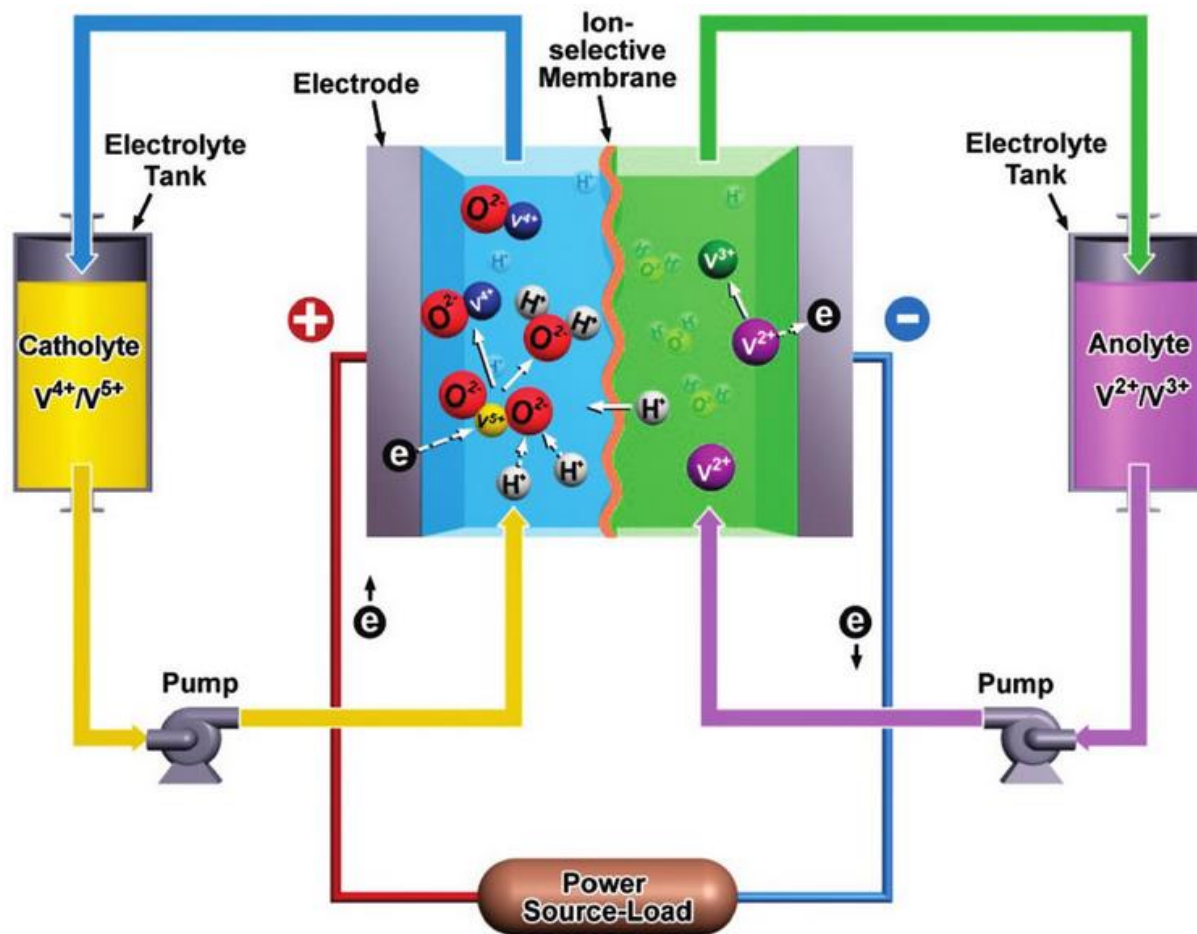


Fig. 5. Schematical set-up of an all-vanadium redox flow battery with expiring redox reactions for the discharging process [24].

### 2.2.2 Electrode material

Central characteristics aimed for VRFB electrodes are high electrochemical and mechanical stability, fast reaction kinetics for the vanadium redox couples combined with low electrical resistance at favorable prices [21]. Due to the aqueous electrolyte's acidic and corrosive properties, graphite- or carbon- based materials are usually applied. Their advantages are chemical inertness and a pronounced overvoltage relating to oxygen or hydrogen formation. Disadvantageous are the relatively high electrical resistivity and the low mechanical stability [49].

Graphite- or carbon- based electrodes with high surface areas made of porous or felt structures are commonly used in the VRFB to provide the necessary electrochemically active surface area for the redox reactions. These electrode materials often show insufficient electrochemical activity and kinetic reversibility with respect to the vanadium redox reactions [22]. Mostly, their activity is further increased by additional chemical, electrochemical or thermal treatment [50-53]. Additionally, doping with e.g. nitrogen as electrochemical active site and the deposition of nanomaterials for enlargement of the catalytic active surface have been investigated [54-59].

Thermal preconditioning is often dealt as the easiest and most effective procedure for activity improvement of VRFB electrodes [22]. The surface hydrophilicity and the amount of electrochemically active sites on the electrode surface are enhanced [49-60]. As suggested in literature, the increased introduction of functional groups, like hydroxyl functionalities (C-O-H) or ketones (C=O) on the electrode surface is the basis for this rising amount of electrochemically active sites [22]. These C-O functionalities are supposed to operate as catalysts for the redox reactions of the vanadium species by Sun et al. [51]. Due to the formation of covalent bonds between the C-O functionalities on the electrode surface and the vanadium ions (C-O-V) crucial reaction parts like oxygen or electron transfer are promoted. This corresponds to the reduction of the activation overpotential of the vanadium redox processes [51,52].

In the case of chemical pretreatment with concentrated sulfuric acid modifications similar to the thermal preconditioning of the electrodes were achieved, e.g. increased hydrophilicity and electrochemically active area. Contrarily, surface functionalization is not limited to hydroxyl or ketone functions and is also exhibiting carboxyl groups (C-OOH) [52]. Combined approaches utilizing chemical and thermal preconditioning as well as electrochemical treatment led to an increased amount of electrochemically active C-OOH sites on the electrode surface [61-63].

### 2.2.3 Bipolar plate material

Bipolar plates are used in the VRFB for different reasons. Generally, the bipolar plates stabilize the flexible electrode materials and function as conductive connection between the latter and the current collectors [24]. In the case of VRFB stacks, they separate negative and positive half-cell electrolytes. Depending on the VRFB structure, bipolar plates are additionally utilized to navigate the electrolyte flow through the VRFB cell. In this case, they are equipped with flow channels [24]. Necessary properties are their high electrical conductivity in combination with structural and mechanical stability. Bipolar plates should also exhibit chemical inertness concerning the acidic and corrosive environmental conditions of the vanadium electrolyte [24]. Therefore, only a limited amount of electrode materials is regarded as suitable for the application in all-vanadium redox flow battery systems.

Among these, material formulations consisting of graphite or carbon combined with polymers are widely utilized, e.g. polymer-impregnated graphite plates, polymer-impregnated flexible graphite and carbon-polymer composites [64-67]. The graphite or carbon content of the bipolar plate ensures its electrical conductivity. Its polymer content inhibits the desorption of vanadium ions of the electrolyte out of the VRFB cell due to electromigration [21]. VRFB polymer-impregnated graphite plates exhibit good conductivity and fabricability. Drawbacks like elevated costs and brittleness restrict the widespread use. Contrarily, the lightweight carbon-polymer composites overcome the problems of polymer-impregnated graphite plates concerning cost and flexibility and are therefore often favored [64,65,68-71].

### 2.2.4 Ion-selective membranes

The positive and the negative half-cell of the VRFB are separated by a membrane to prevent mixture of the electrolytes. Simultaneously, charge balancing is permitted by diffusion of charged ions, e.g.  $H^+$ ,  $SO_4^{2-}$  through this diaphragm [22]. Further crucial requirements besides low cost are the chemical and mechanical stabilities of the membrane corresponding to the VRFB operating conditions in the applied SOC range [22]. To achieve a low resistivity, the ion-selective membranes exhibit high hydrophilicity at the liquid-solid interface between the membrane surface and the vanadium electrolyte [22]. Undesired effects are the diffusion of the active vanadium species or water through the membrane. By withholding the vanadium ions from crossing the membrane capacity losses are minimized. As a result ions are conducted well and selectively [22]. Thus, the transport of the active species and water is limited and the resulting energy losses are reduced.

Generally, ion exchange membranes consist of a polymeric basis structure, commonly referred to as polymer backbone and side chains with diverse acid or basic functional groups [21]. These polar acidic or basic functionalities attract water or dipolar solvents and cause a polymer swelling. When the swelling procedure is finished, a three dimensional network consisting of solvent molecules is obtained [21]. Through the water channels of this network transport of mobile ions, particularly small particles like protons can proceed [72]. Ionic functional groups on the polymer surface establish a charged stationary phase, which is generating an electrostatic shield. Consequently, a highly selective exchange and retention of anionic and cationic electrolyte components is ensured by the membrane's electrostatic selection mechanism [21].

Concerning the charge state of the stationary polymer phase ionic exchange membranes can be manufactured as cationic or anionic ion-exchange membranes. Due to the harsh chemical conditions of the vanadium electrolyte perfluorinated cationic polymer membranes are usually preferred for the VRFB cells [73]. In this case, perfluorosulfonic acids (PFSA) are utilized as standard polymer basic building blocks. In these polymers the sulfonic acid groups are connected to the polymer backbone via fluorinated spacers. The amount of the fluorinated spacers in the membrane determines its chemical resistance and its extent of swelling [21].

Higher selectivity relating to species permeation, also described as permselectivity, is achieved with anionic exchange membranes. Then, commonly trimethylamine groups are introduced in a polymer backbone like poly(fluorenyl ether) [74]. To further improve the membrane's permselectivity the pristine membrane is modified by insertion of inorganic substances into the polymer matrix. The underlying concept of the resulting composite membranes is the decrease of its pore size. In this context inorganic materials like silicates, zirconium phosphate or titanium dioxide were added to different polymers during manufacturing [75-80]. Additionally, membranes treated with polyaniline and polypyrrole respectively were investigated to reduce the transfer of vanadium active species [81-82].

## 2.3 VRFB-Electrolyte

The vanadium electrolyte is the liquid energy carrier of the VRFB, in which the electrical energy is chemically buffered by means of vanadium compounds. Due to the full reversibility of the energy storage process the VRFB provides a promising cycle stability perspective. Concerning this feature the electrolyte tolerates a nearly unlimited number of energy conversions from chemical into electrical energy and vice versa. Commonly, it consists of vanadium ions dissolved in concentrated sulfuric acid. Due to its rather low energy density triggered by the limited solubility of vanadium in sulfuric acid, large quantities of electrolyte volumina are employed [21]. Thus, the vanadium electrolyte is contributing a considerable share to the cost of the entire VRFB system [60,83].

### 2.3.1 Vanadium chemistry in aqueous solution

In the electronical ground state elementary vanadium exhibits the electron configuration [Ar]  $3d^3 4s^2$ . Regarding the vanadium chemistry in aqueous solution, four different oxidation states of vanadium central ions (2+, 3+, 4+, 5+) are accessible. Generally, the presence, structure and total charge of the vanadium compounds in solution are depending on the actual pH value in solution [26]. As solvents, mainly acidic solutions ( $\text{pH} < 1$ ) like concentrated  $\text{H}_2\text{SO}_4$  are utilized. Because of the acidic conditions cationic vanadium compounds are formed. In this environment, vanadium offers a versatile aqueous chemistry with aqua ions of the four oxidation states 2+ to 5+. The vanadium cation  $\text{V}^+$  is not generated due to instability under these circumstances [26].

For the oxidation states 2+ to 4+ the corresponding hexa-aqua respectively penta-aqua mononuclear complexes are formed. In case of  $\text{V}^{5+}$  a more complex aqueous chemistry is obtained. Depending on the solution's pH value, the vanadium concentration and the presence or absence of vanadium species of differing oxidation state, binuclear or possibly polynuclear complexes are found [84]. Thus, a broad range from sparsely oxidized  $\text{V}^{2+}$  aqua complexes to highly oxidized  $\text{V}^{5+}$  species can be obtained [26].

While  $\text{V}^{2+}$  is continuously oxidized to  $\text{V}^{5+}$  characteristic color changes of the aqua ions are observed. At the beginning of the oxidation the violet  $\text{V}^{2+}$  aqua ion reacts to green  $\text{V}^{3+}$ . The green  $\text{V}^{3+}$  is oxidized to the blue  $\text{V}^{4+}$  ion and finally yellow  $\text{V}^{5+}$  is yielded at the end of the oxidation. Due to these specific color changes, the oxidation state of aqueous vanadium samples is optically definable. As a result, SOC and quantitative determinations based on the optical information are enabled [26].

### Vanadium (II+)

The  $V^{2+}$  ion appears in aqueous solutions as the corresponding violet hexa-aqua complex  $[V(H_2O)_6]^{2+}$  with octahedral structure (see Fig. 6). Owing to the negative standard reduction potential of the  $V^{2+/3+}$  redox couple  $E_{2/3}^0 = -0.26 V$ ,  $V^{2+}$  is a strong reducing agent. It is easily oxidizable when getting in contact with oxygen and requires handling under inert gas atmosphere [85]. In combination with water  $V^{2+}$  is oxidized and simultaneously hydrogen gas is formed. Contrarily, in aqueous acidic solutions of sulfuric acid  $V^{2+}$  is stabilized by the existing sulfate anions [86]. After degassing of the acidic  $V^{2+}$  solutions to remove the remaining oxygen the  $V^{2+}$  dissolved in sulfuric acid exhibits long-term stability. Apart from the exhaustive electrolytic reduction of higher oxidized vanadium ions in acidic environment, the complete reduction by means of amalgamated zinc is feasible [84].

### Vanadium (III+)

Normally,  $V^{3+}$  compounds like  $V_2O_3$  or  $V_2(SO_4)_3$  are used for the solution preparation of the latter. In aqueous, acidic solution  $V^{3+}$  occurs in form of its green, octahedrally structured hexa-aqua complex  $[V(H_2O)_6]^{3+}$  [26]. Hence, the  $V^{2+}$  complex as well as the  $V^{3+}$  complex are coordinated by six water molecules. Compared to the divalent  $V^{2+}$  aqua complex, the trivalent  $V^{3+}$  complex vanadium-ligand bond lengths are shorter and the octahedral hydration structure is distorted (see Fig. 6). The underlying cause is the increased charge density of the  $V^{3+}$  aqua complex in contrast to the  $V^{2+}$  analog [87,88].

### Vanadium (IV+)

The  $V^{4+}$  ion is covalently bonded to one additional oxygen atom in case of acidic conditions. Thus, in aqueous solution this  $VO^{2+}$  central ion also referred to as vanadyl ion or oxovanadium(IV) cation is present as the corresponding sky-blue penta-aqua complex  $[VO(H_2O)_5]^{2+}$ . Compared to the divalent and the trivalent vanadium aqua complexes, the  $VO^{2+}$  cation is complexed by five water molecules. These five water molecules combined with the vanadyl oxygen lead to an octahedral geometry of the mononuclear  $VO^{2+}$  aqua complex [88-91]. This octahedral structure of the complex shows a geometrical distortion due to the oxy-oxygen repulsion (see Fig. 6). As a result, the average length of the equatorial V-O bonds is shorter compared to the average axial V-O bond length [88,90].

By means of relatively strong acids dissolved vanadyl compounds can be protected against atmospheric oxidation [86]. In case of chemical treatment the vanadyl's covalent V-O bond is very stable and is preserved. Together with ligands incorporating distinctively electronegative donor atoms like F, Cl, O and N, the vanadyl central ions form strong bonds [92]. Usually, blue  $VOSO_4 \times 5 H_2O$  is used as starting chemical to produce aqueous  $VO^{2+}$  solutions. Beside the existence of  $VO^{2+}$  aqua complexes, vanadyl sulfate complexes are also assumed by Ivakin and Voronova [93]. However, only limited intermolecular electrostatic interactions are obtained for the complexation of the vanadyl aqua ion with the sulfate ions [89].

Additionally, Vijayakumar et al. investigated the shape and composition of the vanadyl ions in sulfuric acid by means of  $^1\text{H}$  and  $^{17}\text{O}$  NMR spectroscopy. Based on their results, it was concluded that the vanadyl central ion is present as the corresponding aqua complex  $[\text{VO}(\text{H}_2\text{O})_5]^{2+}$  up to a concentration maximum of  $3 \text{ mol L}^{-1}$  and within a temperature range of  $-33 \text{ }^\circ\text{C}$  to  $67 \text{ }^\circ\text{C}$  [89].

### Vanadium (V+)

Commonly, for the preparation of  $\text{V}^{5+}$  solutions vanadium pentoxide is applied.  $\text{V}_2\text{O}_5$  is orange and exhibits a poor solubility in  $\text{H}_2\text{O}$ . An increased solubility of  $\text{V}_2\text{O}_5$  is obtained by means of strongly acidic solvents. In this case yellow-green  $\text{V}^{5+}$  solutions are produced. Regarding the pH range between  $-0.5$  and  $1.3$ , the dominant  $\text{V}^{5+}$  species is the pervanadyl or cis-dioxovanadium(V) cation  $\text{VO}_2^+$  [26]. The cis-dioxo configuration is probably formed to optimize  $d_{\pi}\text{-}p_{\pi}$  bonding. Corresponding O-V-O angles are in the range of  $104^\circ\text{-}107^\circ$  [84].

Due to the pronounced positive standard reduction potential of the  $\text{V}^{4+/5+}$  redox couple  $E_{4/5}^0 = +1.00 \text{ V}$ , the  $\text{V}^{5+}$  compounds are rather strong oxidizing agents. For example in presence of hydrochloric acid HCl, vanadium pentoxide is reduced to  $\text{VO}^{2+}$  and elementary chlorine gas is formed [94].

In aqueous solution two possible structures of the mononuclear  $\text{VO}_2^+$  aqua complex are distinguished. The octahedral  $\text{VO}_2^+$  aqua complex  $[\text{VO}_2(\text{H}_2\text{O})_4]^+$  incorporating four water molecules and the corresponding bipyramidal  $\text{VO}_2^+$  complex  $[\text{VO}_2(\text{H}_2\text{O})_3]^+$  with one water ligand less than the octahedral complex are proposed [88,95-97] (see Fig. 6). According to the conclusions of the thermodynamic calculations and the geometrical optimizations published in literature, the bipyramidal complex structure is preferred over the octahedral complex geometry [88,95,97]. Consequently, the bipyramidal  $\text{VO}_2^+$  aqua complex is the most frequent  $\text{VO}_2^+$  aqua complex due to its superior stability.

Besides, Ivakin and Voronova investigated the  $\text{V}^{5+}$  complex formation concerning acidic solutions, which contain sulfate anions. Therein, an equilibrium between the  $\text{VO}_2^+$  aqua complexes and the corresponding sulfate complexes is expected [93].

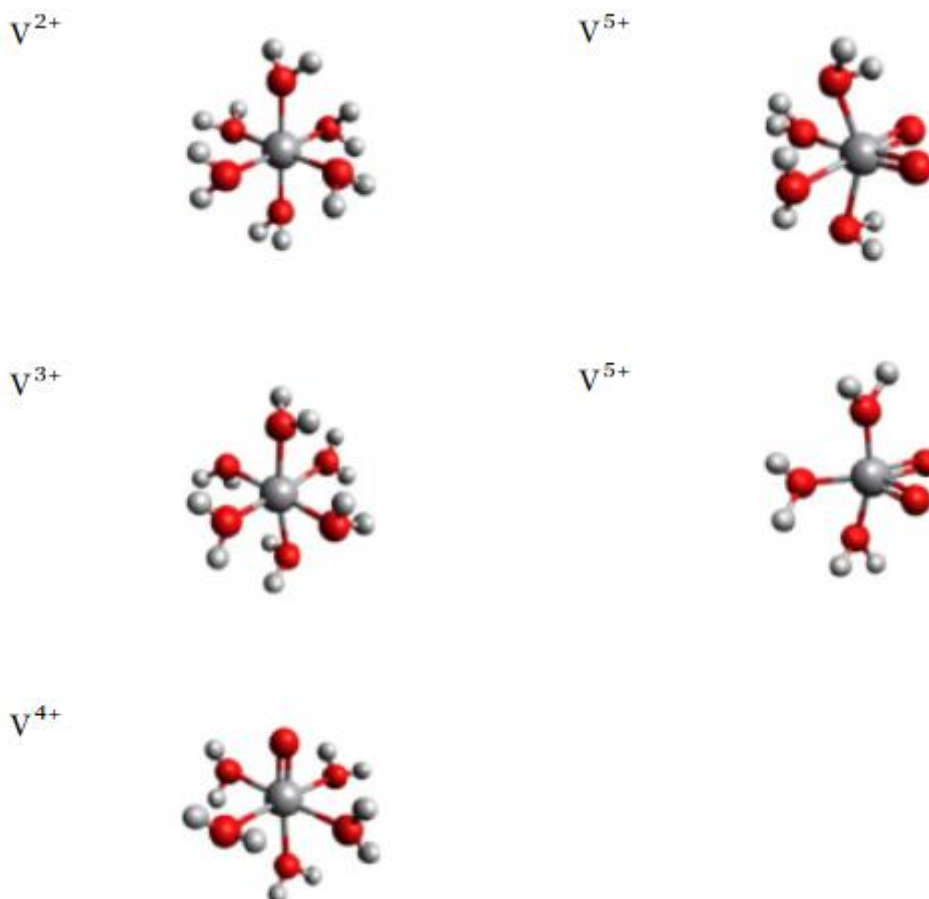


*Fig. 6. Geometrical structures of the vanadium aqua complexes from  $V^{2+}$  to  $V^{5+}$ . For  $V^{2+}$  to  $V^{4+}$  octahedrally shaped complexes are obtained. In case of  $V^{5+}$  the bipyramidal structure is preferred over the octahedral complex geometry (see second row). The complex structures of  $V^{3+}$  to  $V^{5+}$  exhibit geometrical distortions from the ideal octahedron of the  $V^{2+}$  complex [87-91,95-100].*

### 2.3.2 Common vanadium sources

The final vanadium electrolyte price mostly depends on the charges for the vanadium raw material. Normally, high-purity vanadium pentoxide ( $V_2O_5$ ) is applied as vanadium source for the electrolyte production. The vanadium pentoxide prices are subject to certain variability. A limited supply in combination with a rising demand for vanadium used as alloying metal for high-tensile steel e. g. by the rapidly growing Chinese economy are observed [26]. These events are causal for the instability of the high-purity vanadium costs. To counteract this uncertainty on the vanadium market, a significant increase of the vanadium production capacity is striven. Thus, the supply restrictions and excessive price increases for the vanadium raw material should be avoidable [26].

Vanadium is the 20<sup>th</sup> most abundant element on the globe and constitutes a share of around 0.0015 % of the earth crust [26]. Currently, the majority of the vanadium chemicals are produced by means of the byproducts from fossil fuels and mineral ore processing.

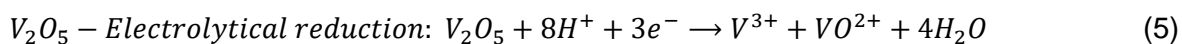
Usually, the used vanadium sources comprise deposits like iron-titanomagnetite, mining slag, oil sludge, fly ash or spent catalysts [101,102]. For the application in the VRFB vanadium electrolyte only high-purity vanadium compounds are chosen. Thus, adverse effects on the VRFB performance owing to impurities in the electrolyte can be excluded. A central drawback of this approach is the elevated price of the vanadium pentoxide due to the more intense purification procedure. Therefore, in order to enhance the attractiveness of the VRFB a more price-competitive technology is aimed at. After analysis of potential impurity effects on the battery performance, the use of cheaper low-grade vanadium also originating from recycling of industrial byproducts is intended [102,103].

### 2.3.3 Vanadium electrolyte production

After the establishment of the VRFB technology the vanadium electrolyte was initially prepared via dissolution of vanadyl sulfate ( $VOSO_4$ ) in sulfuric acid [104,105]. Due to the elevated price of the vanadyl sulfate it was replaced by the cheaper vanadium pentoxide. Compared to  $VOSO_4$ ,  $V_2O_5$  exhibits an approx. ten times lower solubility in aqueous  $H_2SO_4$  [34,106]. The noticeably decreased solubility of vanadium pentoxide resulted in the necessity to evolve suitable chemical or electrolytic dissolution approaches. With the introduction of primarily two methods VRFB electrolytes of the desired vanadium concentration are accessible with use of vanadium pentoxide powder [107-112].

In one attempt the vanadium pentoxide and sulfur dioxide form vanadyl sulfate in a redox reaction. This reaction is also indicated as chemical dissolution. A general drawback is the toxicity of the sulfur dioxide. In case of the utilization of other chemical reductants not required byproducts or intermediates can potentially stay in the finished electrolyte product [26].

Therefore, the second strategy in form of the suspended powder electrolysis was developed to overcome these disadvantages. On the basis of this technique the vanadium pentoxide powder dissolved in  $H_2SO_4$  is reduced to a 50:50 molar mixture of  $V^{3+}$  and  $V^{4+}$  (also designated as  $V^{3.5+}$ ) in the negative half-cell of an electrolysis apparatus (see Eq. 5). In the positive half-cell an equally concentrated aqueous  $H_2SO_4$  solution is applied, where  $H_2O$  is oxidized to gaseous oxygen [112].



A central challenge of this electrolytical approach is the maintenance of the vanadium pentoxide powder suspension during the production scale up [26]. Besides, the application of filters to inhibit the clogging of the continuously operated set-up by the vanadium pentoxide powder increases the complexity of the apparatus. Because of the slow kinetics of the reduction process only low current densities and consequently a limited reduction rate per cathode area are obtained [26]. Due to these imperfections further efforts were conducted leading to several improved preparation methods stated in the following.

### The vanadium pentoxide/vanadium trioxide reactive dissolution approach

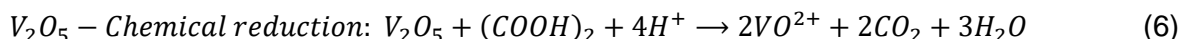
In the first step vanadium trioxide ( $V_2O_3$ ) is dissolved in sulfuric acid to obtain  $V^{3+}$  cations. In the next step a predefined amount of vanadium pentoxide is added to the solution to react with the present  $V^{3+}$  cations to a  $V^{3.5+}$  composition. This  $V^{3.5+}$  electrolyte is applied in both VRFB half-cells. After the adjustment of 0 % SOC by means of the preparatory procedure discussed in chapter 2.2.1 the VRFB electrolyte is ready for the actual energy storage purposes. A positive side effect is the exothermic redox reaction of the differently oxidized vanadium oxides which evokes a temperature increase in the solution. Consequently, an accelerated dissolution of the freshly added vanadium oxide powders is induced [113,114].

### The reaction of $V^{4+}$ and $V^{5+}$ with elementary sulfur

This technique applies tetra- or pentavalent vanadium sources like vanadyl sulfate, vanadium dioxide  $VO_2$  or vanadium pentoxide, sulfuric acid and elementary sulfur as basic chemicals. First of all, the predetermined quantities of vanadium powder, concentrated sulfuric acid and the reductant sulfur are mixed to generate the vanadium species of a particular oxidation state e. g.  $V^{3.5+}$ . A mechanical blender is used to produce a homogeneous paste of the chemicals to ensure a consistent reaction process in the subsequent steps. Accordingly, the paste is calcined in the temperature range of 150 °C to 440 °C to obtain the mixed valence vanadium composition, which is dissolved in sulfuric acid to form the final VRFB electrolyte [115].

### The chemical reduction of $V^{5+}$ suspensions and solutions respectively

At the beginning, a  $V^{5+}$  source like vanadium pentoxide is dissolved in sulfuric acid. Then, a reducing agent e.g. oxalic acid, oxalates, hydrogen, alkyl alcohols or sulfur dioxide is added to the solution [107]. Accordingly, a positive side effect is that the solution stays free of contamination related to the reducing agents [116]. Thus, if sulfuric acid is formed during the redox reaction it is not removed as an integral content of the electrolyte. If the reaction product is gaseous, a removal from the electrolyte without remaining contamination is simple. In Eq. 6 the chemical reduction of  $V_2O_5$  with oxalic acid is stated [109].



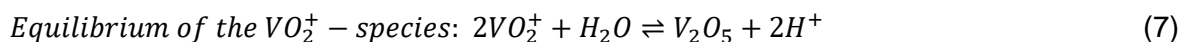
In principle other reductants containing nitrogen, phosphorous, sulfur or metal based reducing agents are theoretically applicable [107,116]. But these reactants are generally regarded as critical due to their impurification of the electrolyte. For example, certain metals like Cu, Ni or Sn enhance the hydrogen evolution after their deposition on the negative electrode during the VRFB charging operation.

In the case of these three metals, their depositions are already expiring during the charging process, due to the less negative standard reduction potential compared to the  $V^{2+}/V^{3+}$  redox pair [26]. Besides, deposits of ammonium or silicon dioxide further the clogging of the graphite felt electrode and lead to a substantial decrease of the flow rate [103]. Thus, the overall battery efficiency is lowered. Concerning these significant drawbacks, the application of impurity causing reactants is commonly avoided [26,116].

### 2.3.4 Vanadium species solubilities and their impact on electrolyte composition

Regarding the evolution of the vanadium species solubility in the case of alterations in temperature and sulfuric acid concentration, the behavior of  $V^{2+}$ ,  $V^{3+}$  and  $V^{4+}$  differs from the  $V^{5+}$  behavior. Concerning the solubility of the  $V^{2+}$  to  $V^{4+}$  compounds, an increase of the same is observed with increasing temperature and decreasing sulfuric acid concentration. The reduction of solubility with rising acid concentration is due to the common ion effect [117,118]. Considering  $V^{2+}$  to  $V^{4+}$ , the precipitation of these species occurs in form of the corresponding vanadium sulfate salts. With the higher  $H_2SO_4$  concentration an increased total sulfate concentration is accompanied. Thus, the solubility equilibrium of the related vanadium sulfate is shifted towards a solubility decrease of the latter [26].

Contrarily, the  $V^{5+}$  species precipitate as the corresponding  $V_2O_5$  in the presence of thermal energy impact [26]. Compared to the  $V^{2+}$  to  $V^{4+}$  compounds, the oxygen is participating in the precipitation instead of the sulfate anions. Thus, the sulfate anions do not have any effect on the  $V^{5+}$  solubility. Additionally, the expose of heat is a central requirement for the energy-consuming generation of  $V_2O_5$ . The endothermic redox reaction is stated below.



According to Eq. 7, if a formation of additional protons takes place, the backward reaction will be preferred [108]. This triggers an elevated solubility of the  $V^{5+}$  species. To summarize, the solubility trend of  $V^{5+}$  is inverted compared to the already discussed trend for  $V^{2+}$  to  $V^{4+}$ . The  $V^{5+}$  solubility increases with decreasing temperature and increasing  $H_2SO_4$  concentration [108,119]. As a result, the maximally applicable total vanadium concentration depends on the intended VRFB operating temperature regime. Their dependency is reciprocally proportional. If the used temperature range is enlarged, the total vanadium concentration and consequently the VRFB energy density are reduced.

A workable approach to maximize the battery's energy capacity as well as the operating temperature regime is proposed in literature [26]. Therein, the VRFB's SOC range is adapted in the presence of extreme climatic conditions to inhibit vanadium compound precipitation. These measures prevent VRFB stack channel clogging and the electrolyte flow reduction.

Considering the solubility trends for all vanadium oxidation states in sulfuric acid and a desired temperature interval from 10 °C to 40 °C, the favored total vanadium concentration is situated in the range of 1.6-2.0 mol L<sup>-1</sup> accompanied with a total sulfate concentration of 4-5 mol L<sup>-1</sup> [26]. Here, the sulfate is the sum of all sulfate and bisulfate anions in the electrolyte.

In case of cold climates, a total sulfate concentration of roughly 4 mol L<sup>-1</sup> is adjusted to prevent vanadium sulfate precipitation of V<sup>2+</sup> to V<sup>4+</sup>. For warmer climates, the sulfuric acid concentration is increased until a total sulfate concentration of approximately 5 mol L<sup>-1</sup> is reached to suppress the thermal precipitation of V<sup>5+</sup> to V<sub>2</sub>O<sub>5</sub> [26].

However, if the precipitation as vanadium salts has already been occurred, the salts of V<sup>2+</sup> to V<sup>4+</sup> are dissolved again by means of thermal treatment. In case of formed V<sub>2</sub>O<sub>5</sub> precipitates the dissolution can be electrochemically performed [26]. One possibility is to invert the electrolysis cell's polarity to reduce V<sup>5+</sup> to V<sup>3+</sup> or V<sup>4+</sup> species with better solubility characteristics. Another option is to solubilize the V<sub>2</sub>O<sub>5</sub> deposit via chemical reduction by addition of a certain amount of negative electrolyte [26].

Additionally, the application of phosphate improves the stability of the VO<sub>2</sub><sup>+</sup> cation at elevated temperatures. The stability enhancement can possibly proceed by complexation or ion-pairing of phosphate with the VO<sub>2</sub><sup>+</sup> cations. Another suggestion is the phosphate adsorption on the V<sub>2</sub>O<sub>5</sub> nucleation sites. Hence, further precipitation of V<sub>2</sub>O<sub>5</sub> will be prevented due to the blocked nucleation sites and the related stop of crystal growth [98].

## 2.4 Definition of the State-of-Charge

For the efficient operation of a battery the knowledge of its energy level is mandatory. Therefore, a measure for the battery's energy level is required. In case of the all-vanadium redox flow battery, the chemical composition of the vanadium electrolyte is altered noticeably during operation.

Considering the VRFB charging process in the positive half-cell,  $V^{5+}$  species are formed via oxidation of  $V^{4+}$  ions. Similarly in the negative half-cell, the  $V^{2+}$  concentration is increased and simultaneously  $V^{3+}$  is reduced. Thus, when electric energy is stored in the VRFB electrolyte the average oxidation state and subsequently the potential of the negative half-cell is decreased while the positive half-cell potential and its average oxidation state are increased.

Consequently, the difference of the two half-cell potentials is also increased. This potential difference is commonly referred to as the open circuit voltage (OCV), if its measurement is proceeded current-less. As a result, the higher the actual VRFB's OCV rises, the more electrical energy is accumulated in the battery in the form of chemically stored energy.

A popular and probably more familiar indication of the battery's energy level is given by the state-of-charge (SOC). To obtain the SOC, the knowledge of the differently oxidized vanadium species concentrations in the electrolyte is required. Derived from these concentrations the SOC can be determined, which specifies the battery's remaining capacity for electricity uptake and delivery.

For the negative half-cell electrolyte, the resulting negative partial state-of-charge  $SOC_{2/3}$  defines the ratio of the present concentration of  $V^{2+}$  and the sum of the  $V^{2+}$  and  $V^{3+}$  concentration. The partial state-of-charge of the positive half-cell  $SOC_{4/5}$  is obtained by division of the actual  $V^{5+}$  concentration by the sum of the  $V^{4+}$  and  $V^{5+}$  concentration. Generally, the sum of all vanadium species in the considered half-cell is also designated as the total vanadium concentration  $[V_{total}]$ . The relationships for both partial SOC's are given by the following equations:

$$\text{Negative partial state of charge: } SOC_{2/3} = \frac{[V^{2+}]}{[V^{2+}] + [V^{3+}]} = \frac{[V^{2+}]}{[V_{total}]} \quad (8)$$

$$\text{Positive partial state of charge: } SOC_{4/5} = \frac{[V^{5+}]}{[V^{4+}] + [V^{5+}]} = \frac{[V^{5+}]}{[V_{total}]} \quad (9)$$

If the VRFB is completely discharged, only  $V^{3+}$  species are present in the negative half-cell. In the positive half-cell solely  $V^{4+}$  ions are existent. According to Eq. 8 and 9, the two resulting partial SOC's amount to 0.0. Contrarily, if the VRFB is fully charged, only  $V^{2+}$  and  $V^{5+}$  are available in the anolyte and catholyte respectively. In this case the state-of-charge is 1.0 for both half-cell electrolytes. Additionally, a ratio of 50:50 of  $V^{2+}/V^{3+}$  for the negative electrolyte and of  $V^{4+}/V^{5+}$  for the positive electrolyte results in two partial SOC's of 0.5. Thus, the theoretically explorable SOC range of a VRFB lies within the boundary of 0.0 and 1.0.

Accordingly, the measured electrolyte's SOC depends on the current average oxidation state of the contained vanadium ions and subsequently the electrolyte's present potential. A special case is the commercially available vanadium electrolyte already dealt with in chapter 2.2.1. This electrolyte comprises  $V^{3+}$  and  $V^{4+}$  in a 50:50 mixture for each half-cell. Therefore, the derived SOC's are -0.5. By means of the preparatory procedure described in chapter 2.2.1, both partial SOC's are increased to 0.0 to enable efficient VRFB operation.

## 2.5 State-of-the-art SOC determination techniques

A number of methods for the SOC determination have been discussed in the literature so far. Frequently examined approaches are situated in the electrochemical and optical research field. Besides, less common methods using ultrasound are investigated. Generally, the SOC determination techniques are distinguished concerning their ex-situ application or their installation directly in the battery system (in-situ).

An ex-situ SOC determination is realized by the intervention in the VRFB's continuous operation. One central disadvantage is the time lag due to the sampling, which leads to inaccuracies of the SOC predictions. Additionally, after the sample extraction and subsequent SOC determination the electrolyte sample preparation-related is returned incompletely into the battery circulation. Therefore, the volumes of the two examined half-cell electrolytes are decreasing during operation. The removal of electrolyte as well as the thereby potentially triggered formation of volume differences between the half-cells reduces the available VRFB capacity.

Moreover, some analytical procedures interact with the electrolyte to a certain degree. Consequently once chemical reactions are induced, the vanadium electrolyte and/or the SOC sensor itself are chemically altered or damaged. The necessary maintenance of the VRFB requires the restricted operation or a complete shutdown of the VRFB apparatus. Thus, the increased temporal and financial expenditure for the battery operation significantly lowers the overall system efficiency.

To sum up, for the efficient SOC determination the time lag, electrolyte loss or damage should be avoided and the system's maintenance expense should be minimized. A promising approach could be the in-situ application of the SOC sensor combined with the protection of its hardware against destruction induced by the chemically aggressive electrolyte.

A central challenge is the determination of the differently oxidized vanadium species. The potentiometric titration enables the determination of every vanadium species and the distinction between their oxidation states. Therefore, this wet-chemical method is commonly regarded as the most reliable method for the SOC determination and serves as a benchmark for the other SOC determination methods presented in the following sections. A general drawback of this classical method is its ex-situ application and the need of chemical expertise for its operation. This is not a problem for its application by the VRFB manufacturer or in a chemical plant, but confronts the other end customers with major difficulties.

### 2.5.1 Electrochemical techniques

#### Open-circuit-voltage (OCV)

As discussed in chapter 2.4, the electrolyte's potential change during charging operation is a characteristic feature of the redox flow batteries. Therefore, this property is further investigated with regard to the SOC determination. Currently, the most frequently applied technique for SOC sensing is based on the in-situ measurement of the open-circuit-voltage [120,121].

Generally, a corresponding OCV measuring cell incorporates two electrodes made of e. g. graphite felt, which are separated by an ion-selective membrane. The OCV technique measures the potential difference of the positive and the negative half-cell at the graphite felt electrodes at zero current. Proportionally to the amount of stored electric energy the OCV value increases. By means of calibration methods like coulomb counting and the use of samples of known composition the OCV values are converted into the corresponding SOCs.

The determination of the individual half-cell potentials is not enabled. Thus, a crucial shortcoming of this method is the determination of the overall SOC of the VRFB system [120,121]. Therefore, the partial SOCs are not accessible with the OCV approach and the electrolyte's condition in each half-cell remains unknown. Besides, in case of the long-term application, the graphite felts are slowly oxidized and have to be replaced. Otherwise, a chemical aging related drift of the OCV value will occur [122,123].

#### Open-circuit-potential (OCP)

A possible solution to overcome the OCV method's inability to perform partial SOC determinations is the in-situ measurement of the half-cell specific open-circuit-potential (OCP) [124-126]. The OCP sensor consists of a working electrode and a reference electrode. By means of this two-electrode-setup the potential of the working electrode is determined relating to the reference electrode's constant potential at high resistance. This procedure is conducted for each VRFB half-cell separately.

In case of the VRFB's positive half-cell its potential increases during charging operation. For the negative half-cell an OCP decrease is observed concerning the battery charging [124-126]. Consequently, partial SOCs are obtained via calibration as introduced for the OCV sensing. Additionally, the description of the potential curve with help of the Nernst equation is investigated. This model deviates from the experimental data, especially due to the neglect of the alteration of the proton concentration or the absence of standard conditions [124,125].

In case of the chemically aggressive electrolyte a central challenge is to protect the working electrode and the reference electrode against this acidic environment. For the working electrodes with a metallic basic structure like e. g. copper noble metals are deposited onto the surface by means of electroplating.

Unfortunately, the noble metals like platinum or gold catalyze the auto-oxidation of the  $V^{2+}$  ions to  $V^{3+}$  [127,128]. The prevention of the electrolyte alteration by this  $V^{2+}$  auto-oxidation is achieved by minimizing the contact area between the noble metals and the vanadium electrolyte. Another possibility is the application of graphite felt electrodes. These graphite felt electrodes do not trigger the  $V^{2+}$  auto-oxidation, but they are slightly oxidized by the VRFB electrolyte during usage over an extended period. Therefore, a continuously weak change in the working electrode potential has to be considered or they have to be exchanged during maintenance of the VRFB system [122,123].

Moreover, the applied reference electrode has to show long term stability in the electrolyte. To obtain reliable SOC values in the aggressive VRFB electrolyte, all the reference electrode materials have to be permanently resistant and the reference electrode's potential has to stay invariably fixed. Until now, a reference electrode which is covering both requirements is not commercially available or published in literature. Especially the problem of the drifting reference electrode potential remains unsolved [124,125].

### Electrical conductivity

Besides the investigation of the electrolyte's potential, the in-situ observation of the electrolyte's conductivity changes during charging of the battery is also examined in literature [85,124,130-132]. In the highly acidic vanadium electrolyte the conductivity is mainly attributed to the incorporated protons. Their far highest ionic conductivity compared to the other ions in solution is based on the Grotthus mechanism [129]. Therefore, the conductivity changes during the charging process are caused by a continuous increase in the proton concentration in both VRFB half-cells. Within the charging operation two protons are formed in the positive half-cell of the VRFB in a single oxidation step of  $V^{4+}$  to  $V^{5+}$  (see chapter 2.2.1, Eq. 2). One of them is migrating through the ion-selective membrane into the negative half-cell for charge balancing. Thus, within each oxidation step of  $V^{4+}$  to  $V^{5+}$  the conductivity increases due to the additionally present proton in each of the two half-cells.

Generally, the conductivity in solution is determined between two electrodes with exactly known distance. Similar to the OCP, the conductivity measurements are applicable at both half-cells separately. The calibration towards SOC values is proceeded via samples of defined concentration or coulomb counting. Thus, partial SOCs are accessible [85,124,130-132]. Additionally, the used electrodes have to be protected against the highly corrosive electrolyte like the components of the OCP sensor. Consequently, the metallic electrodes are electroplated with noble metals and their contact area to the vanadium electrolyte is minimized due to their auto-catalyzing properties [127-128]. In case of the application of graphite electrodes the exchange of already oxidized exemplars has to be proceeded within the maintenance [122,123].

A benefit of the introduced electrochemical SOC sensing techniques is their ability of in-situ application which allows instant SOC determination without time lag. The main drawbacks are their temperature dependence and the present unavailability of suitable electrode materials (chemically inert and sufficiently electrical conductive) which are necessary for the long-term stability and subsequently the long-term reliability of the SOC sensor.

## 2.5.2 Optical strategies

As described in chapter 2.3.1, the vanadium chemistry in aqueous solution comprises four vanadium oxidation states. Within the range of  $V^{2+}$  to  $V^{5+}$  the increase of the vanadium ionic charge induces an alteration of the shape of the ions' corresponding coordination spheres [133]. Due to these distortions in the coordination octahedrons like the Jahn-Teller distortions [134] the energy levels of the involved central ion orbitals are changed. These energy level changes trigger a shift in the wavelength range of the radiation absorption by the incorporated valence electrons.

The wavelengths/colors and intensities of the absorbed radiation and alterations of the latter can be determined by optical spectrometry. Additionally, the transmitted complementary colors of the examined vanadium complexes' absorbed radiation are visually visible [133]. Thus, the used spectroscopic approaches are situated in the field of transmission or absorbance measurements. Due to the previously discussed alterations of the electrons' energy levels during VRFB charging, the absorption evolution of different electromagnetic radiation types by the vanadium valence electrons is investigated.

### UV/Vis transmission spectrometry

Several optical approaches are presented in the scientific publications. Among other methods, the UV/Vis transmission of the vanadium electrolyte is investigated by Liu et al. and Zhang et al. [135,136]. By means of a customized spectrometer and an in-house developed flow-through optical quartz cell (optical path length:  $d = 1$  mm [135],  $d = 0.5$  mm [136]) in-situ transmission measurements are conducted.

The transmission of both half-cell electrolytes is monitored separately and reveals non-linear variations. Thus, partial SOC values are obtained after correlation with spectra of known state-of-charge. For this purpose a correlation analysis is performed [135,136]. The measured transmission spectrum is compared to SOC-related measurements of a database. Based on the highest degree of accordance, the measured spectrum is assigned to the particular state-of-charge value indicated in the database. The analyzed electrolyte samples are produced by mixing of the appropriate amounts of fully charged and completely discharged electrolyte [135,136].

The indirect SOC determination increases the demands on the hardware performance for the assignment algorithm and potentially reduces the accuracy of SOC prediction due to errors during the assignment. Besides, the flow-through optical cell is the only part of the SOC sensor, which comes into contact with the aggressive vanadium electrolyte. The use of chemically inert glass windows for the flow-through optical cell significantly increases the durability of the SOC sensor, if the rest of the optical cell e.g. sealings exhibits also adequate chemical resistance. In this case long-term durability and long-term operational capability of the SOC sensor are achievable.

### UV/Vis absorbance spectrometry

Another method for the optical SOC sensing is the determination of the UV/Vis absorbance of the vanadium electrolyte [132,137-142]. The published experiments are conducted ex-situ utilizing quartz cells with an optical path length of  $d = 1$  mm for diluted vanadium electrolyte [137-139] and  $d = 0.2$  mm [138-139] for higher concentrated samples ( $[V]$  above  $1 \text{ mol L}^{-1}$ ). Previous studies consistently use cuvette path lengths of  $d = 10$  mm [132], which is clearly oversized for the optically dense electrolyte. Only commercially available standalone spectrometers without customization are used.

For the ex-situ UV/Vis absorbance measurements the studied vanadium samples are obtained by electrochemical oxidation or reduction of a  $V^{4+}$  stock solution. The endpoint of the oxidation and the reduction is defined by the measurement of the potential of a carbon electrode and additionally checked by the electrolyte's color changes [132,137-139].

Generally, the negative as well as the positive electrolyte can be investigated. A calibration at two different wavelengths with samples of known concentration is applied to handle the non-linear variations of the positive electrolyte. Thus, partial SOC values are accessible [137-142]. Therefore, the samples are removed from the VRFB circuit. Then, they are transferred to the spectrometer and measured subsequently. Especially for the negative half-cell electrolyte this procedure is highly error-prone due to the oxidation of  $V^{2+}$  by atmospheric oxygen. The return of the collected samples into the VRFB circulation cannot be realized entirely. Thus, the volumes in the half-cells are changed (negligible in practice).

Additionally, the time lag of the ex-situ procedure reduces the efficiency and precision compared to online approaches. Besides, due to the missing automatization of the ex-situ procedure an operator is necessary for execution of the measurements which increases financial outlay. In case of an optimized sensor set-up (e. g. in terms of optical path length, light source output and sensitivity of the detector) characteristic species-specific absorbance peaks depending on the vanadium oxidation state are accessible.

### IR transmission spectrometry

Besides the already discussed contributions covering the vanadium electrolyte's UV/Vis absorption Rudolph et al. studied the corresponding in-situ IR transmission at a wavelength of 950 nm [143]. The used in-house constructed sensor set-up consists of an IR LED light source, an IR detector diode and a cylindrical-shaped glass tube used as flow-through cuvette. Both the light source and detector are mounted opposite to each other on the glass tube to profit from its focusing lens effect during IR transmission monitoring. Unfortunately, the glass tube's diameter is not specified [143].

The calibration of the SOC sensor is conducted during VRFB operation. By means of parallel measurements of the open-circuit-potential a dependence on the IR transmission is obtained based on the oxidation state specific signals of the vanadium ions. Both the negative and the positive half-cell electrolytes are investigated by two identical sensors. Whereas the negative half-cell electrolyte sensor clearly detects SOC differences, the positive half-cell sensor only shows insufficient response to alterations of the positive electrolyte's oxidation state [143].

Consequently, reliable partial SOC monitoring is not possible with this set-up. Due to the application of an IR LED the resulting emitted wavelength range is narrow and not suitable for recording spectra or determining species-specific signal peaks. An advantage of this economical technique is the beneficial focusing lens effect of the glass tube and the in-situ applicability [143].

#### X-ray near-edge absorption spectroscopy

A special case of a SOC determination method is the synchrotron-based in-situ X-ray near-edge absorption spectroscopy (XANES) explored by Jia et al. [144]. The XANES technique is used to study the X-ray absorption of the vanadium valence electrons. Under common VRFB cycling conditions the valence state evolution of the vanadium species of both the negative and positive half-cell electrolyte is observed [144].

The X-ray source is positioned opposite to the detector. In between these two parts the kapton tubes of both half-cell electrolyte circulations are located. In the experiment the X-ray alterations caused by their penetration of the two electrolytes are monitored separately. The interpretation of the measurements delivers the corresponding vanadium average oxidation state [144]. Thus, partial SOC's are accessible. By means of the evaluation of the obtained results the successive charge-discharge profile during battery cycling is optimized [144].

Due to the considerable financial efforts for the construction and operation of the XANES SOC sensing and the X-ray-related safety issues the technique is not suitable for an application in commercially available VRFB systems. Contrarily, the fields of application are situated in the area of research and development considering the optimization of the VRFB's operating parameters. The in-situ applicability and the access to the average oxidation states of the vanadium ions are central favorable aspects of this approach [144].

### 2.5.3 Additional approaches

#### Ultrasonic velocity sensing

Chou et al. investigated the in-situ ultrasound velocity sensing during VRFB operation for SOC determination [145]. While the VRFB is charged or discharged the chemical transitions of the vanadium species in the electrolyte change its density. By means of this method alterations in the ultrasound speed are registered, induced by changes in the electrolyte density or temperature [145].

Therefore, an ultrasound transmitter and a corresponding receiver are mounted opposite to each other directly on the flow tube of both electrolyte cycles. With this set-up the duration of the ultrasonic pulse's crossing through the electrolytes in the flow tube is measured. Consequently, the actual ultrasonic velocity can be determined individually for each half-cell [145]. Via coulomb counting the ultrasonic velocity results are linked to partial SOC values.

A general issue of this approach is the temperature-dependence of the ultrasonic velocity measurement which has to be considered to obtain reliable SOC predictions. The in-situ and half-cell specific scopes are advantageous [145]. Apart from this ultrasonic approach, several ex-situ density measurements are conducted gravimetrically by Mousa and Skyllas-Kazacos via weighing of accurately determined volumes of vanadium electrolyte [146].

#### Viscosity measurements

The viscosity of differently concentrated  $V^{5+}$  electrolytes is examined by Kausar [130]. Therefore, the viscosity of the vanadium samples is determined ex-situ by means of a U-tube Ostwald capillary viscometer. With the viscometer the retention time of the considered samples is measured. Then, the retention time is multiplied by the viscometer constant to obtain the viscosity [130].

An increase in viscosity proportional to the  $V^{5+}$  concentration is observed. The samples are generated in a VRFB by electrochemical oxidation of a  $V^{4+}$  solution. Their concentration is determined by coulomb counting and the solution's color [130]. Measurements at different SOC values are not conducted. Thus, partial SOC determinations are excluded.

Additionally, the viscosity evolution also shows a dependence on the sulfate counter ion concentration in the electrolyte as well as on the temperature changes [130]. These two challenges together with the missing in-situ applicability illustrate the necessity of further research on this field [130].

## 2.6 Research objective

The central objective of this PhD thesis is the development of an improved state-of-charge sensor for the all-vanadium redox flow battery. Significant potential for improvement of the current VRFB technology is located in the fields of development such as the accessibility to half-cell specific partial state-of-charge information and the ability to perform vanadium species specific SOC sensing. Both capabilities are leading to substantially profound insights in the evolution of the VRFB electrolyte's chemical composition during charge-discharge cycling of the battery. Additionally, the permanent protection of the SOC sensor's hardware against the highly corrosive vanadium electrolyte is of crucial interest. The more resistance of the applied material with direct contact to the electrolyte is realized, the less frequently the repair efforts on the battery will occur. To achieve the previously addressed improvements two different approaches are discussed in this dissertation.

The first approach which combines in-situ UV/Vis/NIR absorbance spectrometry with in-situ open-circuit-voltage measurements for in-operando partial SOC monitoring is introduced in chapter 3. Firstly, the values of an open-circuit-voltage curve are measured during charging of a concentrated pristine vanadium electrolyte (total vanadium concentration =  $1.6 \text{ mol L}^{-1}$ ) in a VRFB single cell. The obtained OCV curve is mathematically described and related to the SOC by a fit function based on Nernst's equation. In the fit procedure the absence of standard conditions concerning the vanadium electrolyte is considered as well as the proton formation and consumption during charge-discharge cycling. Due to the parallel operation of the UV/Vis/NIR absorbance spectrometry and the OCV measurement, the calibration of the UV/Vis/NIR spectroscopic sensor is conducted by means of the SOC-related OCV values. This calibration is performed in-operando and individually for both half-cell electrolytes. Therefore, partial SOC values are obtained. Besides, a durable quartz flow-through cell with optimized path length is applied in the absorbance measurements. Consequently, the SOC sensor's long-term applicability, the distinction between the different vanadium oxidation states and the determination of their present concentrations are achieved.

The second approach is dealing with potentiometric titration coupled with simultaneously conducted UV/Vis/NIR absorbance spectroscopy and is discussed in chapter 4. During the potentiometric titration the UV/Vis/NIR spectra are recorded in-situ via an optical quartz immersion probe. A  $V^{2+}$  solution sample of a fully charged VRFB negative electrolyte is used as titrand. The titrant is a  $0.2 \text{ mol L}^{-1} \text{ KMnO}_4$  solution. The study covers eight different total vanadium concentrations in the range of  $0.2 \text{ mol L}^{-1}$  to  $1.6 \text{ mol L}^{-1}$ . Due to this combined technique the absorbance peaks of  $V^{2+}$  and  $V^{3+}$  are obtained. Subsequently, their absorption coefficients at precisely determined total vanadium concentrations are accessible. The challenging determination of the absorption coefficient of the oxidation-sensitive  $V^{2+}$  species is accomplished via an extrapolation procedure described in detail in chapter 4.2.4. Due to this extrapolation technique, there is no necessity to operate under inert gas atmosphere for the sample preparation and its transfer into the titration set-up. Because of the mixed-valence  $V^{4+}$ - $V^{5+}$  complex formation in highly concentrated vanadium catholytes [147] only the negative partial SOC of the anolyte is accessible. Henceforth, by means of photometry and the obtained absorption coefficients the SOC of the VRFB anolyte can be determined directly within the whole total vanadium concentration range of  $0.2 \text{ mol L}^{-1}$  to  $1.6 \text{ mol L}^{-1}$ .

### 3. In-situ spectrometric State-of-Charge determination

SOC monitoring via UV/Vis absorbance spectroscopy is usually conducted ex-situ [137-142] which is insufficient for the in-operando SOC determination in VRFB systems. Especially the ex-situ SOC determinations in the negative half-cell electrolyte (anolyte) are inadequate due to the oxygen sensitivity of the  $V^{2+}$  species. Besides, the SOC monitoring of the positive half-cell electrolyte (catholyte) is complicated because of the intermediate binuclear complex formation and depletion during charge-discharge cycling [147]. For this purpose an in-situ UV/Vis/NIR state-of-charge sensor is developed to allow half-cell specific SOC monitoring directly during the VRFB operation and the protection against atmospheric  $V^{2+}$  oxidation as discussed below.

#### 3.1 Experimental

##### 3.1.1 Electrolyte

The applied vanadium electrolyte produced by GfE (Gesellschaft für Elektrometallurgie mbH, Germany) contains  $1.6 \text{ mol L}^{-1}$  vanadium ions (a 50:50% mole fraction of  $V^{3+}$  and  $V^{4+}$ ) and  $2.0 \text{ mol L}^{-1}$  sulfuric acid according to the manufacturer. Further  $2 \text{ mol L}^{-1}$  sulfate ions are originating from the vanadium sulfates dissolved in the  $2.0 \text{ mol L}^{-1}$  sulfuric acid during the electrolyte production. Thus, the total sulfate concentration is  $4 \text{ mol L}^{-1}$  [148].

Additionally, this commercially available electrolyte contains  $0.05 \text{ mol L}^{-1}$  of phosphoric acid. The total vanadium concentration of the commercial electrolyte is determined by means of ICP-OES and gives  $1.624 \text{ mol L}^{-1}$ . This determination is additionally conducted by potentiometric titration and yields  $1.597 \text{ mol L}^{-1}$  [148].

Before battery operation, the negative half-cell electrolyte/anolyte is purged with nitrogen gas (purity 99.99 vol.%) for 3 min to remove dissolved oxygen gas. After that, the anolyte is covered with paraffin oil to prevent oxidation by atmospheric oxygen of the  $V^{2+}$ -species to be generated. The positive and negative half-cell electrolytes are continuously agitated with magnetic stirrers to guarantee homogeneity within the electrolyte vessels [148].

##### 3.1.2 Membrane

The positive and negative half-cells of the VRFB single cell are separated by a Fumasep F-1850 cation exchange membrane (FUMATECH BWT GmbH, Germany). This cation exchange membrane is pretreated by the immersion in  $2 \text{ mol L}^{-1}$  sulfuric acid for 6 h to improve its proton conductivity [148].

### 3.1.3 Electrode felts and current collectors

Graphite felts (GFD 4.6, SGL Carbon GmbH, Germany) are utilized as VRFB electrodes with a thickness of 4.6 mm and a geometrical area of 10 cm<sup>2</sup>. Prior to their application in the battery, the graphite felts are thermo-chemically activated. Thus, the felts are immersed in concentrated sulfuric acid (96%, Merck, Germany) for 20 h [148]. Then, they are washed with distilled water, dried and oxidized in an oven (B150, Nabertherm GmbH, Germany) for 30 h at 400 °C and ambient atmosphere.

The used current collectors are made of a graphite-based bipolar plate material (PPG86, Eisenhuth GmbH Co. KG, Germany) equipped with a simple flow field. Before application, these bipolar plates are slightly abraded with emery paper [148].

### 3.1.4 Construction material

The three dimensionally printed polyaniline end plates of the VRFB with integrated electrolyte channels are equipped with Teflon Swagelok fittings (Swagelok Company, USA) and connected to the other parts of the battery circuit by Tygon tubings (ISMATEC, IDEX Health & Science GmbH, Germany). The Tygon tubings have an inner diameter of 3 mm [148].

### 3.1.5 VRFB single cell

In Fig. 7 an exploded-view drawing of the applied VRFB single cell is displayed. From the inside out it consists of an ion-selective membrane, two graphite felt electrodes with rectangular sealings, two graphite-based bipolar plates with sealing rings and two adjacent gold-plated copper current collectors. The two 3D printed polyaniline end plates fix the positions of the inner VRFB parts by means of screws and nuts.

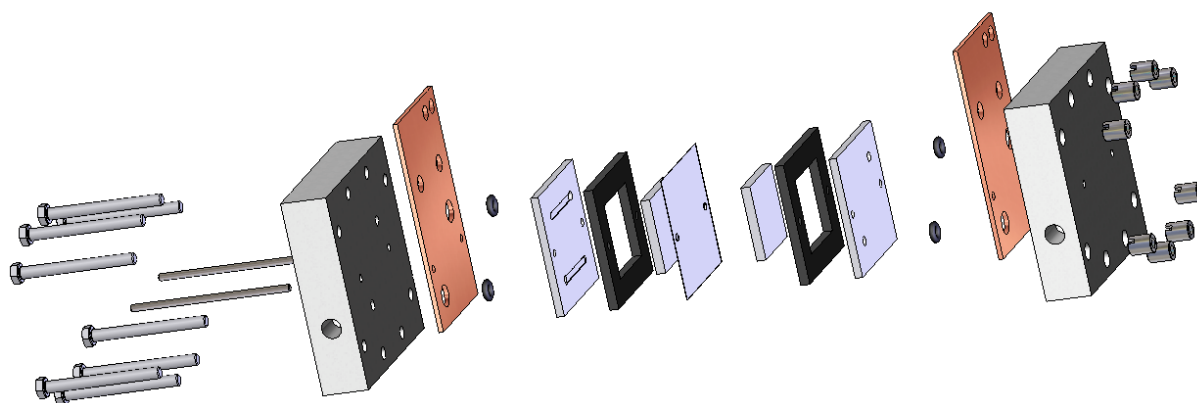


*Fig. 7. Exploded-view drawing of the applied VRFB single cell.*

### 3.1.6 Laboratory VRFB set-up

The specifically developed battery circuit (see Figure 8) contains an in-house-constructed all-vanadium redox flow battery and two electrolyte glass vessels. One glass vessel is applied for the negative and the positive half-cell electrolyte, respectively, (anolyte and catholyte) and is equipped with magnetic stirrers [148].

A two channel peristaltic pump (ISMATEC REGLO Analog, Cole-Parmer GmbH, Germany) ensures electrolyte circulation through the experimental set-up with controlled flow rate for both catholyte and anolyte simultaneously. An electrolyte volume of 30 mL is utilized in each half-cell. The corresponding electrolyte flow rate is adjusted to 10 mL min<sup>-1</sup> [148].

A smaller in-house-constructed VRFB is installed in the battery circulation as a flow-through open-circuit-voltage (OCV) cell for online in-situ OCV measurements. In the anolyte as well as in the catholyte battery circuit a flow-through cuvette (170.700-QS, Hellma Analytics, Germany) is integrated to enable online in-situ absorbance measurements [148].

As described in the subsequent procedure, the OCV cell voltage values are related to distinct state-of-charge values by means of a derived fit function based on Nernst's equation. Due to these calibrated flow-through OCV cell voltages as input for a potentiostat (VMP3, BioLogic Science Instruments, France) it is possible to specifically charge both vanadium electrolytes to defined values of state-of-charge [148].

In the following the spectrometric determinations of SOC<sub>2/3</sub> and SOC<sub>4/5</sub> are conducted in 0.05 SOC steps in the range of 0.0 ≤ SOC ≤ 0.8. Accordingly, a SOC = 0.0 implies that only V<sup>4+</sup> ions are present in the positive electrolyte and solely V<sup>3+</sup> ions appear in the negative electrolyte. The indication -0.5 ≤ SOC < 0.0 represents mixtures of V<sup>3+</sup> and V<sup>4+</sup> ions in variable proportions for the negative and the positive half-cell electrolyte respectively [148].

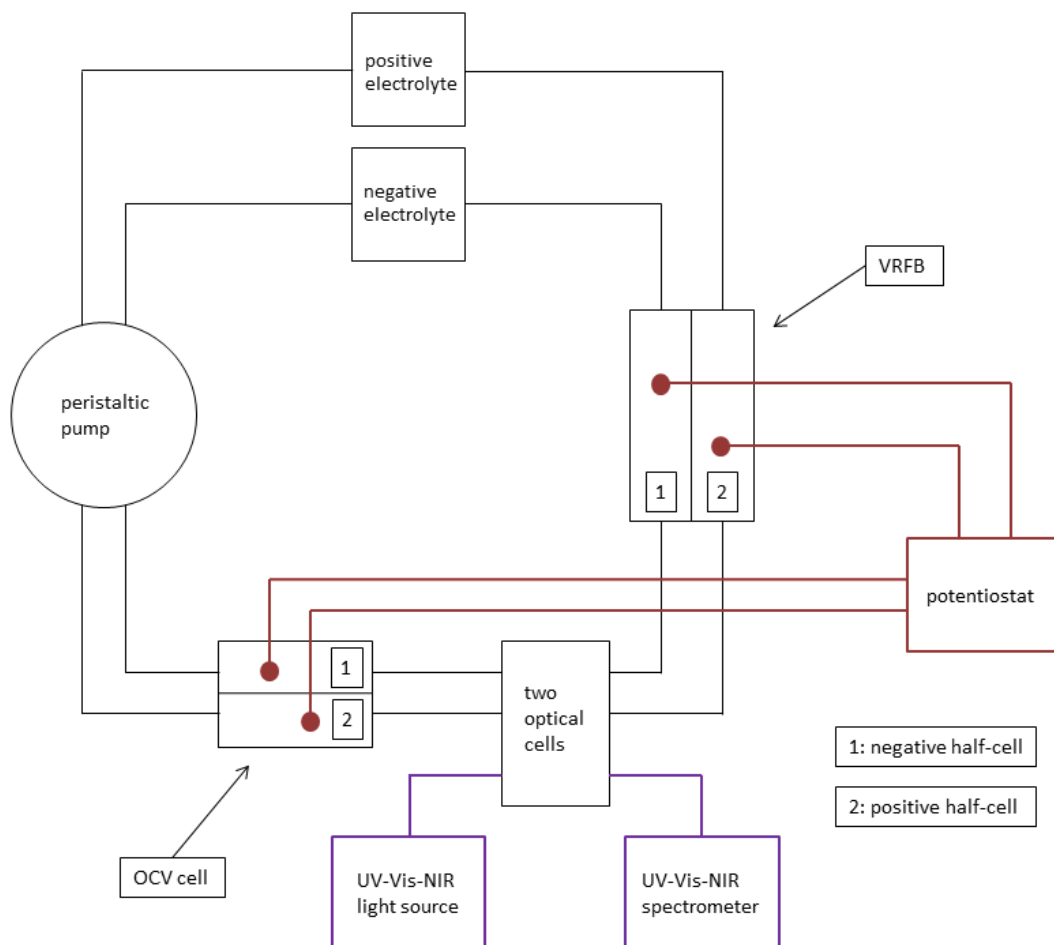
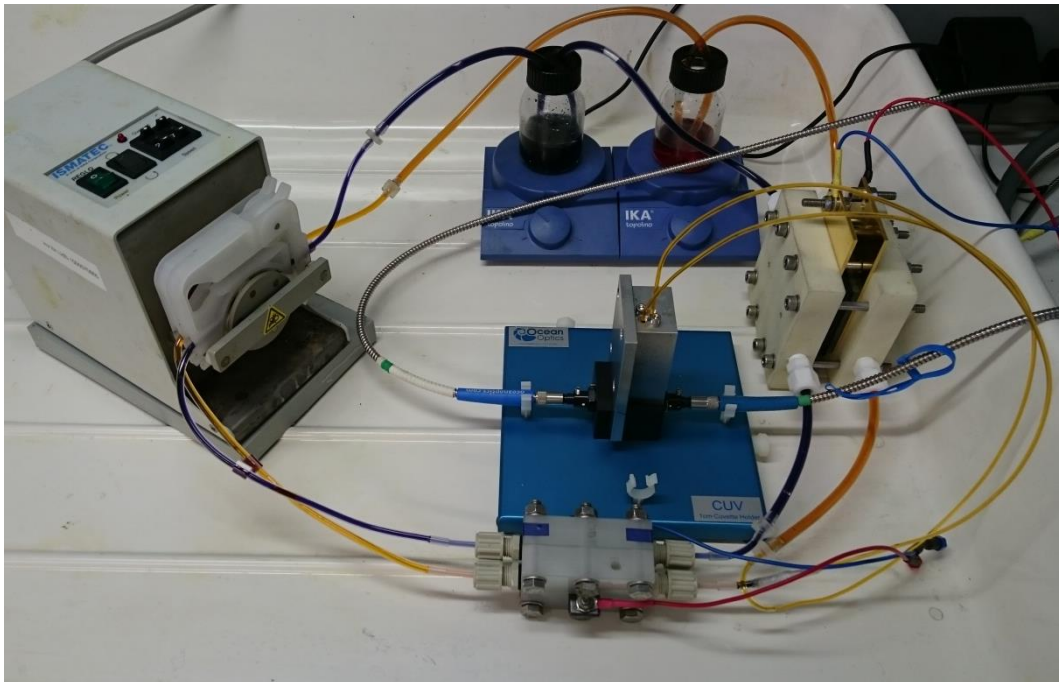
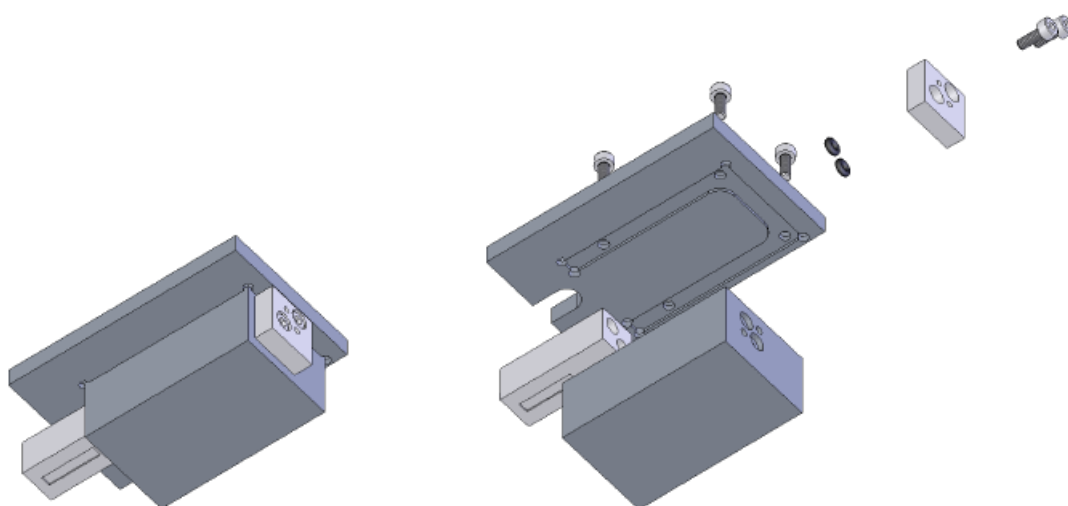


Fig. 8. Experimental laboratory set-up for the online in-situ absorbance measurements (above) and the corresponding schematical layout (below) [148].

### 3.1.7 UV/Vis/NIR spectroscopic set-up

The UV/Vis/NIR spectral data are recorded during the charging operation of the VRFB single cell by means of a modular in-situ UV/Vis/NIR experimental set-up (see Fig. 8). The used UV/Vis/NIR spectrometer (HR2000+, Ocean Optics, USA) is connected to the separate light source DH-2000-BAL (Ocean Optics, USA). This separate light source includes a deuterium lamp and a halogen lamp to sufficiently cover the ultraviolet, visible and near infrared spectral ranges [148]. Besides, a system of internal mirrors and filters removes the pronounced D-alpha line at 655 nm in the UV lamp emission spectrum to prevent saturation of the spectrometer detector [149].

Between the described UV/Vis/NIR light source and the UV/Vis/NIR spectrometer a cuvette holder (CUV, Ocean Optics, USA) is connected. The original cover of this cuvette holder is replaced by an in-house designed flow-through supporting cover equipped with two boreholes for electrolyte inlet and outlet (see Fig. 9) [148].



*Fig. 9. Flow-through supporting cuvette cover incorporating a flow-through cuvette in the assembled state (left); the corresponding exploded-view drawing of the cover (right).*

The flow-through cuvette (170.700-QS, Hellma Analytics, Germany, optical path length: 200  $\mu\text{m}$ ) located inside the cuvette holder is directly integrated into the VRFB circulation. Every optical component of the spectrometric set-up is connected with shielded glass fiber optical cables (Ocean Optics, USA) using a glass fiber diameter of 100  $\mu\text{m}$  [148].

Prior to starting with the absorbance (abs) measurements the light source is allowed to warm up for 45 min to achieve a stationary thermal state. For control of the spectrometric set-up the software OceanView 1.5.2 (Ocean Optics, USA) is applied. The integration time for the spectra is adjusted to 6 ms. Eventually, the obtained spectrum results from five recorded scans within the wavelength range  $300 \text{ nm} \leq \lambda \leq 1000 \text{ nm}$  [148].

## 3.2 Results and discussion

### 3.2.1 Description of OCV values with the Nernst equation

#### Derivation of the relevant Nernst equations for both VRFB half-cells

The OCV cell voltages are linked to specific state-of-charge values by means of a fit function based on Nernst's equation [124]. In the negative half-cell of the VRFB the following reduction is proceeding during the charging process:



Thus, the  $V^{2+}$  concentration is directly proportional to the negative partial state-of-charge  $SOC_{2/3}$ :

$$[V^{2+}] = SOC_{2/3} * [V_{total}] \quad (11)$$

where  $[V^{2+}]$  = the actual  $V^{2+}$  concentration in the negative half-cell and  $[V_{total}]$  = the total vanadium concentration in the negative half-cell [148].

Accordingly, the  $V^{3+}$  species is related to  $SOC_{2/3}$  by

$$[V^{3+}] = (1 - SOC_{2/3}) * [V_{total}] \quad (12)$$

where  $[V^{3+}]$  = the actual  $V^{3+}$  concentration in the negative half-cell [124].

Nernst's equation describes the negative half-cell potential  $E_{2/3}$  of the VRFB as:

$$E_{2/3} = E_{2/3}^0 + \frac{RT}{zF} * \ln \frac{[V^{3+}]}{[V^{2+}]} \quad (13)$$

with  $E_{2/3}^0$  = the standard reduction potential for the vanadium redox couple  $V^{2+}/V^{3+}$ ,  $z$  = the number of electrons transferred in the cell reaction;  $R$ ,  $T$  and  $F$  have the usual meanings. In Eq. 13 concentrations instead of activities are used assuming that the activity coefficients of the two vanadium species are very similar and therefore essentially cancel [148].

The insertion of equation (11) and (12) into Nernst's equation (13) yields the following potential at room temperature:

$$E_{2/3} = E_{2/3}^0 + \frac{RT}{zF} * \ln \frac{1-SOC_{2/3}}{SOC_{2/3}} = E_{2/3}^0 + 0.059 * \log \frac{1-SOC_{2/3}}{SOC_{2/3}} \quad (14)$$

Consequently, equation (14) describes the relationship between the negative partial  $SOC_{2/3}$  and the negative half-cell potential  $E_{2/3}$ .

In the VRFB's positive half-cell the subsequent oxidation is taking place during the charging operation:



Thus, the  $VO_2^+$  concentration ( $V^{5+}$ -species) is directly proportional to the positive partial state-of-charge  $SOC_{4/5}$ :

$$[VO_2^+] = SOC_{4/5} * [V_{total}] \quad (16)$$

with  $[VO_2^+]$  = the actual concentration of the  $V^{5+}$ -species in the battery and  $[V_{total}]$  = the total vanadium concentration.

As discussed in the following, in case of high vanadium concentrations in the VRFB electrolyte, a certain part of the  $VO_2^+$  cations and the  $VO^{2+}$  cations is present in form of binuclear  $V^{4+}/V^{5+}$  mixed-valence complexes [147,148]. However, noticeable negative effects on the electrochemistry of the electrolyte are not observed.

The  $VO^{2+}$  species is related to  $SOC_{4/5}$  by:

$$[VO^{2+}] = (1 - SOC_{4/5}) * [V_{total}] \quad (17)$$

with  $[VO^{2+}]$  = the actual  $VO^{2+}$  concentration ( $V^{4+}$ -species) in the battery.

Consequently, the positive half-cell potential  $E_{4/5}$  of the VRFB is obtained as:

$$E_{4/5} = E_{4/5}^0 - \frac{RT}{zF} * \ln \frac{[VO^{2+}]}{[VO_2^+] * ([H^+]/mol \cdot L^{-1})^2} \quad (18)$$

with  $E_{4/5}^0$  = the standard reduction potential for the vanadium redox couple  $V^{4+}/V^{5+}$ ,  $[H^+]$  = the proton concentration in the vanadium electrolyte,  $z$  = the number of electrons transferred in the cell reaction;  $R$ ,  $T$  and  $F$  have the usual meanings.

Remarkably, the positive half-cell potential  $E_{4/5}$  strongly depends on the current proton concentration  $[H^+]$  in the corresponding vanadium electrolyte. Thus, the  $H^+$  concentration is increasing in the positive half-cell during the charging process of the VRFB [148]. As stated before, the activity coefficients of both vanadium species are assumed to essentially cancel because of very similar magnitude. Contrarily, the activity of the protons is considered in the following paragraphs.

According to equation (15) two protons are formed every time a  $VO^{2+}$  ion is oxidized to  $VO_2^+$  in the positive half-cell electrolyte during increasing the  $SOC_{4/5}$ . One of these two protons diffuses through the ion-selective membrane into the negative half-cell electrolyte for charge balancing [148]. Consequently, each time a  $V^{4+}$  cation is oxidized to a  $V^{5+}$  cation, the proton concentration  $[H^+]$  is increased to the same extent in both half-cell electrolytes.

However, to meet the requirements of the positive half-cell reaction for the charging operation given by equation (15) an increase of two protons instead of one proton is considered. Thus, the  $H^+$ -diffusion from the positive to the negative half-cell electrolyte is not incorporated in the concerned half-cell reactions [148]. But this imprecision is completely leveling out at the stage of electromotive force calculation by the subtraction of the half-cell potentials  $E_{2/3}$  from  $E_{4/5}$ .

Besides, the actual proton concentration in the electrolyte can be described as being composed of a static and a dynamic part [124]. The  $H^+$  concentration originating from the sulfuric acid  $H_2SO_4$  at  $SOC_{4/5} = 0$  (abbreviation:  $[H_2SO_4]_0$ ) is constant and represents the static part of the proton contribution [148]. As placeholder for the dynamic part of the proton concentration the  $V^{5+}$  cation  $[VO_2^+]$  is applied because the rates of increase of the two species  $[VO_2^+]$  and  $[H^+]$  are identical:

$$[H^+] = [H_2SO_4]_0 + [VO_2^+] \quad (19)$$

The insertion of equation (16) into (19) results in:

$$[H^+] = [H_2SO_4]_0 + SOC_{4/5} * [V_{total}] \quad (20)$$

The insertion of equation (16), (17) and (20) into Nernst's equation (18) leads to the relationship between the  $SOC_{4/5}$  and the positive half-cell potential  $E_{4/5}$  [148]:

$$\begin{aligned} E_{4/5} &= E_{4/5}^0 - 0.059 * \log \frac{1 - SOC_{4/5}}{SOC_{4/5} * ([H_2SO_4]_0 + SOC_{4/5} * [V_{total}])^2} \\ &= E_{4/5}^0 - 0.059 * [-\log(SOC_{4/5}) + \log(1 - SOC_{4/5}) \\ &\quad - 2 * \log([H_2SO_4]_0 + SOC_{4/5} * [V_{total}])] \end{aligned} \quad (21)$$

Thus, equation (21) defines the relationship between the positive partial  $SOC_{4/5}$  and the positive half-cell potential  $E_{4/5}$ .

Consequently, the electromotive force  $\Delta E$ , i.e. the OCV which is calculated as:

$$\Delta E = OCV = E_{4/5} - E_{2/3} \quad (22)$$

is yielded by the insertion of equation (14) and (21) into equation (22):

$$\begin{aligned} OCV &= E_{4/5}^0 - 0.059 * [-\log(SOC_{4/5}) + \log(1 - SOC_{4/5}) \\ &\quad - 2 * \log([H_2SO_4]_0 + SOC_{4/5} * [V_{total}])] \\ &\quad - (E_{2/3}^0 + 0.059 * [-\log(SOC_{2/3}) + \log(1 - SOC_{2/3})]) \end{aligned} \quad (23)$$

In the balanced state of the VRFB, when consequently  $SOC_{2/3} = SOC_{4/5} = SOC$  the following expression is obtained [148]:

$$\begin{aligned} OCV &= (E_{4/5}^0 - E_{2/3}^0) + 0.118 * [\log(SOC) - \log(1 - SOC) \\ &\quad + \log([H_2SO_4]_0 + SOC * [V_{total}])] \end{aligned} \quad (24)$$

### Selection of the initial values for the parameters used in the previously derived least-square fit function

According to the two tabulated standard reduction potentials for the positive and the negative half-cell redox pair equation (25) yields a potential difference of 1.26 V at standard conditions [24].

$$\Delta E_{SOC=0.5} = (E_{4/5}^0 - E_{2/3}^0) = \Delta E^0 \quad (25)$$

However, during the operation of the VRFB at SOC = 0.5, a potential difference of approximately 1.41 V is observed. This voltage value is applied as the initial value for the parameter  $\Delta E^0$  in the derived Nernst fit function.

A possible explanation of the discrepancy between the absolute values of the tabulated and the observed potential difference is the presence of a Donnan potential at the ion-selective membrane [148]. The generation of the Donnan potential is probably triggered by the inability of some electrolyte components to pass through the membrane. Additionally, high concentrations of vanadium and sulfuric acid and lower temperatures lead to deviations from the standard conditions.

Besides, for 2 M  $H_2SO_4$  present in the VRFB electrolyte at SOC = 0.0 (abbreviation:  $[H_2SO_4]_0$ ), the proton activity coefficient is indicated as  $\gamma = 0.124$  at a molality of 2 mol  $kg^{-1}$ . At a molality of 1 mol  $kg^{-1}$  the related activity coefficient is specified as  $\gamma = 0.130$  [148,150]. Accordingly, the difference between both activity coefficients is small. Therefore, the difference between the molality and the concentration of the substance caused by the density of 2 M  $H_2SO_4$  of 1.123 g  $cm^{-3}$  [151] is in this case negligible. Thus, the molality can be written in good approximation as the concentration of the substance:

$$a(2 M H_2SO_4) = 0.124 * 2 mol kg^{-1} \approx 0.124 * 2 mol L^{-1} = 0.248 mol L^{-1} \quad (26)$$

Consequently,  $a = 0.248 mol L^{-1}$  is taken as the initial value for  $[H_2SO_4]_0$  in the Nernst fit function. The activity of  $H_2SO_4$  is clearly different from the concentration, as described in the last paragraphs [148].

Contrarily to the  $H_2SO_4$ , in case of the vanadium species this difference between the activity and the concentration is neglected in the subsequent calculations. The Nernst fit function's initial value for the total vanadium concentration  $[V_{total}]$  is determined by ICP-OES as 1.624 mol  $L^{-1}$  (see chapter 3.1.1.) [148].

By means of these initial values, the curve of the experimental OCV values as a function of SOC (green values in Figure 10) is fitted in the range  $0 \leq SOC \leq 0.99$  with

$$OCV = \Delta E^0 + a * [\log(SOC) - \log(1 - SOC) + \log([H_2SO_4]_0 + SOC * [V_{total}])] \quad (27)$$

(see red curve in Figure 10).

The performed Nernst fit is in good agreement with the OCV curve's data [148]. The resulting fit parameters

$$\Delta E^0 = 1.4088 \text{ V}, a = 0.09483 \text{ V}, [\text{H}_2\text{SO}_4]_0 = 0.281 \text{ mol L}^{-1} \text{ and } [\text{V}_{\text{total}}] = 1.6241 \text{ mol L}^{-1}$$

differ only marginally from the estimated initial values.

With this approach, the OCV cell voltages are directly linked with their corresponding state-of-charge values of a balanced VRFB. This relationship given by equation (24) is applied to specifically charge the vanadium electrolytes in the VRFB to defined state-of-charge values during the absorbance measurements. The results of the consequent measurements conducted using this relationship are discussed in the following sections of chapter 3 [148].

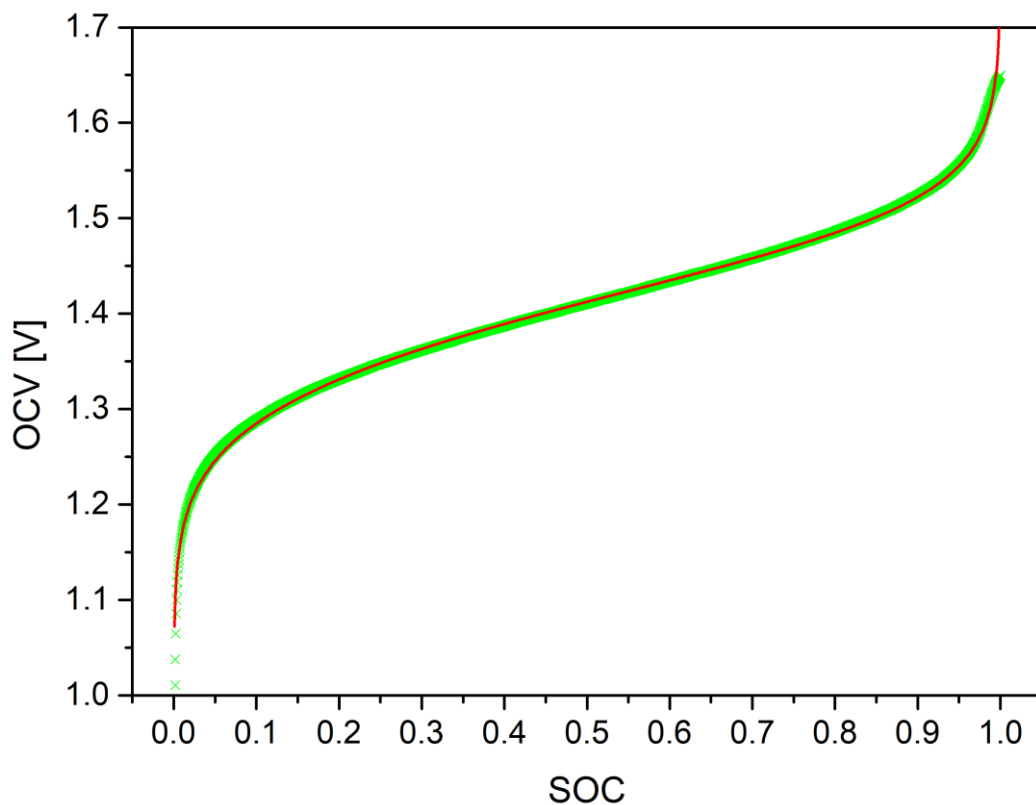


*Fig. 10. Experimental OCV values (green crosses) plotted versus SOC (determined by Coulomb counting) and fitted with equation (27) shown in red. The measurement uncertainties (and the related error bars) are smaller than the size of the green crosses [148].*

### 3.2.2 SOC determination for the negative half-cell of the VRFB

In the negative half-cell electrolyte (anolyte) several UV/Vis/NIR spectra are recorded in-situ during the VRFB charging process. The observed absorbance maxima of the contained  $V^{2+}$  and  $V^{3+}$  species are attributed to d–d transitions and exhibit relatively low intensities [84]. The experimental results of the spectrometric investigations are presented in Figure 11.

Due to the execution of all measurements with VRFB electrolytes in the balanced state the OCV cell related overall SOC is equal to the negative partial state-of-charge  $SOC_{2/3}$  [148]. In-situ UV/Vis/NIR spectra are plotted as a function of both increasing and decreasing negative partial state-of-charge  $SOC_{2/3}$  in three-dimensional representations.

At  $SOC_{2/3} = 0.0$  according to the OCV cell voltage, two absorbance maxima are observed for the  $V^{3+}$  species at the wavelengths 400 nm and 600 nm. At this state-of-charge value almost no  $V^{2+}$  species are present in the anolyte. With increasing state-of-charge a continuous absorbance decrease of the two peaks is registered [148].

This decrease in intensity is noticeably more pronounced for the  $V^{3+}$  absorbance band at 400 nm. Simultaneously, a  $V^{2+}$  absorbance peak at 570 nm is evolving together with an additional low-intensity maximum of the  $V^{2+}$  species at 850 nm with continuously increasing absorbance. As displayed in Figure 11, the  $V^{2+}$  peak located at 570 nm overlaps with the  $V^{3+}$  peak at 600 nm.

At  $SOC_{2/3} = 0.8$  according to the OCV cell voltage, the  $V^{3+}$  absorbance bands are significantly reduced in comparison with  $SOC_{2/3} = 0.0$ . Due to the VRFB charging operation the  $V^{3+}$  species are steadily electrochemically reduced to the corresponding  $V^{2+}$  species [148].

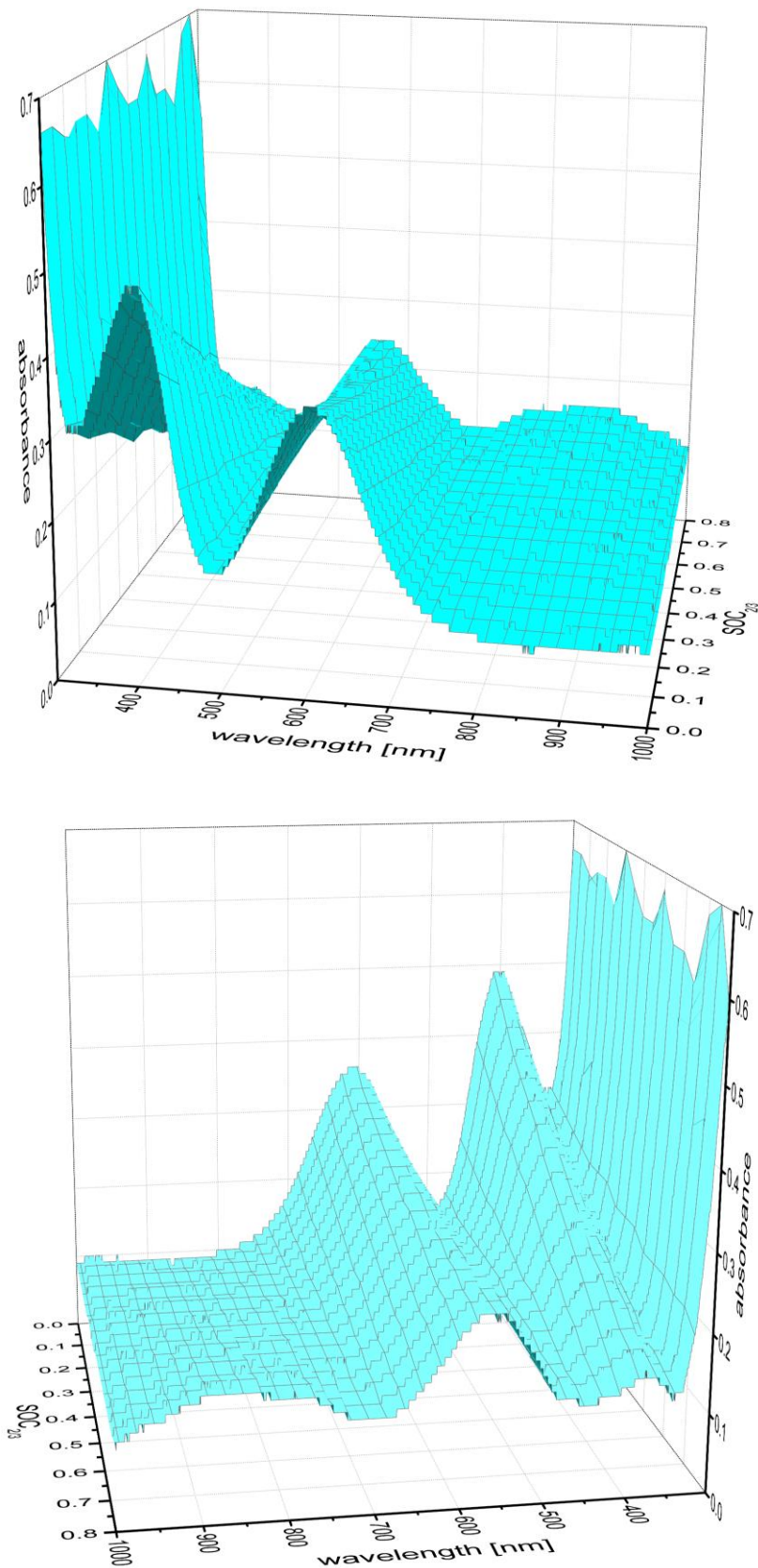


Fig. 11. Negative half-cell electrolyte (anolyte): In-situ UV/Vis/NIR spectral data as a function of increasing SOC<sub>2/3</sub> (above) [148] and of decreasing SOC<sub>2/3</sub> (below).

Because of the stronger absorbance signal at low states-of-charge in combination with a more pronounced decrease in signal intensity with increasing state-of-charge the  $V^{3+}$  absorbance maximum at 400 nm is applied for the photometric determination of the state-of-charge of the negative half-cell electrolyte (anolyte) [148]. As illustrated in Figure 12, the measured absorbance values (abs) at 400 nm exhibit a linear dependence on the negative half-cell state-of-charge  $SOC_{2/3}$  according to equation (28):

$$SOC_{2/3}(abs) = 1.10 - 2.33 * abs (@ 400 nm) \quad (28)$$

Consequently, the previously introduced procedure describes a calibration of the photometric measured absorbance values of the anolyte to the related OCV data (which correspond to a comparison between the anolyte and catholyte, as detailed in Eq. 24) [148]. All underlying spectrometric experiments are conducted in a pristine VRFB and therefore with vanadium electrolytes in the fully balanced state. As explained within the derivation of the Nernst based fit equation (see chapter 3.2.1), if the VRFB electrolytes are in this balanced state the two half-cell specific partial states-of-charge are equal to the overall state-of-charge of the VRFB and thus:  $SOC_{2/3} = SOC_{4/5} = SOC$  [148]. Henceforth, this introduced procedure based on the photometry of the anolyte is applicable for the determination of the negative partial  $SOC_{2/3}$  of a VRFB in various states. Accordingly, even if the two partial states-of-charge  $SOC_{2/3}$  and  $SOC_{4/5}$  have different magnitudes commonly classified as an imbalanced state [148].

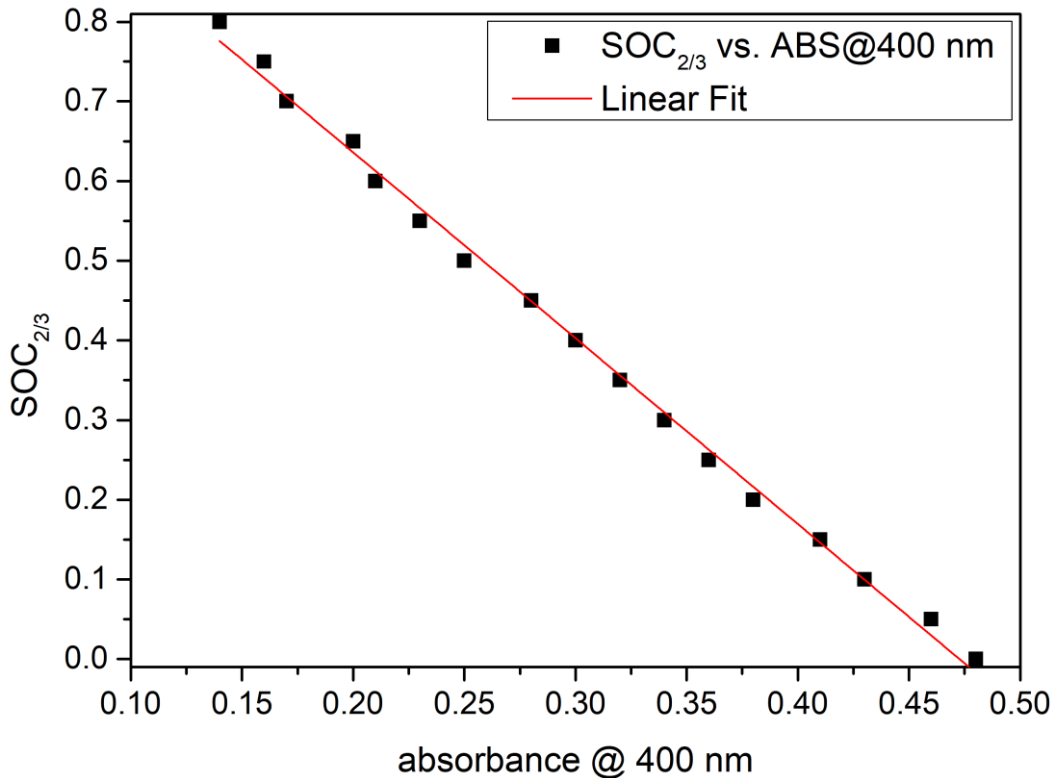


Fig. 12. Negative half-cell electrolyte (anolyte): Linear fit of the measured absorbance values at 400 nm as a function of the negative partial  $SOC_{2/3}$  (according to the OCV cell voltage). The measurement uncertainties (error bars) are smaller than the size of the black dots [148].

Besides, the low-intensity maximum of the  $V^{2+}$  species at 850 nm with continuously increasing absorbance during charging of the VRFB is also potentially suitable for monitoring the negative partial  $SOC_{2/3}$ . Due to its very low intensity the used spectrometer set-up is unable to detect the absorbance changes caused by a charging of the electrolyte in a single 0.05 SOC step. Contrarily, the absorbance changes induced by a 0.10 SOC charging step are mostly registered (see Figure 13).

However, a trend of a linear dependence between the absorbance at 850 nm and the negative partial  $SOC_{2/3}$  can be recognized. To achieve a higher sensitivity towards these slight absorbance changes the flow-through cuvette's optical path length can be increased from 200  $\mu\text{m}$  to approximately 1 mm. Thus, the intensity of the  $V^{2+}$  absorption maximum will likely be situated in the required absorbance range for the monitoring of the negative partial  $SOC_{2/3}$ .

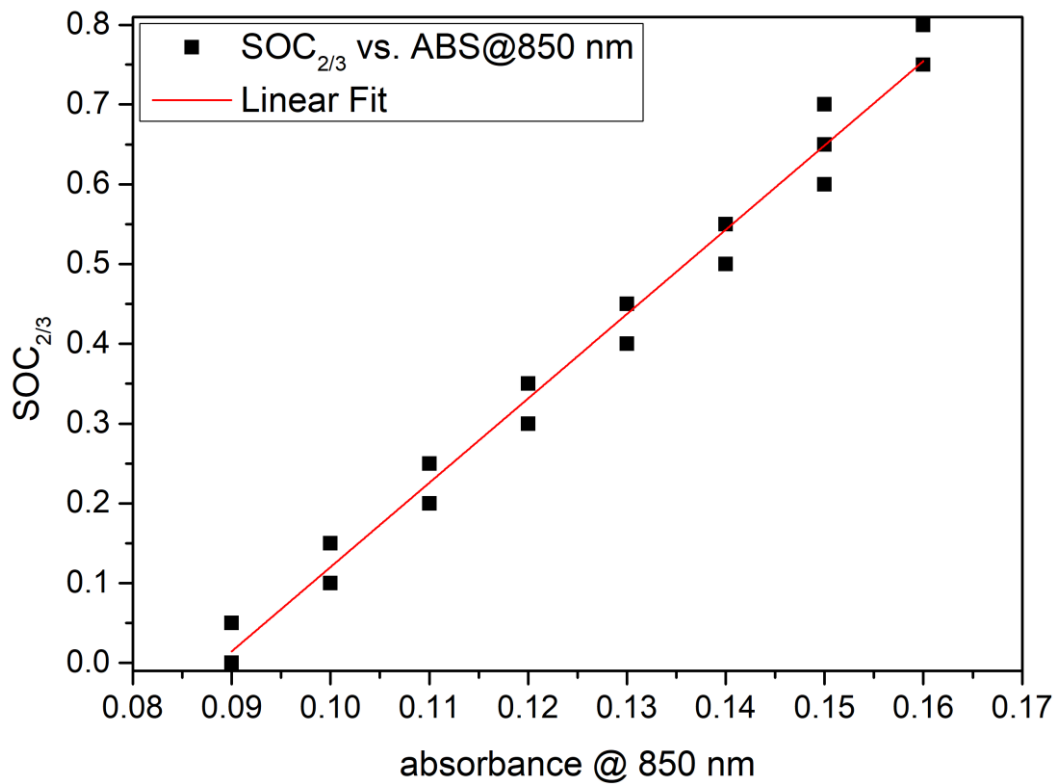


Fig. 13. Negative half-cell electrolyte (anolyte): Trend of the measured absorbance values at 850 nm as a function of the negative partial  $SOC_{2/3}$  (according to the OCV cell voltage). The measurement uncertainties are smaller than the size of the black dots.

### 3.2.3 SOC determination for the positive half-cell of the VRFB

Additionally, in the positive half-cell electrolyte (catholyte) several UV/Vis/NIR spectra are recorded in-situ during the VRFB charging process. All measurements are conducted with VRFB electrolytes in the balanced state. Thus, the OCV cell related overall SOC is equal to the positive partial state-of-charge  $SOC_{4/5}$ . The experimentally obtained absorbance results are plotted as a function of both increasing and decreasing positive partial state-of-charge  $SOC_{4/5}$  in form of two 3D line graphs illustrated in Figure 14 [148].

Beginning at  $SOC_{4/5} = 0.0$  according to the OCV cell voltage, a broad absorbance continuum is obtained for the  $V^{4+}$  species at a wavelength of 760 nm. At this state-of-charge value nearly no  $V^{5+}$  species are present in the catholyte. With rising  $SOC_{4/5}$  concerning the OCV cell voltage, the continuum absorbance is increasing, runs through a maximum at  $SOC_{4/5} \approx 0.3$  and decreases again, until  $SOC_{4/5} = 0.8$  where the charging operation is finished [148].

The observed maximum at  $SOC_{4/5} \approx 0.3$  is the sum of the absorbances of the  $VO^{2+}$  species and the additionally formed binuclear species with a  $V_2O_3^{3+}$  central ion [147,148]. Besides, the growth of two further local absorbance peaks at 570 nm and 680 nm is detected during the charging process of the VRFB. These local absorbance peaks combined with the exceptional position of the absorbance intensity maximum at  $SOC_{4/5} \approx 0.3$  indicate the formation of an intermediate mixed-valence complex between the existing  $V^{4+}$ -ions and the newly formed  $V^{5+}$ -ions [147].

Furthermore, with the increase of  $SOC_{4/5}$  a steeply rising  $V^{5+}$  absorbance flank within the wavelength range between 400 nm and 500 nm is obtained [148]. This intense  $V^{5+}$  absorbance flank is caused by an increasing concentration of  $V^{5+}$  species during the charging process. Consequently, a rising number of  $V^{5+}$  charge transfer transitions is detected [148].

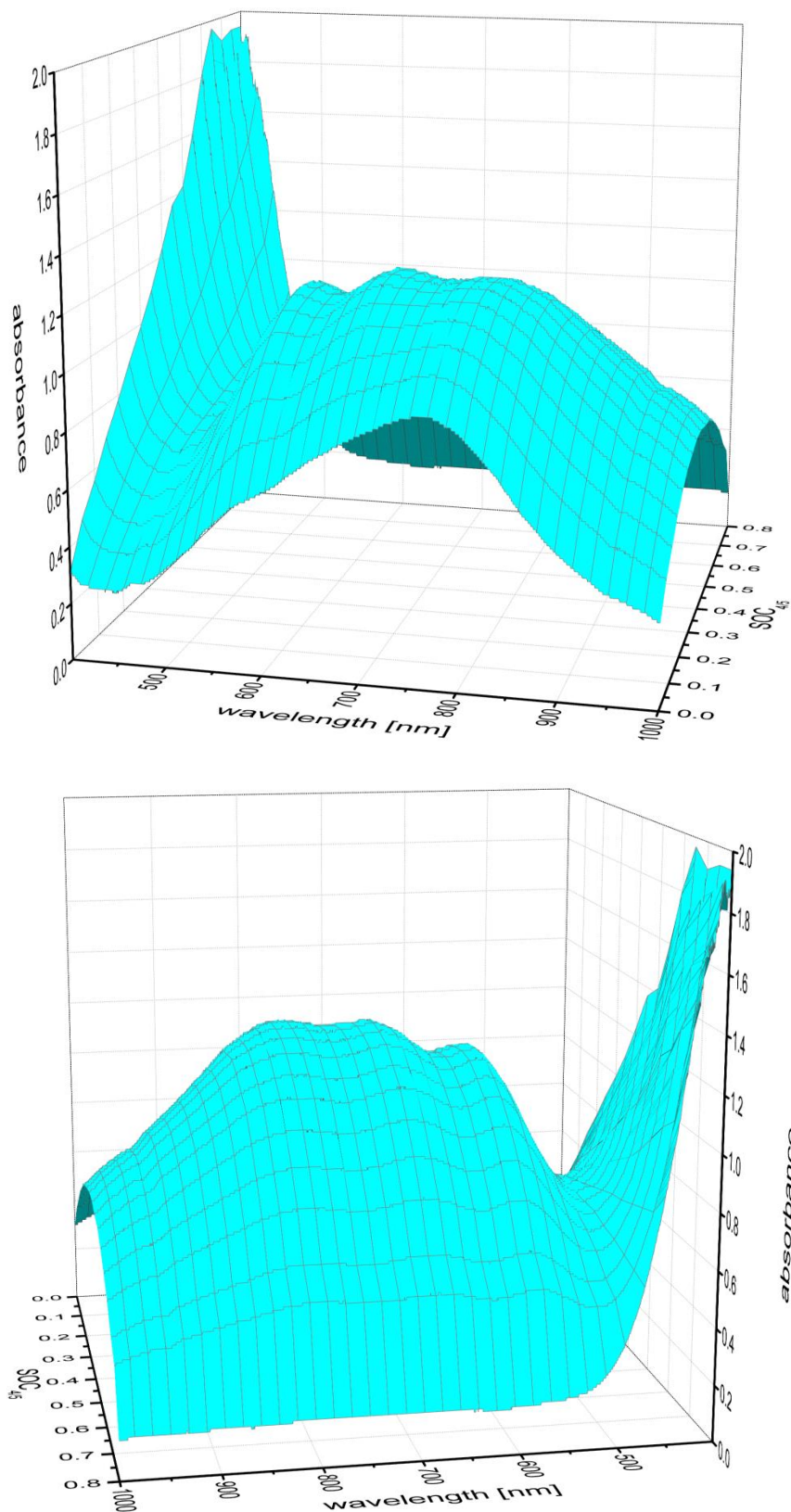


Fig. 14. Positive half-cell electrolyte (catholyte): In-situ UV/Vis/NIR spectral data as a function of increasing SOC<sub>4/5</sub> (above) [148] and of decreasing SOC<sub>4/5</sub> (below).

The related steady increase of the  $V^{5+}$  absorbance flank enables its photometric evaluation. Thus, a wavelength of 440 nm is used for the photometric determination of the state-of-charge of the positive half-cell electrolyte (catholyte) [148]. These  $V^{5+}$  absorbance values at 440 nm are shown as a function of the positive partial  $SOC_{4/5}$  in Figure 15. Probably due to the intermediate formation and subsequent depletion of the mixed-valence complex during the VRFB charging process the increase of the  $V^{5+}$  absorbance values is not strictly linear [148]. Hence, the present evolution of the absorbance values is empirically described with a third order polynomial:

$$SOC_{4/5}(abs) = a + B1 * abs^1 + B2 * abs^2 + B3 * abs^3 \quad (29)$$

where  $a = 0.09$ ;  $B1 = -1.06$ ;  $B2 = 3.17$ ;  $B3 = -1.49$  and  $abs =$  absorbance at 440 nm.

Consequently, a calibration of the UV/Vis/NIR absorbance values at 440 nm to the OCV related  $SOC_{4/5}$  values is described. It is applicable for the photometric in-situ determination of the positive partial  $SOC_{4/5}$  in the VRFB's positive half-cell electrolyte (catholyte) within the range  $0 \leq SOC_{4/5} \leq 0.8$  [148]. Every absorbance measurement is conducted in a pristine VRFB electrolyte, also denoted as a VRFB electrolyte in the balanced state. Henceforth, the introduced approach based on the photometric analysis of the catholyte enables the determination of the positive partial  $SOC_{4/5}$  of a VRFB in various states. Thus, the detection of an imbalanced state of the VRFB catholyte is also possible [148].

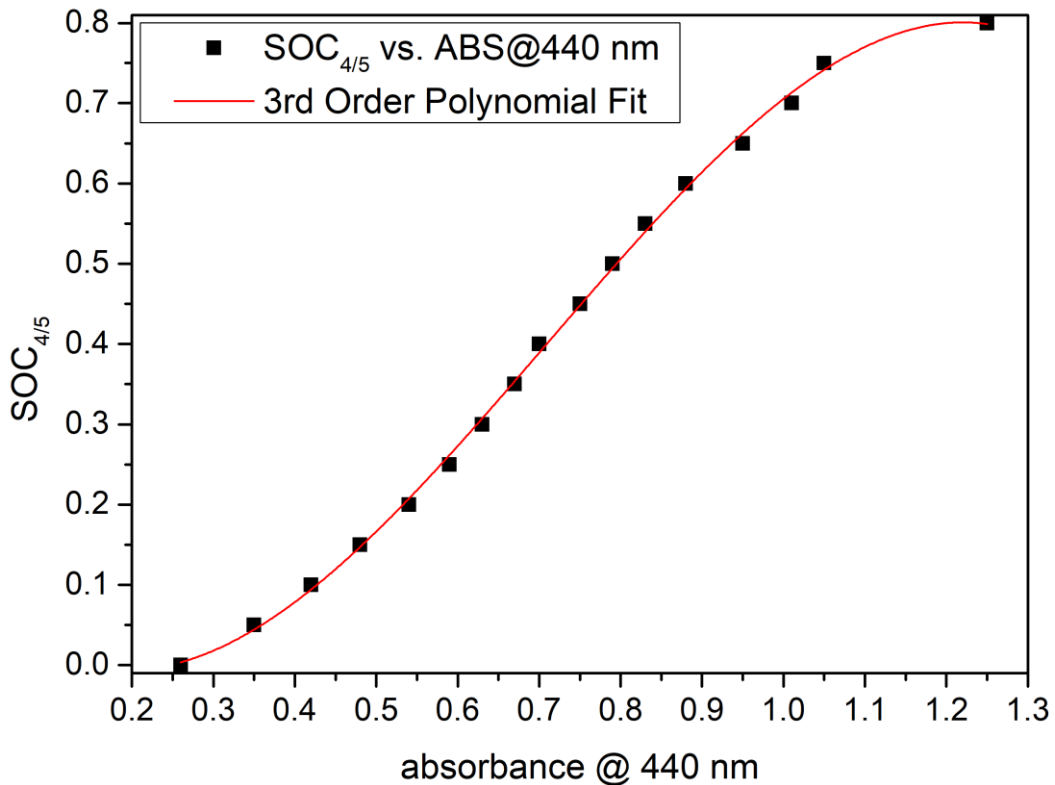


Fig. 15. Positive half-cell electrolyte (catholyte): Third order polynomial fit of the measured absorbance values at 440 nm depending on the positive partial  $SOC_{4/5}$  according to the OCV cell voltage. The measurement uncertainties (error bars) are smaller than the size of the black dots [148].

### 3.2.4 Conclusion

The previously introduced spectrometric state-of-charge sensor is particularly developed for in-situ applications to facilitate immediate and autonomous SOC monitoring. Besides, the sensor is applicable in the negative vanadium electrolyte (anolyte) as well as in the positive electrolyte (catholyte). With the described determination approach the separate half-cell specific analysis of the VRFB electrolytes is enabled. Therefore, both the negative and positive partial state-of-charge ( $SOC_{2/3}$  and  $SOC_{4/5}$ ) can be directly monitored.

Additionally, the various vanadium species in the electrolyte exhibit characteristic colors which differ depending on their vanadium oxidation state. Due to the applied UV/Vis/NIR sensing technique the introduced approach is able to distinguish between the different vanadium oxidation states. Thus, the concentrations of the differently oxidized vanadium species can be directly determined. This additional information provides significantly deeper insights in the vanadium electrolyte's chemical composition and its alterations during charge-discharge cycling of the VRFB.

Furthermore, the use of a resistant quartz flow-through cell/cuvette protects the hardware of the sensor set-up against the aggressive vanadium electrolyte and ensures very good optical conductivity. In case of the application in large VRFB storage units the potential clogging of the flow-through cell can be prevented by means of increased optical path lengths (see chapter 3.2.2) and/or by installing of appropriate filters. Hence, the cuvette's long-term applicability in the electrolyte circuit allows for longer maintenance intervals and consequently extended operation times of the current SOC sensor.

## 4. Potentiometric titration coupled in-situ spectroscopy

Due to the strong absorbances of the vanadium species in concentrated solution the determination of the related absorption coefficients with UV/Vis/NIR spectrometry is difficult. A special challenge is the access to the absorption coefficient of the oxygen-sensitive  $V^{2+}$  species. Accordingly, low vanadium concentrations are normally examined [152]. Therefore, an approach combining potentiometric titration with UV/Vis/NIR spectroscopy is presented in the following which enables the analysis of vanadium concentrations up to  $1.6 \text{ mol L}^{-1}$  under inert gas atmosphere. Henceforth, the resulting absorption coefficients can be applied for in-operando photometric SOC monitoring in VRFB systems [153].

### 4.1 Experimental

#### 4.1.1 Electrolyte

The starting material for the preparation of the investigated samples is a commercial, fresh vanadium electrolyte. It consists of a 50:50% mole fraction of  $V^{3+}$  and  $V^{4+}$ , a total vanadium concentration of  $1.6 \text{ mol L}^{-1}$  and is produced by GfE (Gesellschaft für Elektrometallurgie mbH, Germany). Additionally, the applied vanadium electrolyte contains  $2.0 \text{ mol L}^{-1}$  of sulfuric acid according to the manufacturer [153].

Further  $2 \text{ mol L}^{-1}$  sulfate ions originate from the previous dissolution of vanadium sulfates in the  $2.0 \text{ mol L}^{-1}$  sulfuric acid during the electrolyte production. Thus, the resulting total sulfate concentration is  $4 \text{ mol L}^{-1}$ . Besides, the used vanadium electrolyte includes  $0.05 \text{ mol L}^{-1}$  of phosphoric acid [153].

For the adjustment of a vanadium oxidation state of  $V^{2+}$ , the applied vanadium electrolyte is filled into a laboratory VRFB single cell which is introduced in chapter 3.1. In this VRFB single cell a combined pretreatment and charging procedure is taking place [153]. Initially, the negative half-cell electrolyte (anolyte) is purged with nitrogen gas of a purity of 99.99 vol. % for 3 min to remove dissolved oxygen gas. Then, the anolyte is covered with paraffin oil to exclude subsequent oxidation of the newly generated  $V^{2+}$ -species by atmospheric oxygen.

Afterwards, the vanadium electrolytes are fully charged. Thus, 99.9% of the vanadium cations in the anolyte are in the  $V^{2+}$  oxidation state, according to a determination of the open-circuit-voltage [148,153]. Simultaneously, the negative as well as the positive half-cell electrolyte (anolyte and catholyte respectively) is continuously agitated by means of a magnetic stirrer to ensure homogeneity within each electrolyte vessel. Accordingly, with the anolyte a  $1.6 \text{ mol L}^{-1}$   $V^{2+}$  stock solution is obtained [153].

Additional solutions for the lower concentrated samples are prepared by dilution of this  $1.6 \text{ mol L}^{-1}$   $V^{2+}$  stock solution with a  $2.0 \text{ mol L}^{-1}$  sulfuric acid standard solution (AppliChem GmbH, Germany) using 20 mL volumetric flasks [153].

Thus, the starting points for the potentiometric titrations are the  $V^{2+}$  electrolytes in different vanadium concentrations originated from the fully charged VRFB analyte [153].

Prior to every titration start a  $V^{2+}$  sample of 15 mL is pipetted in the titration vessel. During the sample transfer a small part of its  $V^{2+}$  content is oxidized to  $V^{3+}$  by atmospheric oxygen. However, this small sample part is subsequently determined by means of an extrapolation procedure as explained below [153].

#### 4.1.2 Spectroscopic coupled potentiometric titration set-up

The experimental titration set-up (see Figure 16) consists of a conically shaped titration vessel equipped with a magnetic stirrer and sealed with a Teflon cover. The crucial advantage of the conical titration vessel is the low minimal required sample volume (analyte volume) of 15 mL. Due to the low required sample volume the corresponding necessary amount of titrant solution is also comparatively low [153].

Besides, the applied Teflon cover provides five drill holes to include the following components into the titration set-up: a UV/Vis/NIR immersion probe (Hellma Excalibur, Hellma GmbH & Co. KG, Germany, path length: 1 mm), a titration tube for the continuous dosage of the oxidizing agent solution ( $0.2 \text{ mol L}^{-1} \text{ KMnO}_4$ , Bernd Kraft GmbH, Germany), a combination electrode (working electrode: Au, reference electrode: Ag/AgCl/ $3 \text{ mol L}^{-1} \text{ KCl}$ , Metrohm AG, Switzerland), a nitrogen gas supply and a separate gas outlet [153].

The titer of the  $\text{KMnO}_4$  titrant is previously determined by manual titration of an accurately weighed amount of sodium oxalate dissolved in 56 mL  $0.2 \text{ mol L}^{-1} \text{ H}_2\text{SO}_4$ . Therefore, the titer determination is conducted at  $80 \text{ }^\circ\text{C}$  in stirred solution using a burette. Humidified nitrogen gas is utilized to prevent oxidation of the  $V^{2+}$ -species and water loss during the titration process [153].

The optical UV/Vis/NIR immersion probe is directly connected to the UV/Vis/NIR spectrometer (TIDAS 100, J&M Analytik AG, Germany) by means of SMA 905 plugs [153]. Before beginning with the absorbance (abs) measurements the two light sources of the UV/Vis/NIR spectrometer are permitted to warm up for 90 min to reach a stationary thermal state.

The control of the spectroscopic UV/Vis/NIR set-up is realized with the software Tidas DAQ (J&M Analytik AG, Germany). In this software the integration time for the recorded absorbance spectra is adjusted to 90 ms. Each finally obtained absorbance spectrum results from the averaging of 16 previously recorded scans [153].

Additionally, the titration tube as well as the combination electrode is connected to the titrator (Metrohm 800 Dosino, Metrohm AG, Switzerland). The operation of the potentiometric titration set-up is performed with the software tiamo 2.4 (Metrohm AG, Switzerland). A sample volume (analyte volume) of 15 mL is chosen. The total vanadium concentrations of the samples are situated in the range of  $0.2 \text{ mol L}^{-1}$  to  $1.6 \text{ mol L}^{-1}$ . All samples are titrated with a  $0.2 \text{ mol L}^{-1} \text{ KMnO}_4$  solution [153].

Both the potential measurements and the in-situ UV/Vis/NIR spectroscopy are conducted after every dosing step of the titration. In case of the potential measurements a variable delay time up to 180 s is selected depending on the required potential adjustment time. Subsequent to each potential measurement a UV/Vis/NIR spectrum is taken. Every dataset consists of 100 titration steps with an equivalent number of added volumes of the  $0.2 \text{ mol L}^{-1}$   $\text{KMnO}_4$  titrant solution [153].

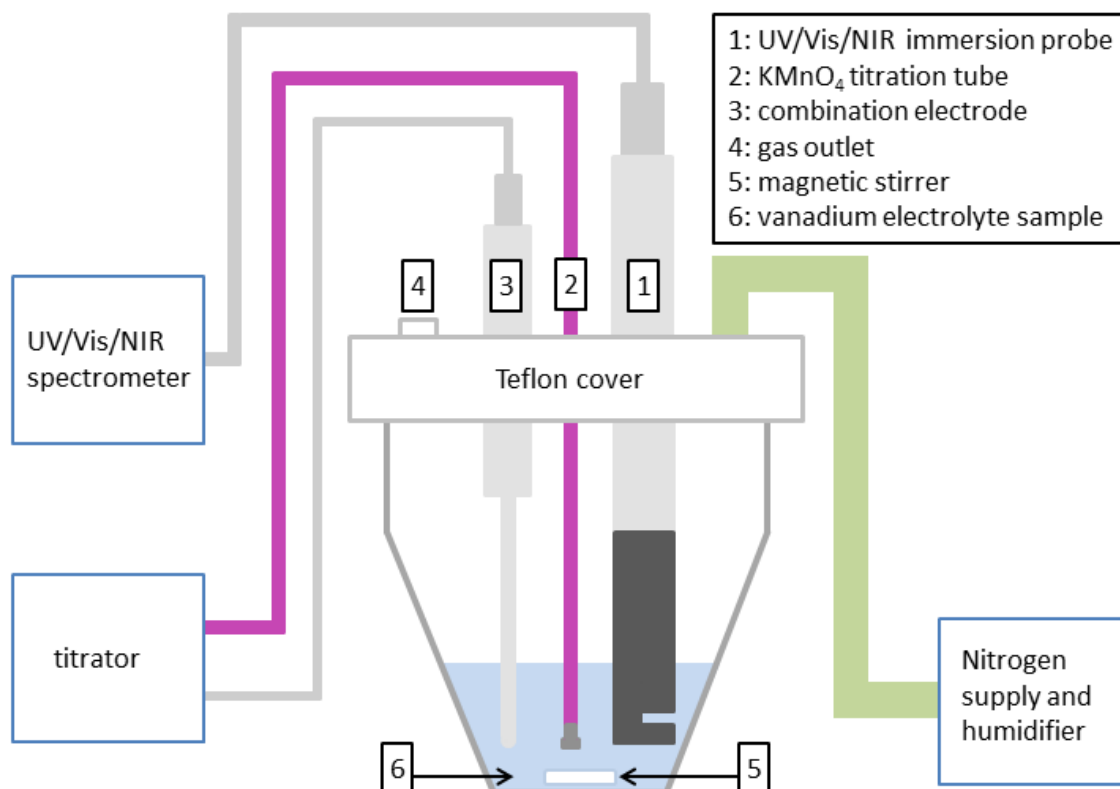


Fig. 16. Scheme for the spectroscopic-coupled potentiometric titration set-up.

## 4.2 Results and discussion

### 4.2.1 Potential measurements during the titration

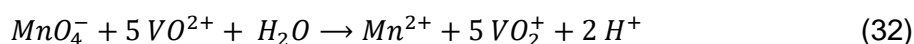
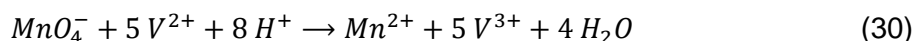
The ex-situ measurement method potentiometric titration yields absolute, oxidation state-specific vanadium concentrations. For the determination of the vanadium content several titrants can be applied, like cerium sulfate [154,155], potassium dichromate [156] and potassium permanganate [157,158]. A crucial challenge of the potentiometric titration is the continuous dilution of the sample during the stepwise addition of the titrant [153]. Thus, in order to minimize this dilution effect  $\text{KMnO}_4$  is employed as titrant (Permanganometry).

The complete reduction of the permanganate ion  $\text{MnO}_4^-$  ( $\text{Mn}^{7+} \rightarrow \text{Mn}^{2+}$ ) is equal to 5 redox equivalents. Contrarily, the Cerimetry delivers only 1 redox equivalent ( $\text{Ce}^{4+} \rightarrow \text{Ce}^{3+}$ ). Besides, the reductions occurring in Dichrometry ( $\text{Cr}^{6+} \rightarrow \text{Cr}^{3+}$ ) correspond to 3 redox equivalents. Additionally, the  $\text{Mn}^{2+}$  species are colorless in this concentration range [153]. Thus, the intense color of surplus  $\text{MnO}_4^-$  allows the direct indication of an overtitration and consequently the determination of the end of the redox process.

During the potentiometric titration the vanadium content of the sample is entirely oxidized by means of the  $\text{KMnO}_4$  titrant solution. The totally dispensed volume of  $\text{KMnO}_4$  titrant solution is proportional to the  $\text{V}^{2+}$  concentration in the sample solution. Initially, all contained  $\text{V}^{2+}$  ions are oxidized to  $\text{V}^{3+}$ . Afterwards,  $\text{V}^{3+}$  is completely oxidized to  $\text{V}^{4+}$  and finally to  $\text{V}^{5+}$  [153].

In the Figures 17-20 the electrochemical potential is plotted as a function of the added volume of the  $0.2 \text{ mol L}^{-1}$   $\text{KMnO}_4$  titrant solution for an initial total vanadium concentration in the range of  $0.2 \text{ mol L}^{-1}$  to  $1.6 \text{ mol L}^{-1}$  [153]. The obtained potential steps deviate from the expected standard behavior due to the non-standard conditions in the sample solution, the formation of mixed potentials, the existence of additional redox pairs ( $\text{Mn}^{2+}/\text{MnO}_4^-$ ) and the presence of phosphoric acid in the electrolyte sample [153,159].

The redox reactions between the differently oxidized vanadium ions and the permanganate ion  $\text{MnO}_4^-$  taking place during the titration process are written in the following:



In the first reaction step of the titration eight protons are consumed. In both other reaction steps two protons are formed respectively. However, these fluctuations in the proton concentration are negligible concerning the surplus of sulfuric acid [153].

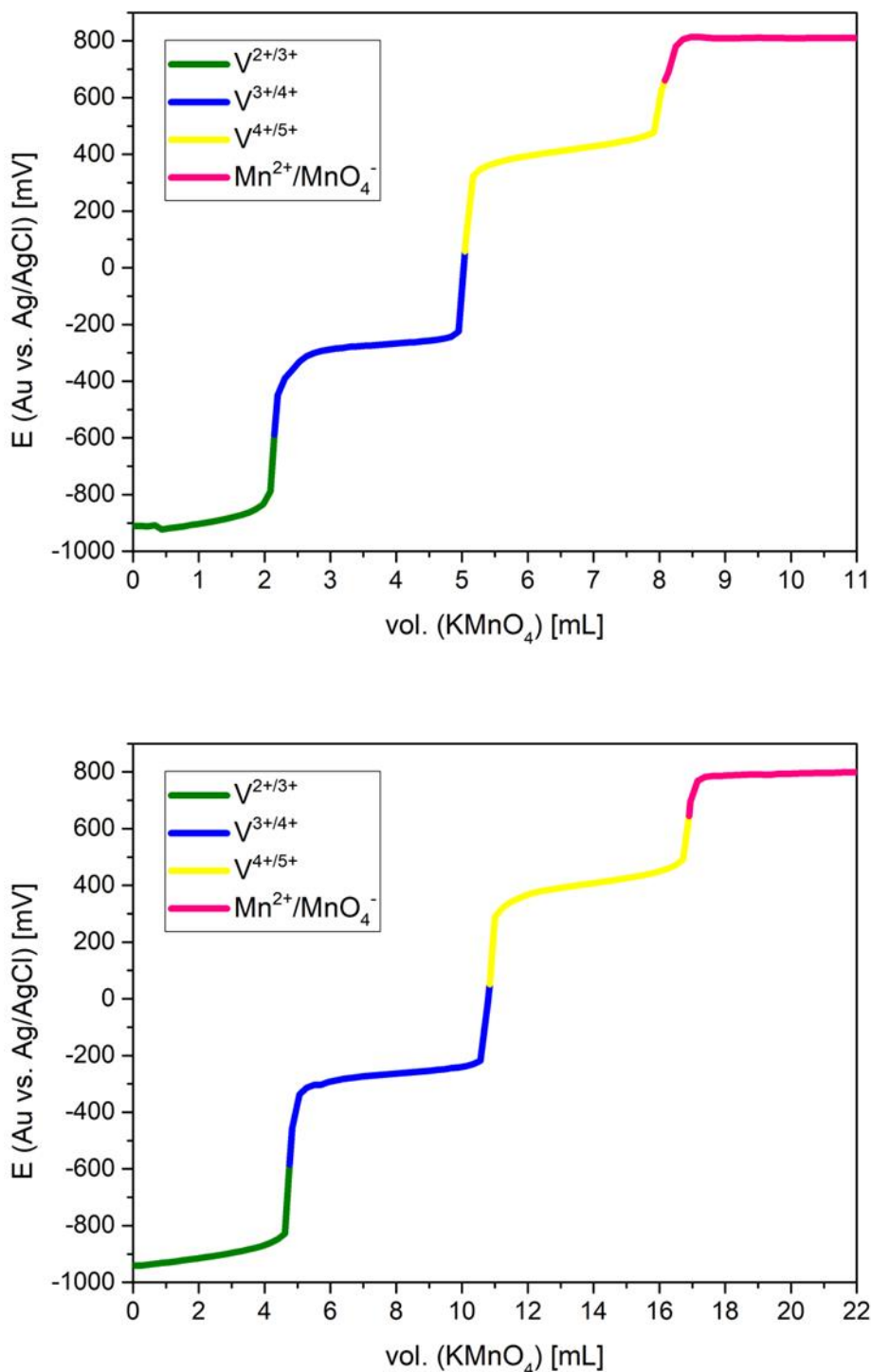


Fig. 17. Potentiometric titration of a vanadium sample solution with  $[V_{\text{total}}] = 0.2 \text{ mol L}^{-1}$  (above) and  $[V_{\text{total}}] = 0.4 \text{ mol L}^{-1}$  (below) using a  $0.2 \text{ mol L}^{-1}$   $\text{KMnO}_4$  titrant solution. At the starting point of the titration process a nominal  $\text{V}^{2+}$  sample solution with mainly  $\text{V}^{2+}$  and a small  $\text{V}^{3+}$  content is applied [153].

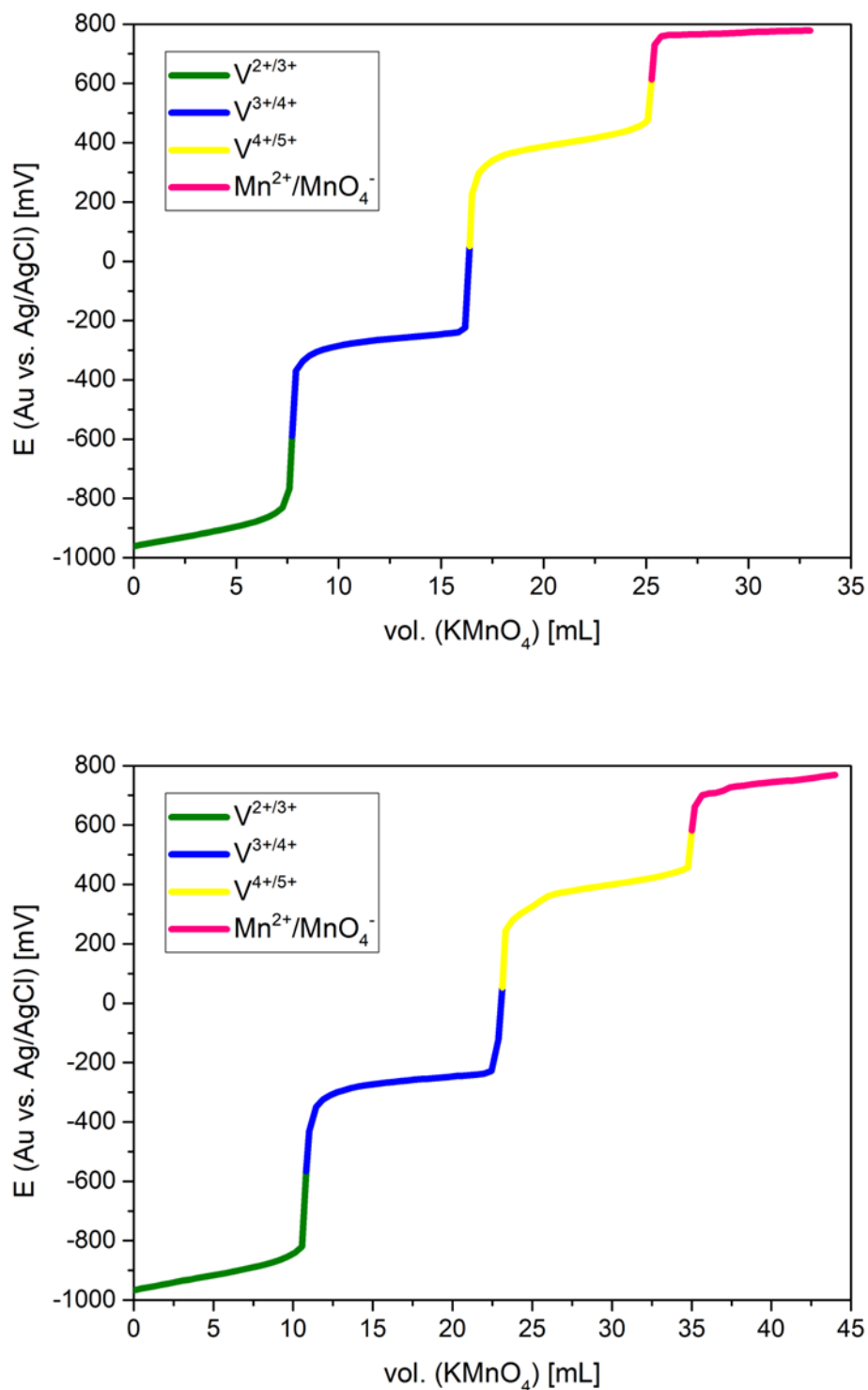


Fig. 18. Potentiometric titration of a vanadium sample solution with  $[V_{\text{total}}] = 0.6 \text{ mol L}^{-1}$  (above) and  $[V_{\text{total}}] = 0.8 \text{ mol L}^{-1}$  (below) using a  $0.2 \text{ mol L}^{-1}$   $\text{KMnO}_4$  titrant solution. At the starting point of the titration process a nominal  $\text{V}^{2+}$  sample solution with mainly  $\text{V}^{2+}$  and a small  $\text{V}^{3+}$  content is applied.

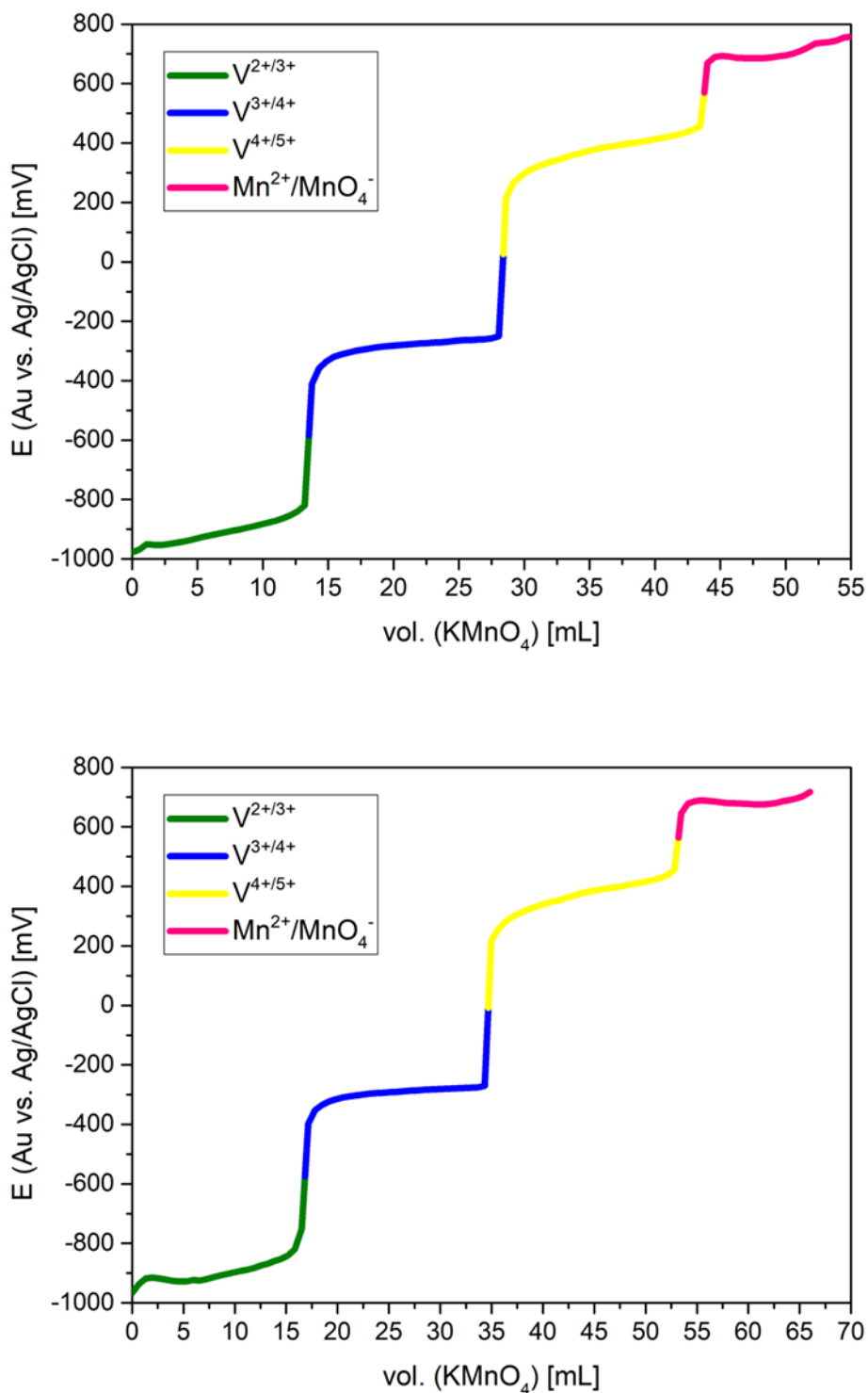


Fig. 19. Potentiometric titration of a vanadium sample solution with  $[V_{\text{total}}] = 1.0 \text{ mol L}^{-1}$  (above) and  $[V_{\text{total}}] = 1.2 \text{ mol L}^{-1}$  (below) using a  $0.2 \text{ mol L}^{-1}$   $\text{KMnO}_4$  titrant solution. At the starting point of the titration process a nominal  $\text{V}^{2+}$  sample solution with mainly  $\text{V}^{2+}$  and a small  $\text{V}^{3+}$  content is applied.

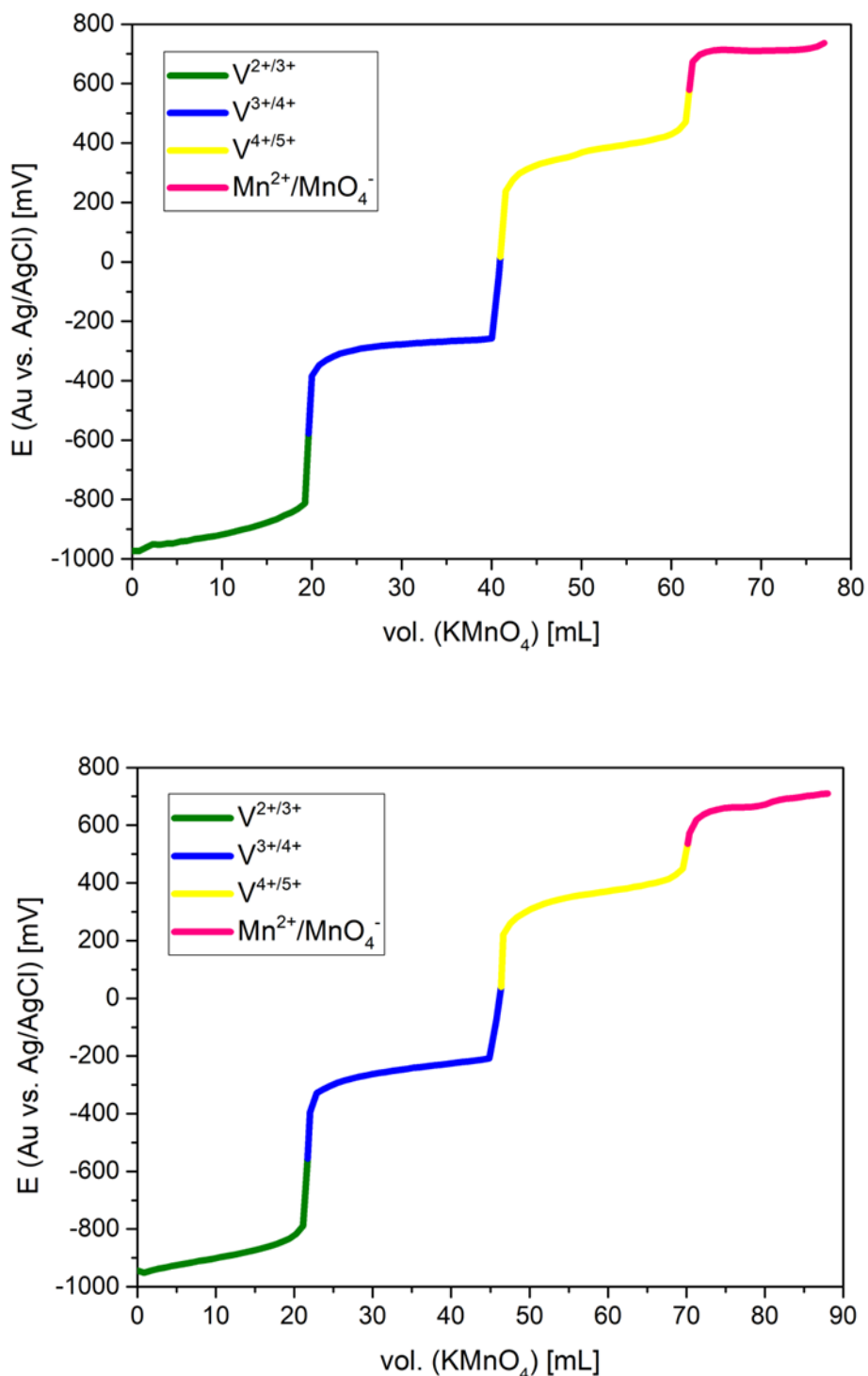


Fig. 20. Potentiometric titration of a vanadium sample solution with  $[V_{total}] = 1.4 \text{ mol L}^{-1}$  (above) and  $[V_{total}] = 1.6 \text{ mol L}^{-1}$  (below) using a  $0.2 \text{ mol L}^{-1}$   $\text{KMnO}_4$  titrant solution. At the starting point of the titration process a nominal  $\text{V}^{2+}$  sample solution with mainly  $\text{V}^{2+}$  and a small  $\text{V}^{3+}$  content is applied.

#### 4.2.2 Simultaneous in-situ UV/Vis/NIR spectroscopy

During the titration process the  $V^{2+}$  content of the initial sample solution is step by step oxidized to  $V^{5+}$ . Simultaneously, color changes as a result of the formation and subsequent depletion of the differently oxidized vanadium species can be observed. Thus, the proceeding step by step oxidation process is monitored by in-situ UV/Vis/NIR spectroscopy. In the Figures 21–23 the evolution of the UV/Vis/NIR spectral data during the complete oxidation of  $V^{2+}$  to  $V^{5+}$  for a total vanadium concentration of  $[V_{\text{total}}] = 1.6 \text{ mol L}^{-1}$  is illustrated [153].

The  $V^{2+}$  ion exhibits absorption maxima both at 570 nm and 850 nm (all absorption maxima positions are determined by manual reading). Besides, the  $V^{3+}$  absorption maxima are located at 400 nm and 600 nm, whereas the  $V^{4+}$  maximum ( $VO^{2+}$  species) is situated at 760 nm. The  $V^{2+}$  absorption band positioned at 570 nm overlaps with the  $V^{3+}$  absorption band located at 600 nm. Accordingly, these bands are not suitable for the photometric determination of the  $V^{2+}$  and  $V^{3+}$  concentrations [153].

The  $V^{5+}$  species  $VO_2^+$  exhibits a very intense absorption maximum at a wavelength of  $\lambda < 350$  nm. The corresponding peak intensity of this  $V^{5+}$  band is too high for the used UV/Vis/NIR spectroscopic set-up. The flank of the large  $V^{5+}$  band is situated within the range of  $350 \text{ nm} \leq \lambda \leq 500 \text{ nm}$  [153].

In Figure 21 the oxidation of  $V^{2+}$  to  $V^{3+}$ , which both show d-d-transitions, is spectroscopically observed. Due to the vanadium oxidation during the titration process, the two  $V^{2+}$  absorption bands at 570 nm and 850 nm are decreasing while the  $V^{3+}$  absorption bands at 400 nm and 600 nm show an intensity increase [153]. For the recorded spectra four isosbestic points (with constant absorbances within this titration step) are obtained at 330 nm, 470 nm, 620 nm and 690 nm.

At the titration start the sample contains already a detectable content of  $V^{3+}$  as proved by the small maximum at 400 nm in the first recorded (black) spectrum. Additionally, the  $V^{2+}$  spectrum exhibits a little shoulder at approximately 390 nm as published by Dobson et al. [153,160]. Consequently,  $V^{2+}$  also contributes slightly to the observed absorption maximum centered at 400 nm.

With further oxidation of the  $V^{3+}$  content to  $V^{4+}$  the absorption band of the  $V^{4+}$  species located at 760 nm increases as displayed in Figure 22. Simultaneously, the  $V^{3+}$  absorption maxima at 400 nm and 600 nm gradually decrease. The presence of only these two species and thus the exclusion of any other species is indicated by a single isosbestic point centered at 640 nm [153].

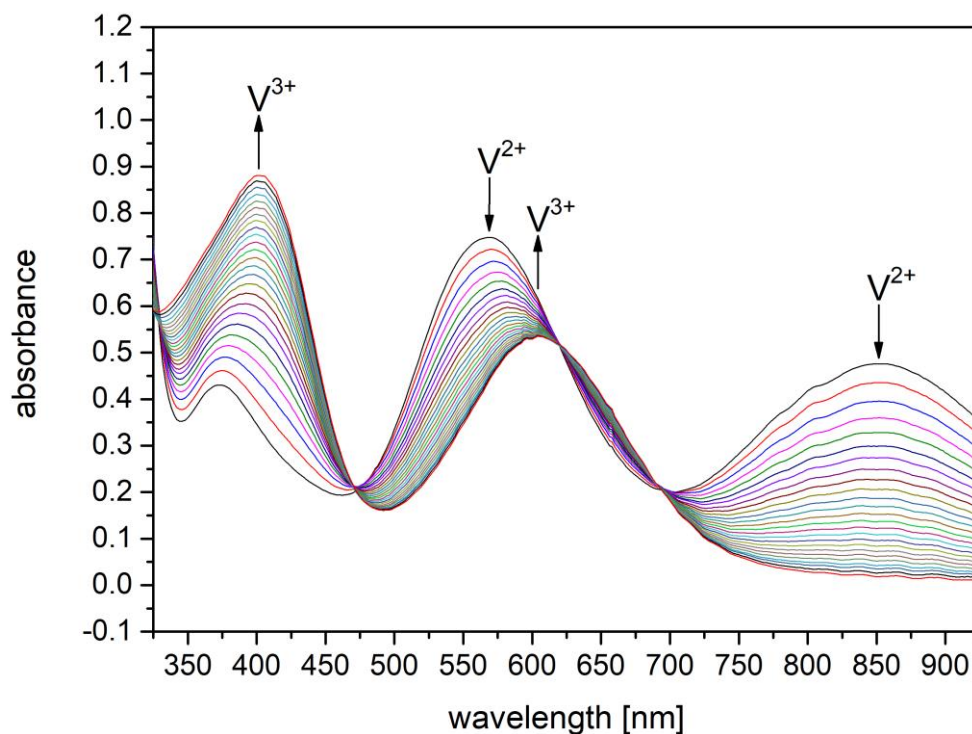


Fig. 21. Evolution of the UV/Vis/NIR spectral data during the oxidation of  $V^{2+}$  to  $V^{3+}$  for an initial total vanadium concentration  $[V_{total}] = 1.6 \text{ mol L}^{-1}$ . Four isosbestic points are situated at the wavelengths 330 nm, 470 nm, 620 nm and 690 nm [153].

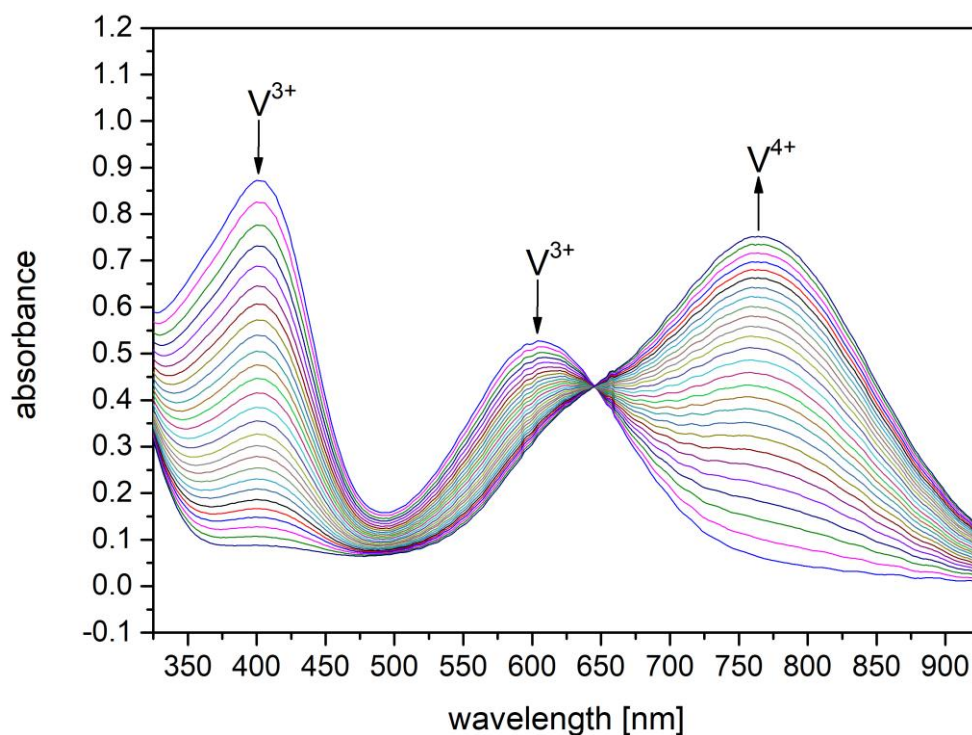


Fig. 22. Evolution of the UV/Vis/NIR spectral data during the oxidation of  $V^{3+}$  to  $V^{4+}$  for an initial total vanadium concentration  $[V_{total}] = 1.6 \text{ mol L}^{-1}$ . A single isosbestic point is located at 640 nm [153].

Further oxidation leads to an intensity decrease of the d-d-transition of the  $V^{4+}$  species at 760 nm (see Figure 23), whereas the  $V^{5+}$  charge-transfer-transition evolves at  $\lambda \leq 500$  nm with its absorption maximum outside of the UV/Vis/NIR spectrometer's measuring range [153]. Compared to the other two oxidation steps, no isosbestic point is detected for the vanadium sample (analyte) with the initial total vanadium concentration  $[V_{\text{total}}] = 1.6 \text{ mol L}^{-1}$ . Contrarily as displayed in Figure 24, at the relatively low initial total vanadium concentration  $[V_{\text{total}}] = 0.2 \text{ mol L}^{-1}$  a single isosbestic point appears to exist [153].

The presence of a binuclear  $V^{4+}-V^{5+}$  mixed-valence complex is mentioned in literature by Petchsingh et al. [138]. Additionally, the corresponding complex formation constant of  $K = 0.8 \text{ L mol}^{-1}$  at room temperature has already been determined [147]. Due to the continuous dilution of the initial vanadium sample solution during the titration process by the addition of the  $\text{KMnO}_4$  titrant solution, the immediate detection of a complex with such a low equilibrium constant is not possible with the current measurement set-up [153].

However, the absence of an isosbestic point at large initial total vanadium concentrations is a hint for the existence of an intermediate complex as described before. Contrarily, the related spectra for the  $0.2 \text{ mol L}^{-1}$  sample solution exhibit an isosbestic point as displayed in Figure 24. Due to the initially low total vanadium concentration combined with the following dilution of the sample solution the actual concentration of the mixed-valence complex is negligibly small and therefore undetectable [153].

The UV/Vis/NIR spectrometry of the titration process enables the identification and distinction of the various vanadium oxidation states in solution by means of the presence or absence of the species specific absorbance maxima. Thus, the in-situ UV/Vis/NIR monitoring of the vanadium oxidation process allows the quantitative determination of the different vanadium species in solution. Besides, a potentiometric titration by means of a  $\text{KMnO}_4$  titrant solution enables a direct, optical identification of an over-titration. The titrant's property to absorb also in the UV/Vis/NIR range facilitates the endpoint detection of the titration [153].

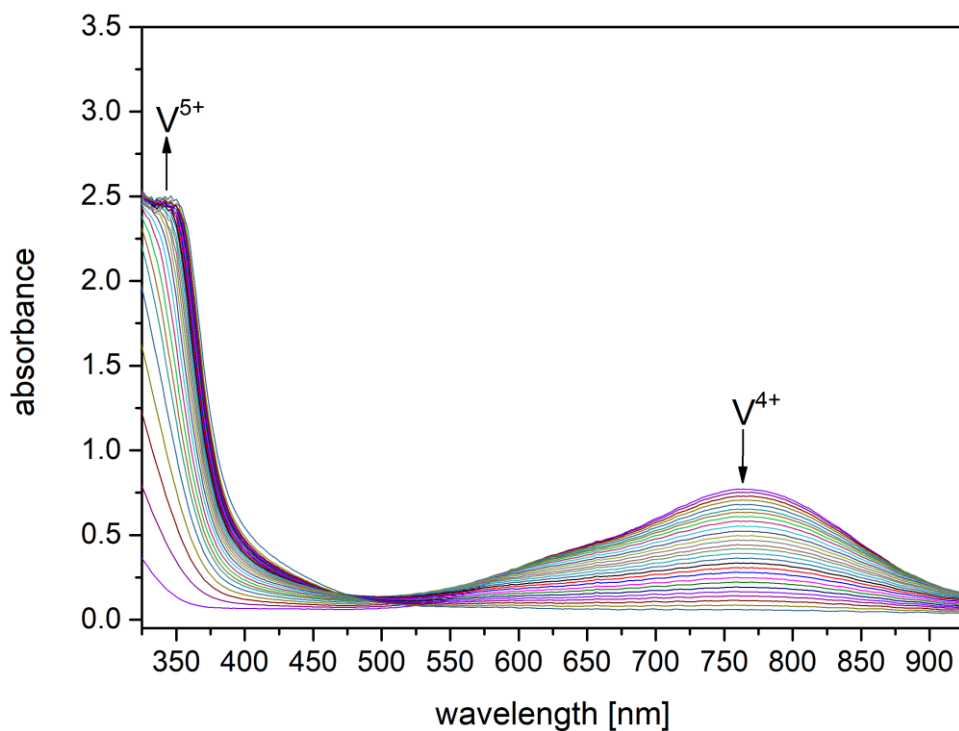


Fig. 23. Evolution of the UV/Vis/NIR spectral data during the oxidation of  $V^{4+}$  to  $V^{5+}$  for an initial total vanadium concentration  $[V_{total}] = 1.6 \text{ mol L}^{-1}$ . An isosbestic point does not occur [153].

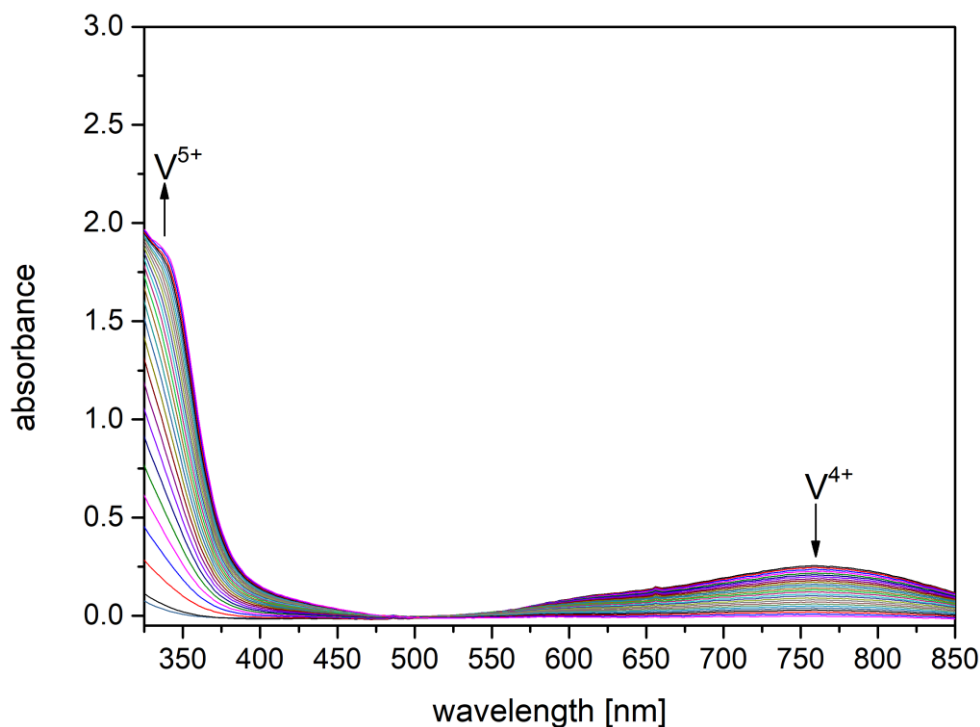


Fig. 24. Evolution of the UV/Vis/NIR spectral data during the oxidation of  $V^{4+}$  to  $V^{5+}$  for an initial total vanadium concentration  $[V_{total}] = 0.2 \text{ mol L}^{-1}$ . An isosbestic point seems to be existent [153].

In Fig. 25-32 the evolution of the UV/Vis/NIR spectral data during the entire oxidation of  $V^{2+}$  to  $V^{5+}$  in the titration is displayed for the initial total vanadium concentrations  $[V_{\text{total}}]$  in the range of  $0.2 \text{ mol L}^{-1}$  to  $1.6 \text{ mol L}^{-1}$ . For the first oxidation step of  $V^{2+}$  to  $V^{3+}$  the absorbance of the two differently oxidized vanadium ions generally increases while the initial total vanadium concentration  $[V_{\text{total}}]$  is increased. Besides, with rising  $[V_{\text{total}}]$  the  $V^{2+}$  absorption maxima increase noticeably faster in relation to the  $V^{3+}$  absorption maxima. This phenomenon is particular apparent for the  $V^{2+}$  absorption maxima at 570 nm and the  $V^{3+}$  maxima at 600 nm.

In the oxidation process  $V^{3+}$  is formed after  $V^{2+}$ . During the oxidation the sample is continuously diluted due to the successively added  $0.2 \text{ mol L}^{-1}$   $\text{KMnO}_4$  titrant solution. Accordingly, the  $V^{3+}$  absorption maxima are more influenced (decreased) by the dilution effect than the  $V^{2+}$  absorption maxima. The addition of the  $0.2 \text{ mol L}^{-1}$   $\text{KMnO}_4$  titrant solution and consequently the dilution effect are proportional to the sample's initial total vanadium concentration  $[V_{\text{total}}]$ . Hence, the noticeably slower increase of the  $V^{3+}$  absorption maxima is the result of the stronger dilution of  $V^{3+}$  during the titration process (compared to  $V^{2+}$ ) combined with the strengthening dilution effect with increasing  $[V_{\text{total}}]$ .

The same behavior is observed for the second oxidation step of  $V^{3+}$  to  $V^{4+}$ . Generally, both absorption maxima are increasing with rising  $[V_{\text{total}}]$ . The  $V^{4+}$  ion is formed after the  $V^{3+}$  ion. Accordingly, for the second oxidation step the  $V^{4+}$  absorption maxima at 760 nm are more affected by the dilution effect and thus increase significantly slower compared to the  $V^{3+}$  maxima at 400 nm. In absence of strong dilution the  $V^{4+}$  absorption maxima are noticeably more pronounced than the  $V^{3+}$  absorption maxima (see Fig. 25). Due to the strengthening dilution effect with increasing initial total vanadium concentration  $[V_{\text{total}}]$  the  $V^{3+}$  absorption maximum is larger than the  $V^{4+}$  maximum at  $[V_{\text{total}}] = 1.0 \text{ mol L}^{-1}$  or above.

Contrarily to the first two oxidation steps, in the third oxidation step of  $V^{4+}$  to  $V^{5+}$  the  $V^{5+}$  species yield only absorption flanks and no absorption maxima, because their intense charge-transfer-transitions are outside of the used spectrometer's range. Thus, no proportionality of the  $V^{5+}$  absorption to  $[V_{\text{total}}]$  is obtained. However, the  $V^{4+}$  absorption maxima are increased with rising  $[V_{\text{total}}]$ .

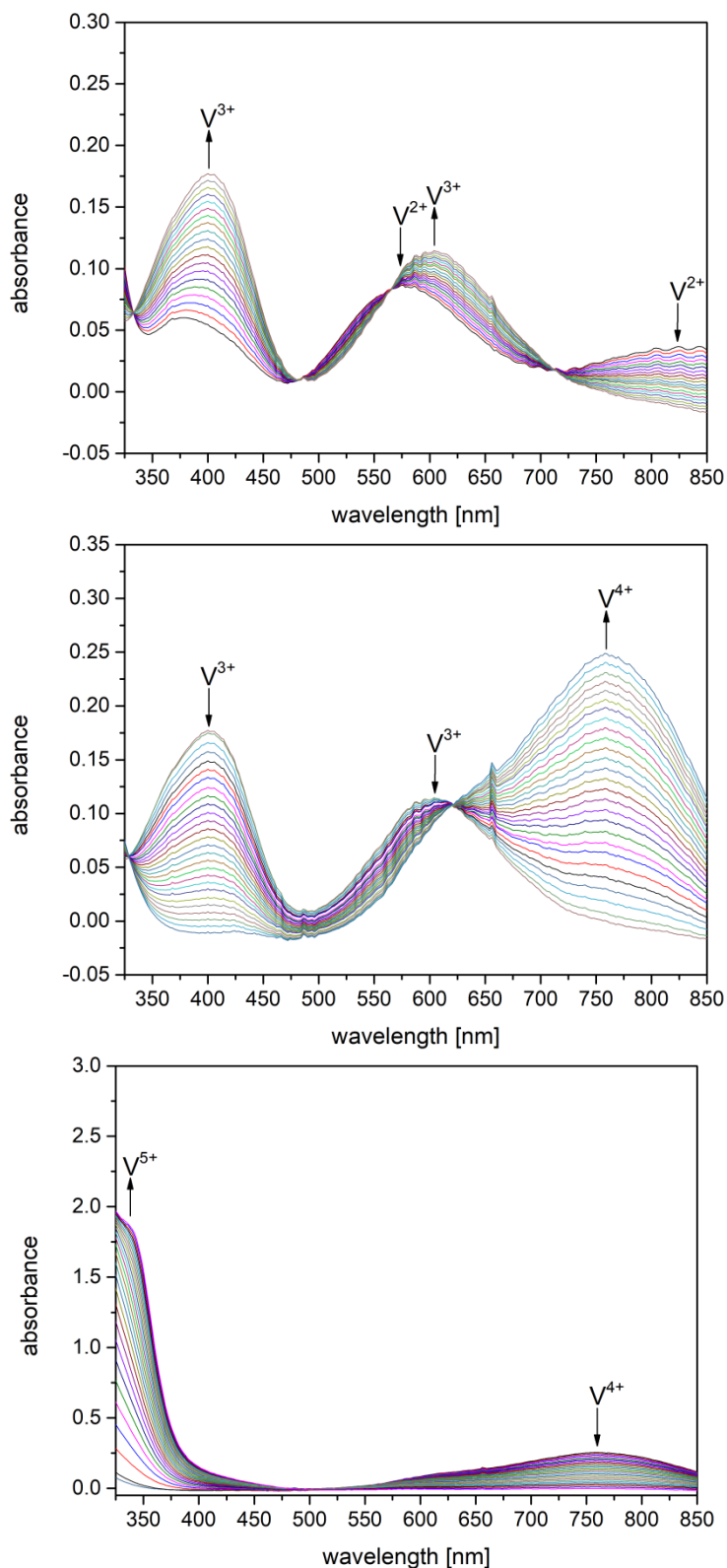


Fig. 25. Evolution of the UV/Vis/NIR spectral data during the oxidation of  $V^{2+}$  to  $V^{3+}$  (top),  $V^{3+}$  to  $V^{4+}$  (center) and  $V^{4+}$  to  $V^{5+}$  (bottom) for the initial total vanadium concentration  $[V_{total}] = 0.2 \text{ mol L}^{-1}$ .

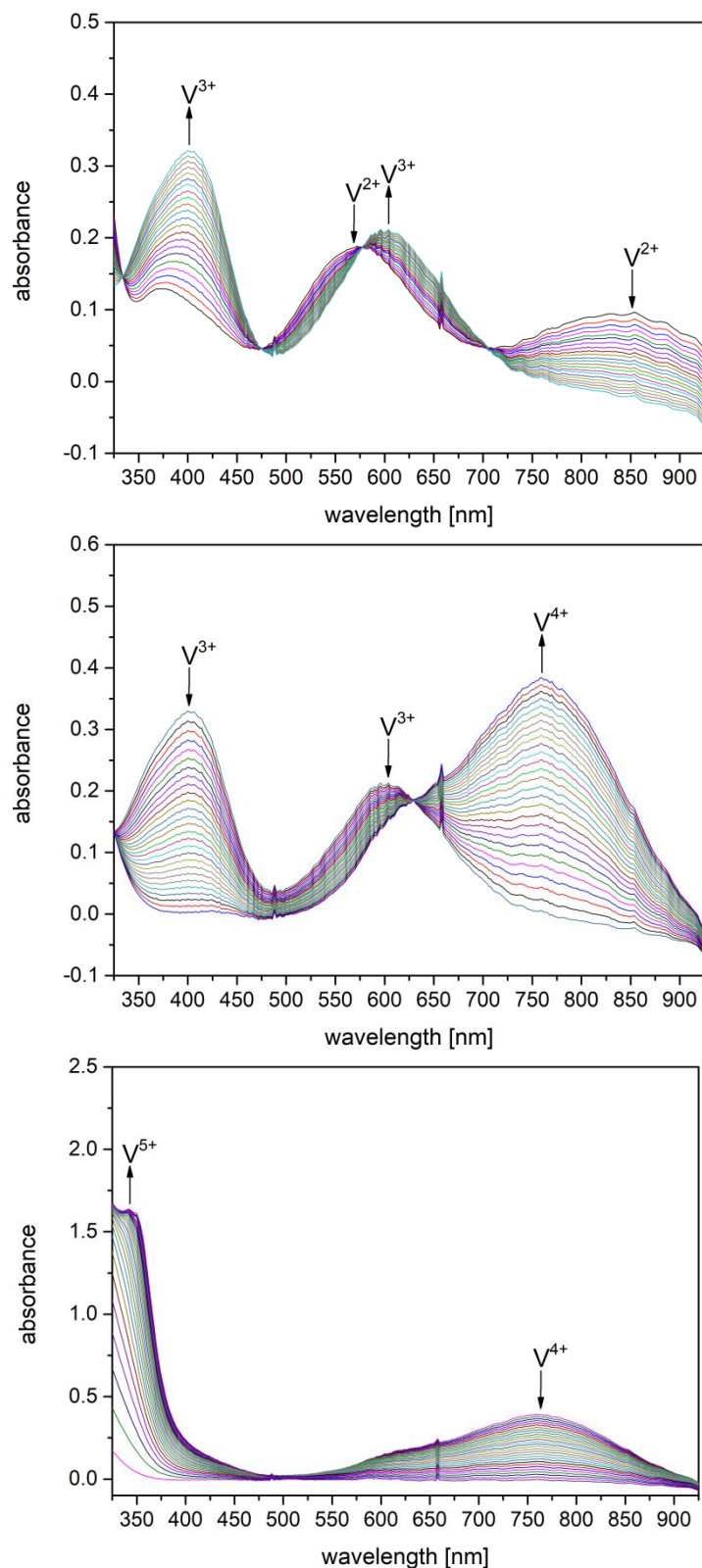


Fig. 26. Evolution of the UV/Vis/NIR spectral data during the oxidation of  $V^{2+}$  to  $V^{3+}$  (top),  $V^{3+}$  to  $V^{4+}$  (center) and  $V^{4+}$  to  $V^{5+}$  (bottom) for the initial total vanadium concentration  $[V_{total}] = 0.4 \text{ mol L}^{-1}$ .

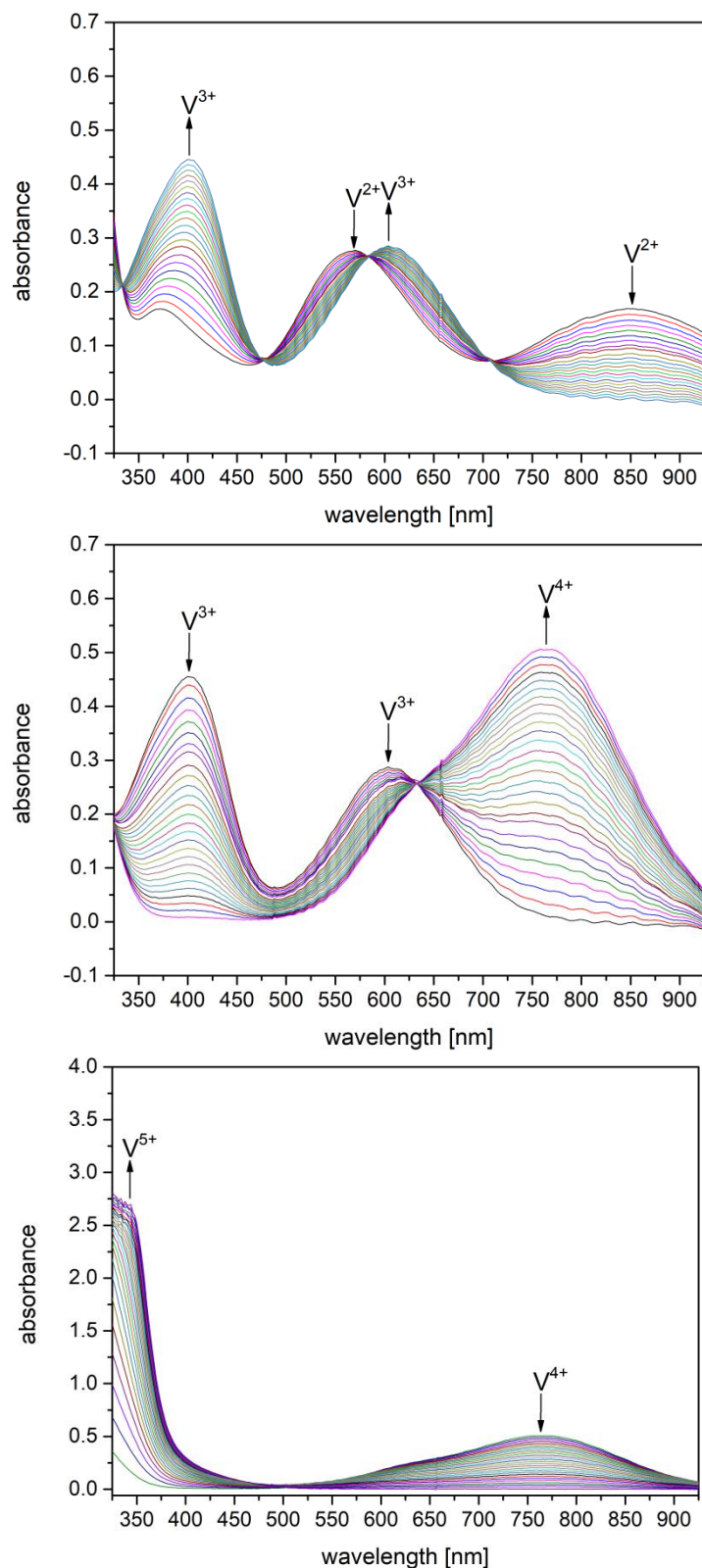


Fig. 27. Evolution of the UV/Vis/NIR spectral data during the oxidation of  $V^{2+}$  to  $V^{3+}$  (top),  $V^{3+}$  to  $V^{4+}$  (center) and  $V^{4+}$  to  $V^{5+}$  (bottom) for the initial total vanadium concentration  $[V_{total}] = 0.6 \text{ mol L}^{-1}$ .

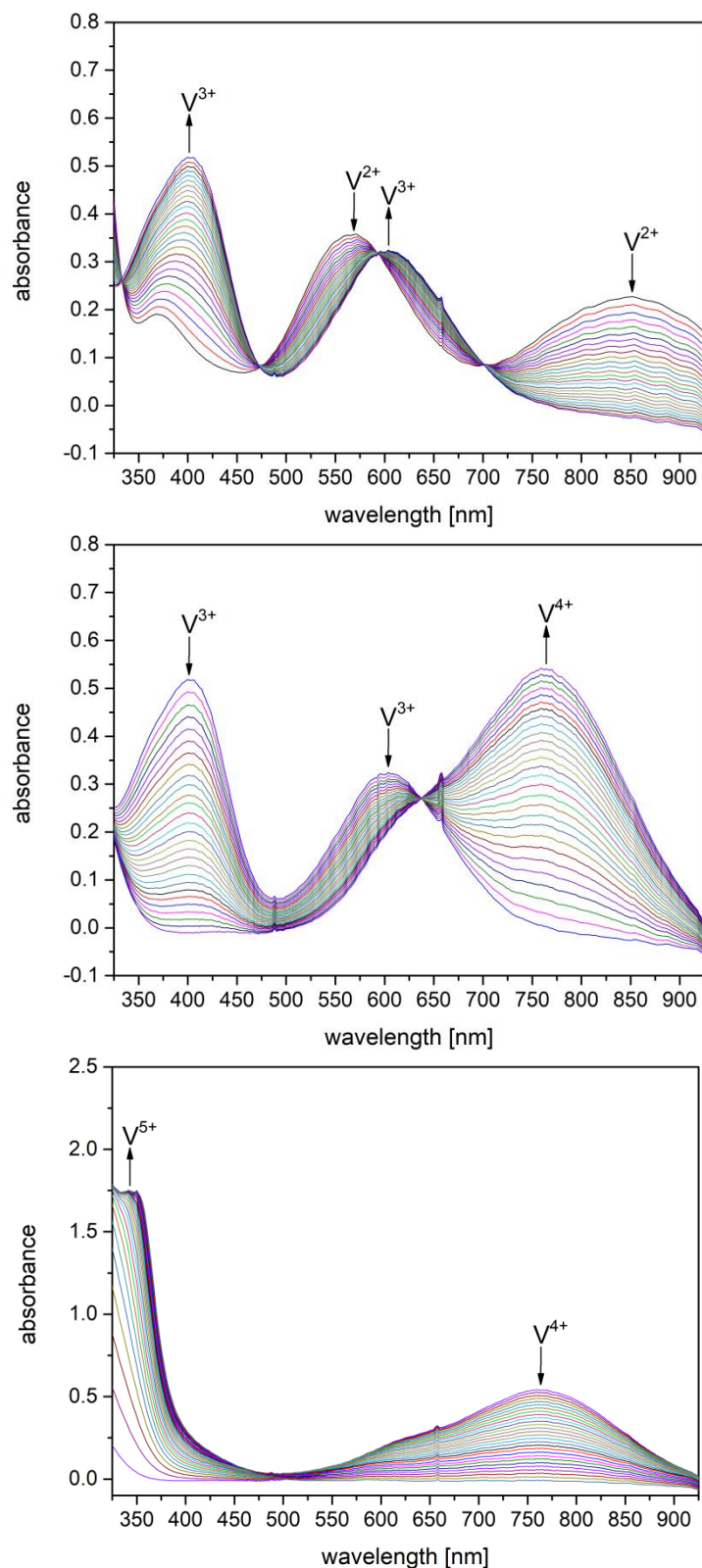


Fig. 28. Evolution of the UV/Vis/NIR spectral data during the oxidation of  $V^{2+}$  to  $V^{3+}$  (top),  $V^{3+}$  to  $V^{4+}$  (center) and  $V^{4+}$  to  $V^{5+}$  (bottom) for the initial total vanadium concentration  $[V_{total}] = 0.8 \text{ mol L}^{-1}$ .

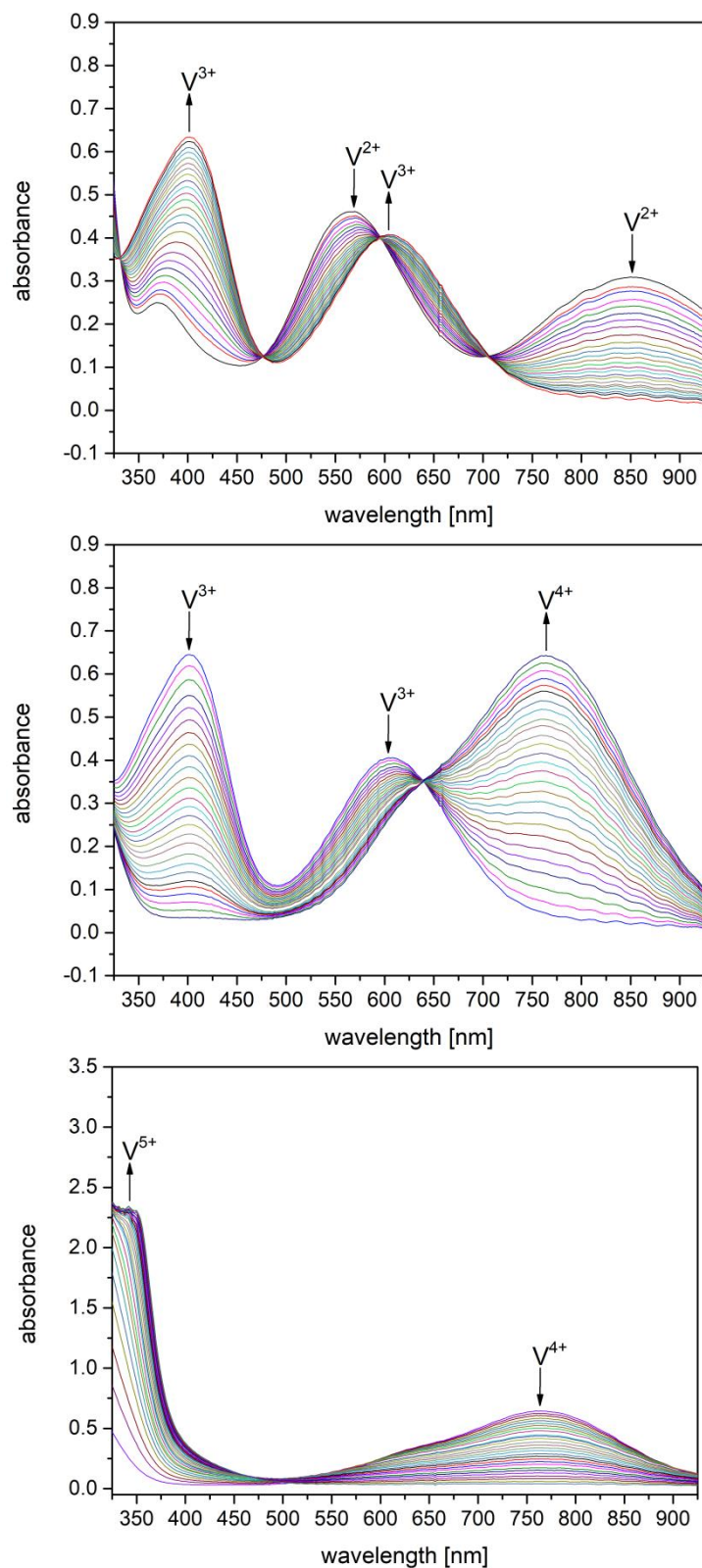


Fig. 29. Evolution of the UV/Vis/NIR spectral data during the oxidation of  $V^{2+}$  to  $V^{3+}$  (top),  $V^{3+}$  to  $V^{4+}$  (center) and  $V^{4+}$  to  $V^{5+}$  (bottom) for the initial total vanadium concentration  $[V_{total}] = 1.0 \text{ mol L}^{-1}$ .

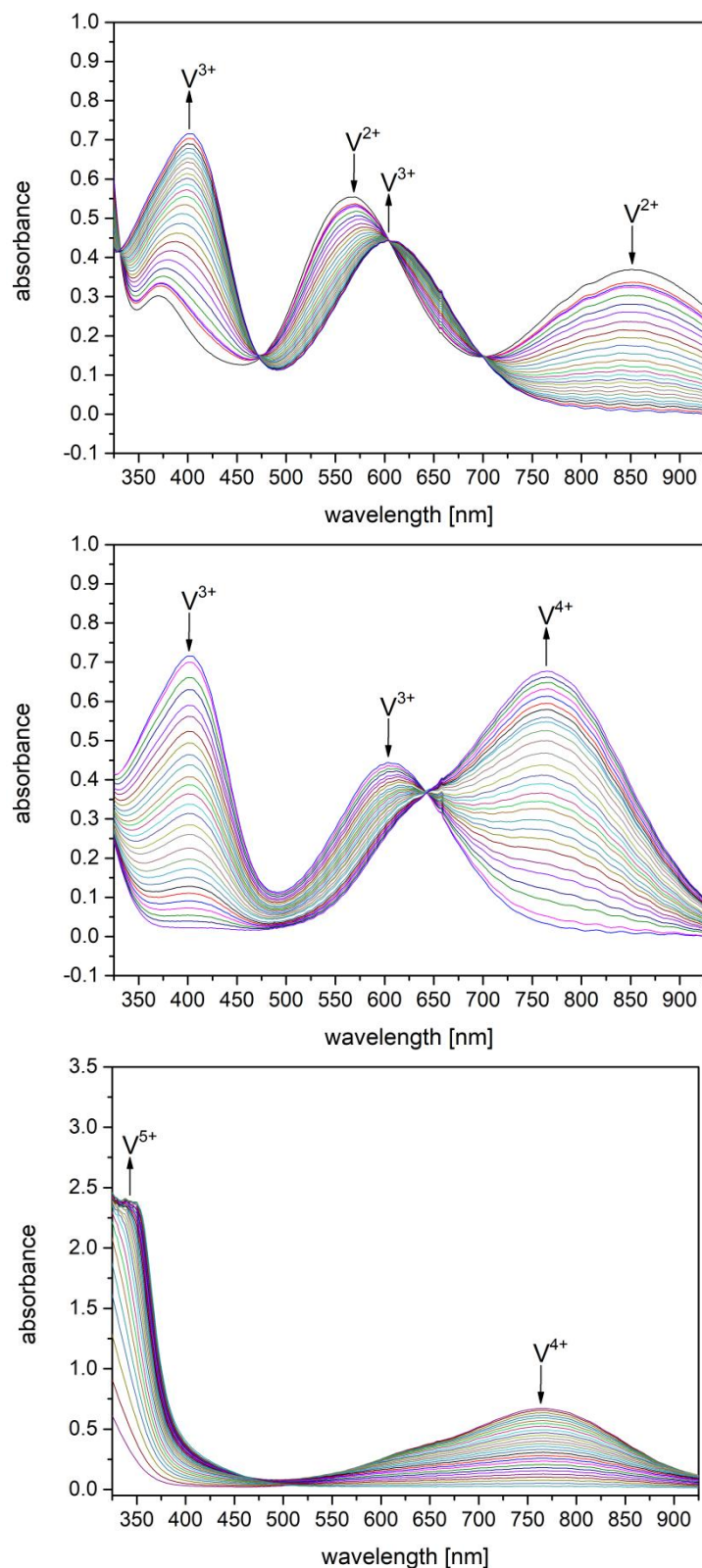


Fig. 30. Evolution of the UV/Vis/NIR spectral data during the oxidation of  $V^{2+}$  to  $V^{3+}$  (top),  $V^{3+}$  to  $V^{4+}$  (center) and  $V^{4+}$  to  $V^{5+}$  (bottom) for the initial total vanadium concentration  $[V_{total}] = 1.2 \text{ mol L}^{-1}$ .

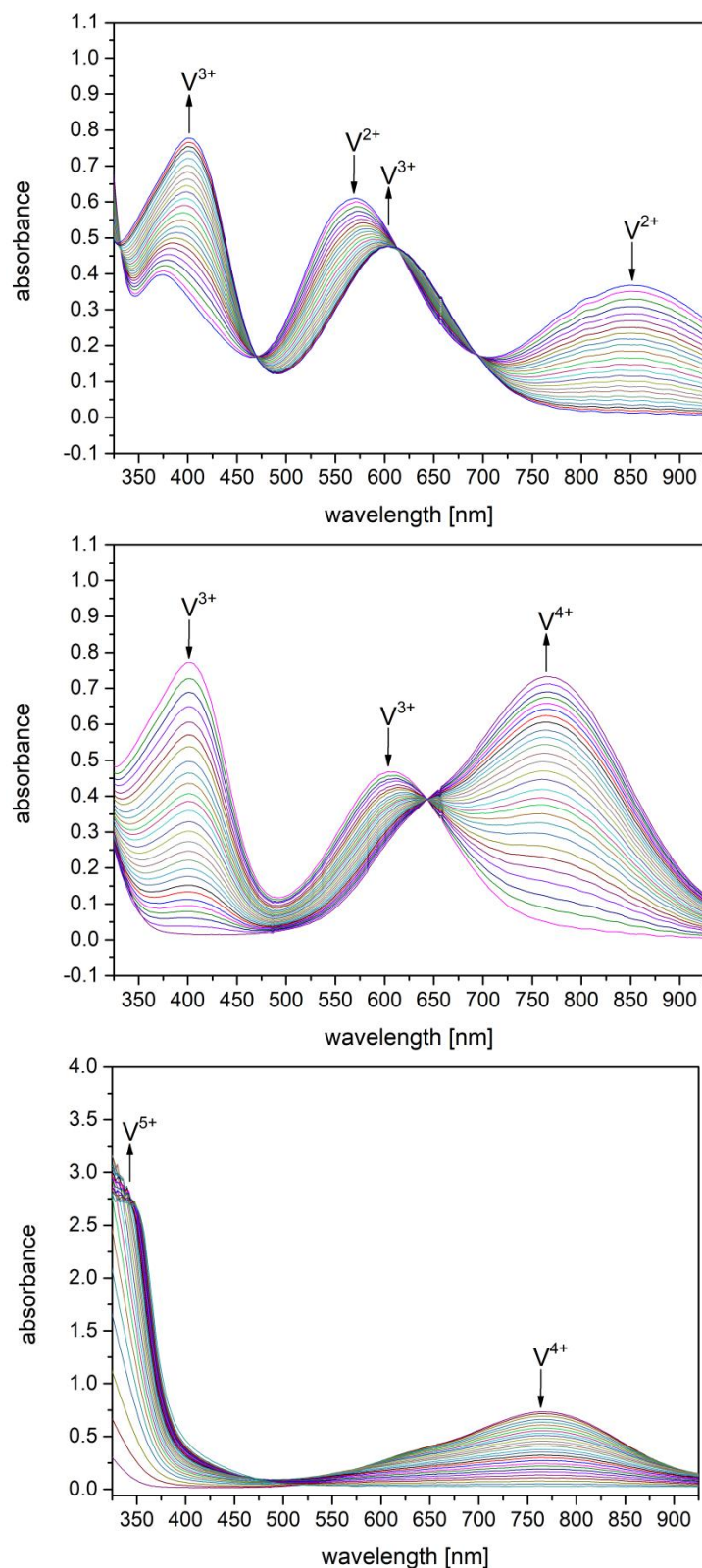


Fig. 31. Evolution of the UV/Vis/NIR spectral data during the oxidation of  $V^{2+}$  to  $V^{3+}$  (top),  $V^{3+}$  to  $V^{4+}$  (center) and  $V^{4+}$  to  $V^{5+}$  (bottom) for the initial total vanadium concentration  $[V_{total}] = 1.4 \text{ mol L}^{-1}$ .

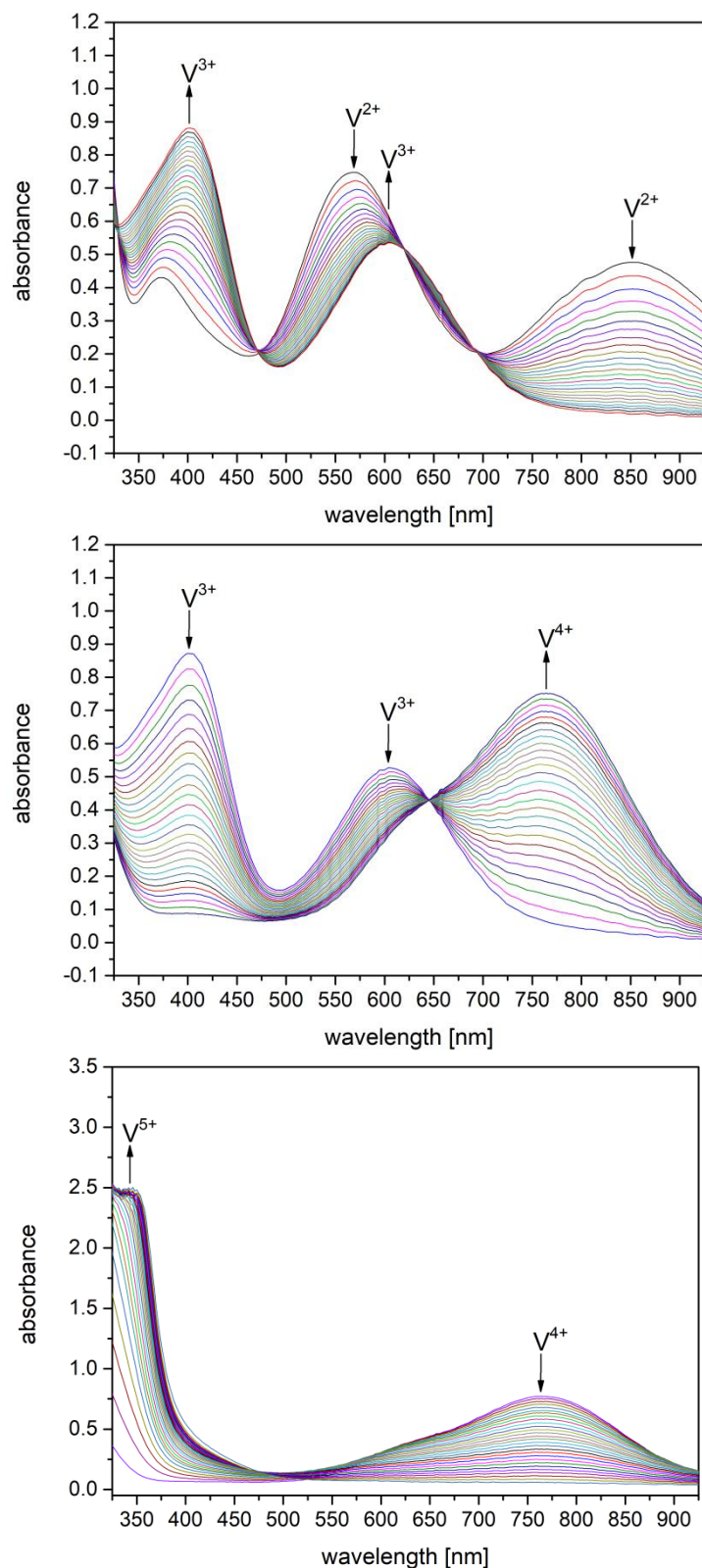


Fig. 32. Evolution of the UV/Vis/NIR spectral data during the oxidation of  $V^{2+}$  to  $V^{3+}$  (top),  $V^{3+}$  to  $V^{4+}$  (center) and  $V^{4+}$  to  $V^{5+}$  (bottom) for the initial total vanadium concentration  $[V_{total}] = 1.6 \text{ mol L}^{-1}$ .

### 4.2.3 Clear assignment of potential measurements to UV/Vis/NIR spectral data

Prior to the determination of the absorption coefficients the potential measurements have to be related to their corresponding UV/Vis/NIR spectral data. This clear assignment allows the reliable determination of the absorption coefficients for pure  $V^{2+}$  and  $V^{3+}$  at the initial total vanadium concentrations.

For an overview, the UV/Vis/NIR spectra of the entire oxidation of  $V^{2+}$  to  $V^{5+}$  are plotted versus the added volume of  $KMnO_4$  titrant solution (see Fig. 33). In the following chapter the determination of the absorption coefficients is conducted at wavelengths characteristic for  $V^{2+}$  and  $V^{3+}$ .

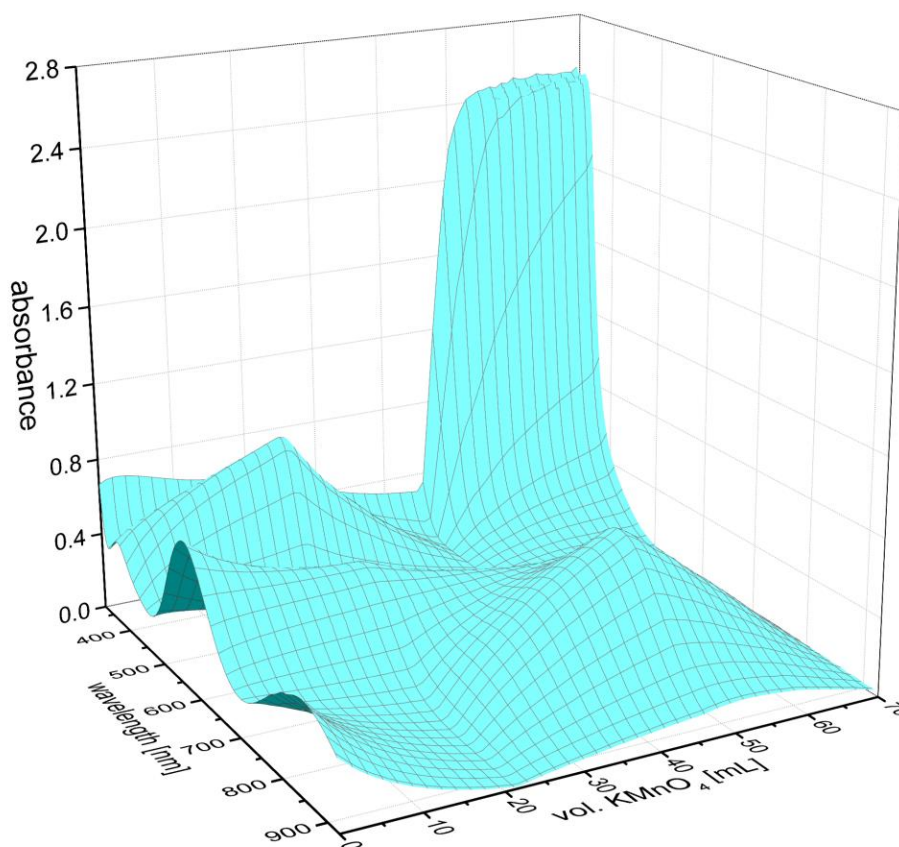


Fig. 33. Evolution of the UV/Vis/NIR spectra during the entire oxidation of  $V^{2+}$  to  $V^{5+}$  for the initial total vanadium concentration  $[V_{total}] = 1.6 \text{ mol L}^{-1}$  as a function of the added volume of  $0.2 \text{ mol L}^{-1} KMnO_4$  titrant solution.

#### 4.2.4 Determination of species-specific absorption coefficients

For the reliable determination of the absorption coefficients the consideration of the continuously increasing dilution of the sample solution and accordingly the steady reduction of its total vanadium concentration is of crucial interest. Therefore, the related absorbance value decrease during the titration process is taken into account [153]. The measured absorbance values of the complete titration process and consequently of all consecutively formed vanadium oxidation states are plotted as black rectangles in the Figures 34 and 35.

For the analysis of  $V^{3+}$  the wavelength of 400 nm is selected (see Figure 34). The analysis of  $V^{2+}$  is conducted at 850 nm as displayed in Figure 35 [153]. Thus, the sample's continuously increasing dilution is determined by calculation of the ratio of the sample's volume at the considered titration step and the sample's initial volume before the titration starts. Afterwards, the calculated ratio is multiplied with the measured absorbance values (in black rectangles) to obtain the dilution corrected absorbance values.

In the Figures 34 and 35 the red circles indicate the evolution of the dilution corrected absorbance values for the complete titration process and thus for all consecutively present vanadium species [153]. Figure 34 exhibits the dilution corrected  $V^{3+}$  absorbances at a wavelength of 400 nm. In Figure 35 the dilution corrected absorbance values of  $V^{2+}$  at 850 nm are outlined.

In each figure a linear relationship between the dilution corrected absorbance values and the added volume of the  $KMnO_4$  titrant solution is observed in the ranges of 0–22 mL (oxidation of  $V^{2+}$  to  $V^{3+}$ ) and of 22–46 mL (oxidation of  $V^{3+}$  to  $V^{4+}$ ), respectively [153]. The determination of the absorbance of pure  $V^{3+}$  is conducted in the first absorbance maximum at 400 nm (see Fig. 34). To obtain the absorbance maximum value the two flanks of the peak are linearly fitted and their intersection is determined. Consequently, the intersection point of these straight lines shown in Figure 34 yields the absorbance of pure  $V^{3+}$  with  $1.6 \text{ mol L}^{-1}$  total vanadium concentration at the wavelength  $\lambda = 400 \text{ nm}$ .

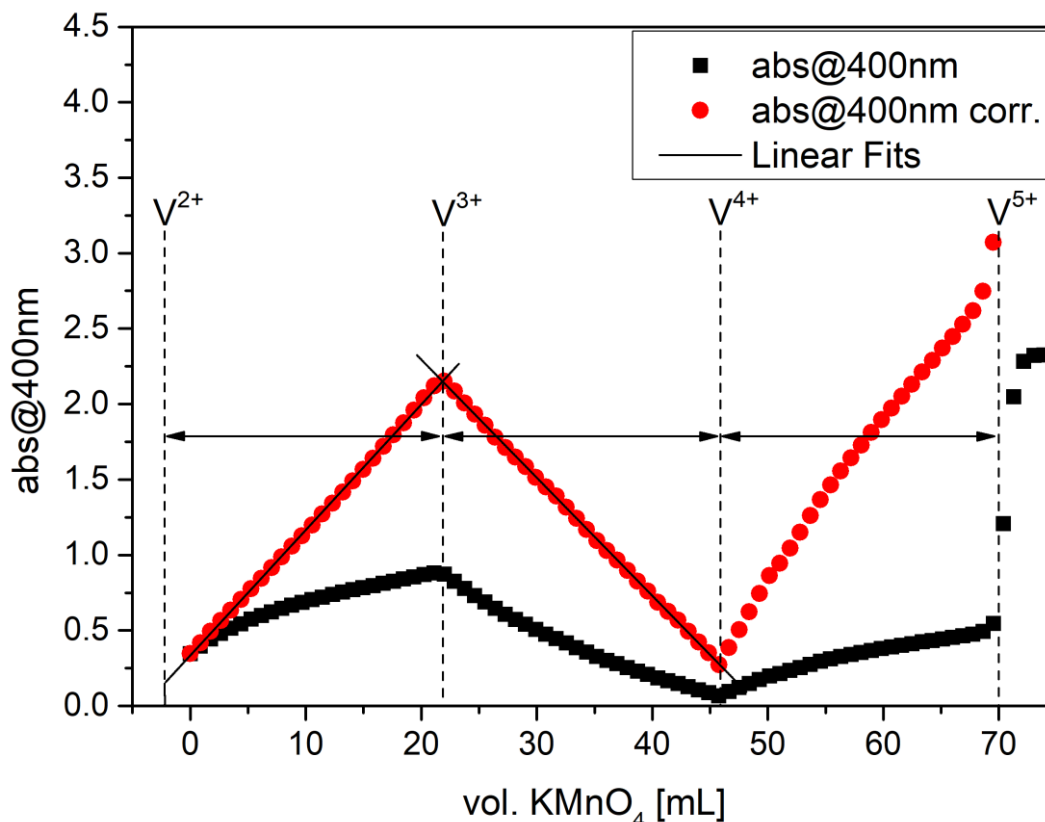


Fig. 34. Evolution of the absorbance at 400 nm during the oxidation of  $V^{2+}$  to  $V^{5+}$  plotted as a function of the dispensed volume of  $0.2 \text{ mol L}^{-1}$   $\text{KMnO}_4$  titrant solution for  $[V_{\text{total}}] = 1.6 \text{ mol L}^{-1}$  (black rectangles: experimental data with dilution effect; red circles: experimental data after removal of dilution effect) [153].

In case of the determination of the  $V^{2+}$  absorption coefficient at  $\lambda = 850 \text{ nm}$  an extrapolation to the absorbance of pure  $V^{2+}$  is required, because the starting sample solution already includes a small  $V^{3+}$  content. Thus, the pure  $V^{2+}$  absorbance is determined by initially fitting the first range of the plot of the absorbance values at 850 nm versus the added  $\text{KMnO}_4$  volume and afterwards extrapolating to a defined negative  $\text{KMnO}_4$  volume [153]. The corresponding extent of extrapolation is calculated by the volume difference between the first and the second stage of the regarded titration curve. Therefore, the obtained volume difference is equal to the atmospherically oxidized volume part of the sample solution. Its detection during the first titration stage is not possible due to its vanadium being already present as  $V^{3+}$  [153]. Thus, the introduced approach enables the determination of the absorbance of a pure  $V^{2+}$  solution by applying the measured absorbance values of the partly oxidized  $V^{2+}$  solution. Consequently, the described extrapolation yields the absorbance of pure  $V^{2+}$  with a total vanadium concentration of  $1.6 \text{ mol L}^{-1}$  at a wavelength of  $\lambda = 850 \text{ nm}$  [153].

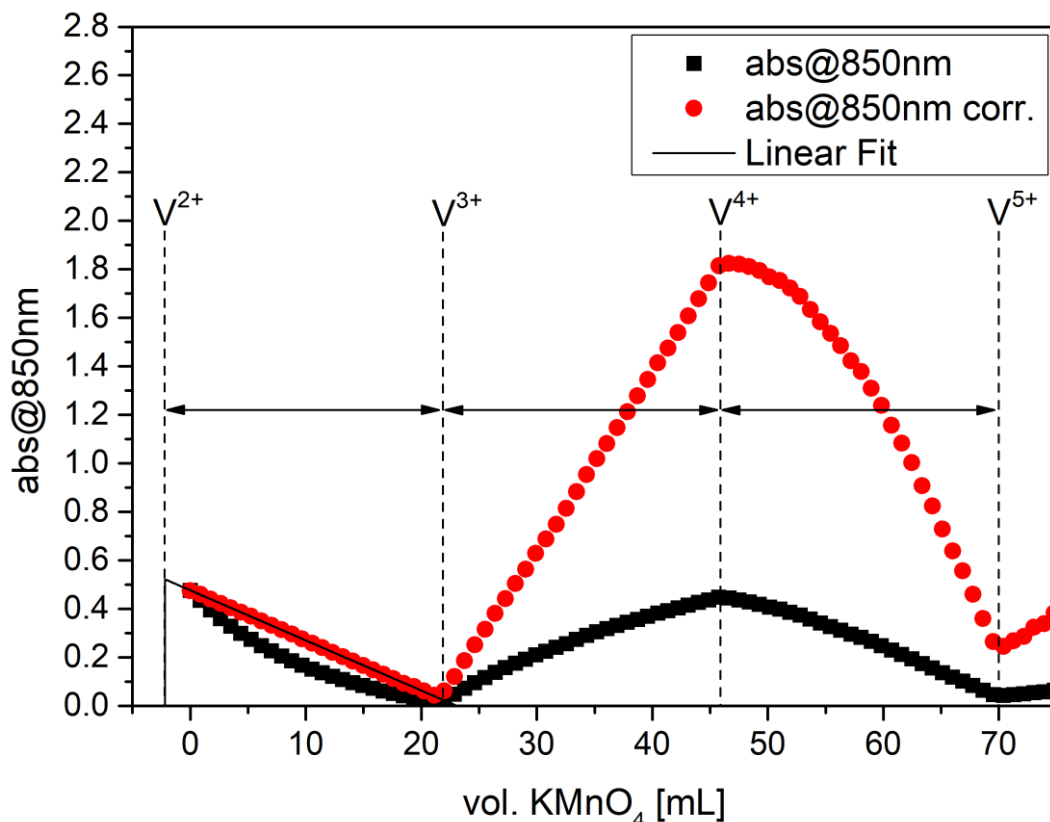


Fig. 35. Evolution of the absorbance at 850 nm during the oxidation of V<sup>2+</sup> to V<sup>5+</sup> plotted as a function of the dispensed volume of 0.2 mol L<sup>-1</sup> KMnO<sub>4</sub> titrant solution for [V<sub>total</sub>] = 1.6 mol L<sup>-1</sup> (black rectangles: experimental data with dilution effect; red circles: experimental data after removal of dilution effect) [153].

Further corresponding data evaluations are conducted for the samples of the total vanadium concentrations 0.2, 0.4, 0.6, 0.8, 1.0, 1.2 and 1.4 mol L<sup>-1</sup>. Contrarily to the first and second branch in both Figure 34 and 35, the third branch in each figure exhibits a non-linear relationship. The observed phenomenon apparently originates from the initial formation and the subsequent depletion of small quantities of the mixed-valence, binuclear charge transfer complex, which depends on the current V<sup>4+</sup>/V<sup>5+</sup> species ratio in the sample solution [147,153]. In Figure 36 the absorbances for pure V<sup>3+</sup> at 400 nm and for pure V<sup>2+</sup> at 850 nm are plotted as a function of the initial total vanadium concentration. The obtained proportionality is expected after Lambert–Beer's law. In case of V<sup>2+</sup> the linear fit describes the data very well. For V<sup>3+</sup> the data shows some deviations from the linear fit function [153].

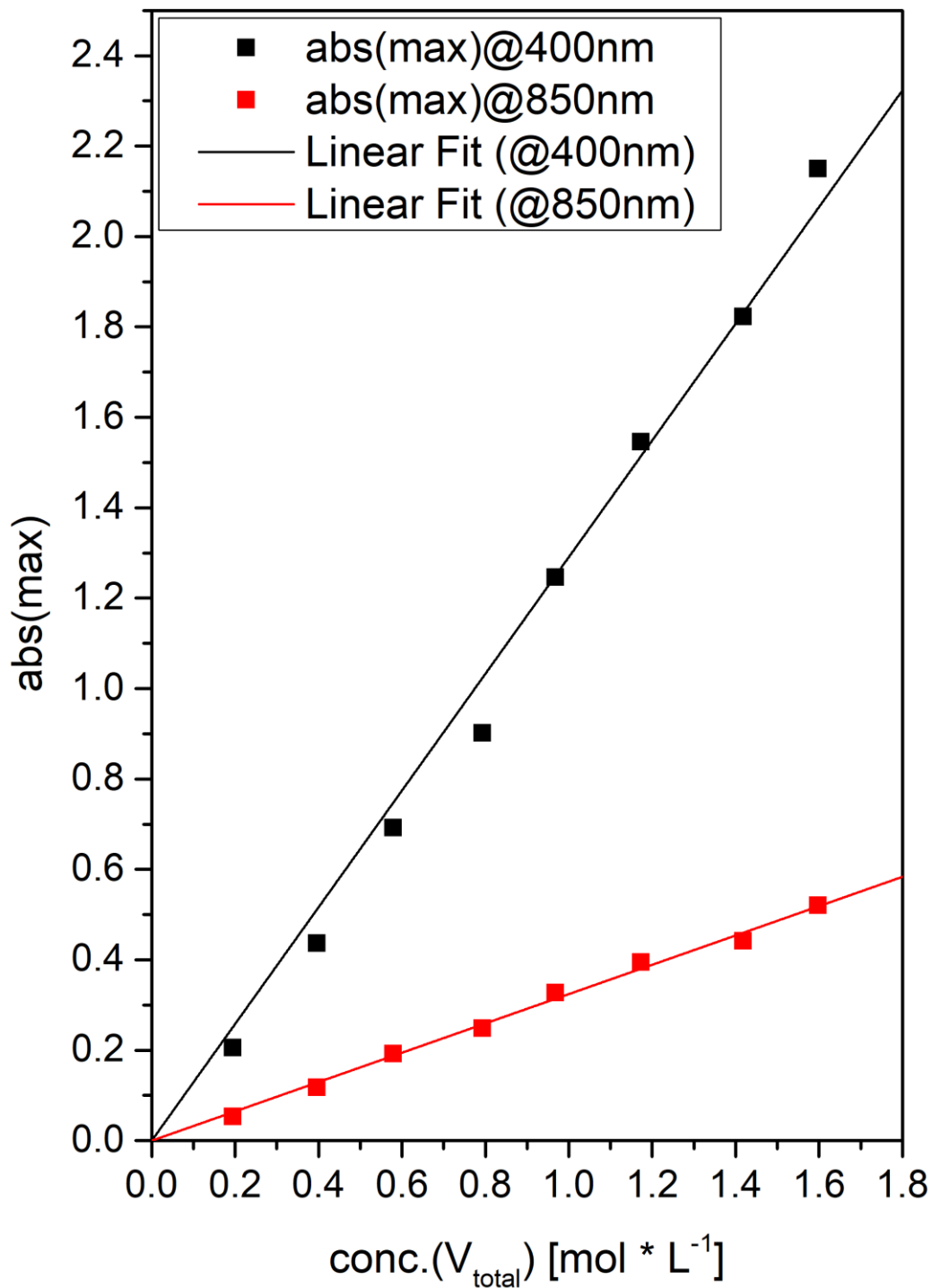


Fig. 36. Pure  $V^{2+}$  absorbances at 850 nm (red rectangles) and pure  $V^{3+}$  absorbances at 400 nm (black rectangles) as a function of the  $V^{2+}$  and  $V^{3+}$  concentration, respectively [153].

In Figure 37 the absorption coefficients for pure  $V^{2+}$  and pure  $V^{3+}$  are plotted versus the related initial total vanadium concentration. The calculation is conducted by means of Lambert-Beer's law. Similarly to Figure 36, the linear fit function exhibits less deviations in case of  $V^{2+}$  compared to  $V^{3+}$ .

Besides, the absorption coefficients usually stay constant while increasing the initial total vanadium concentration. For  $V^{3+}$  in the investigated vanadium electrolyte samples a direct proportionality between the absorption coefficients and the sample's total vanadium concentration is obtained. This behavior probably originates from the production of the vanadium electrolyte. In the production process vanadium is dissolved in the sulfuric acid as the corresponding sulfate compound. Thus, an increasing vanadium concentration in the sample causes a rising sulfate concentration. The additional sulfate species potentially alter the vanadium aqua complexes by substituting water ligands in the coordination sphere by sulfate ligands. Consequently, a probable explanation for the larger deviations in case of  $V^{3+}$  and the observed proportionality is an equilibrium among different absorbing  $V^{3+}$  species occurring in the sample solutions [153].

The resulting dependence between the  $V^{3+}$  absorption coefficients  $\epsilon_{400nm}(V^{3+})$  and the corresponding total vanadium concentration is described in equation (33):

$$\epsilon_{400\text{ nm}}(V^{3+}) = 2.03 * \text{conc.}(V_{\text{total}}) + 10.35 \quad (33)$$

Hence, for a total vanadium concentration of  $1.6 \text{ mol L}^{-1}$  which is commonly applied in the VRFB a  $V^{3+}$  absorption coefficient  $\epsilon_{400nm}(V^{3+})$  of  $13.60 \text{ L mol}^{-1} \text{ cm}^{-1}$  is determined.

Contrarily, the  $V^{2+}$  absorption coefficients  $\epsilon_{850nm}(V^{2+})$  do not depend on the total vanadium concentration and exhibit only slight variations. Thus, a constant  $V^{2+}$  absorption coefficient of

$$\epsilon_{850\text{ nm}}(V^{2+}) = 3.24 \pm 0.04 \frac{\text{L}}{\text{mol} * \text{cm}} \quad (34)$$

is obtained.

Therefore, by means of equation (33) and (34) the actual  $V^{2+}$  and  $V^{3+}$  absorption coefficients for the initial total vanadium concentrations in the range of  $0.2 \text{ mol L}^{-1}$  to  $1.6 \text{ mol L}^{-1}$  are made accessible.

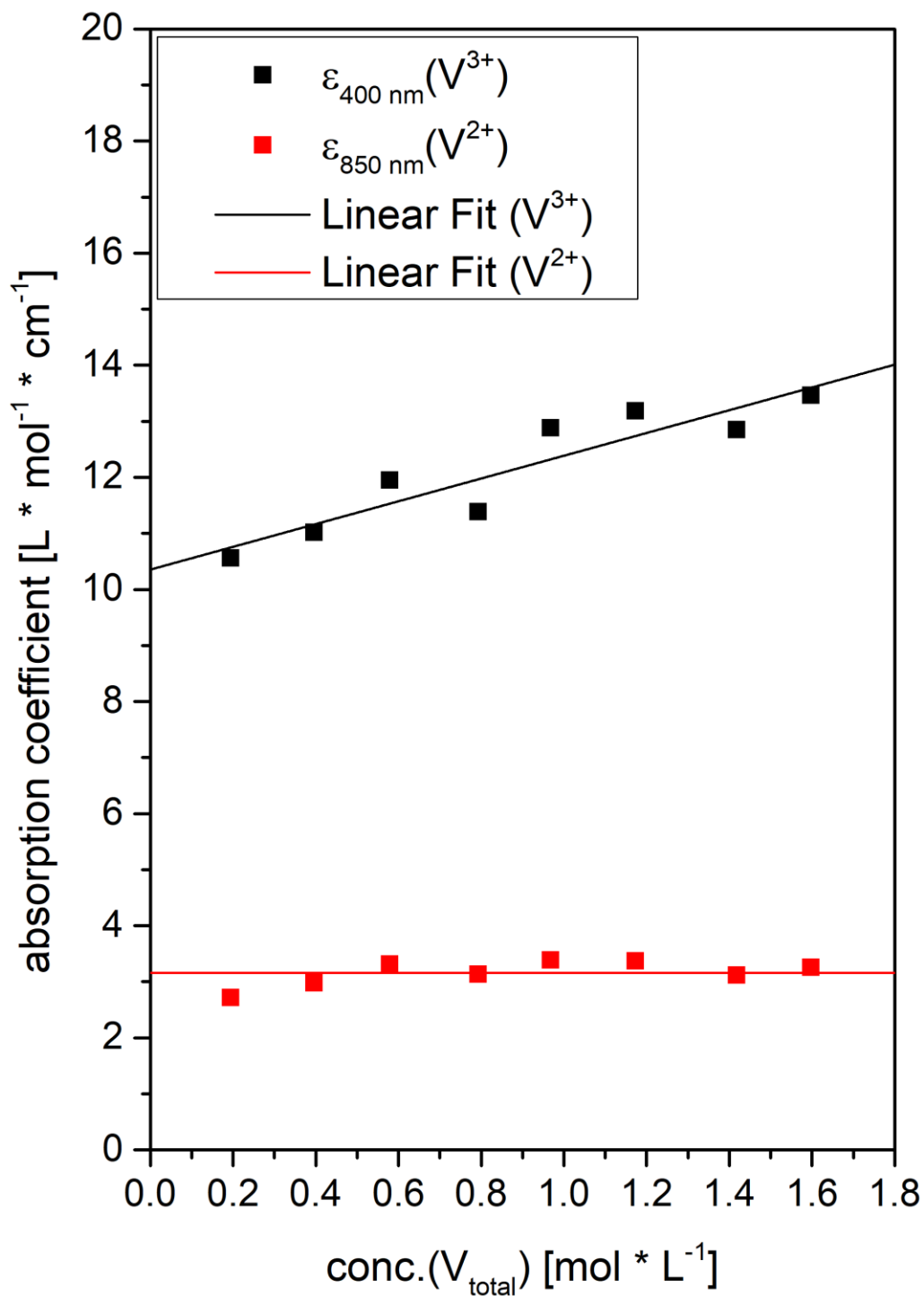


Fig. 37. Absorption coefficients for pure  $\text{V}^{2+}$  at 850 nm (red rectangles) and pure  $\text{V}^{3+}$  at 400 nm (black rectangles) as a function of the  $\text{V}^{2+}$  and  $\text{V}^{3+}$  concentration, respectively.

The future photometric determination of the half-cell specific partial states-of-charge in the VRFB electrolytes is enabled due to the knowledge of the species-specific UV/Vis/NIR absorption coefficients. By means of Lambert-Beer's law the concentrations of the differently oxidized vanadium ions can be calculated [153]. With the applied relationships given by equation (8) and (9) the two partial states-of-charge of the anolyte ( $SOC_{2/3}$ ) and the catholyte ( $SOC_{4/5}$ ) are accessible now:

$$\text{Negative partial state - of - charge: } SOC_{2/3} = \frac{[V^{2+}]}{[V^{2+}]+[V^{3+}]} = \frac{[V^{2+}]}{[V_{total}]} \quad (8)$$

$$\text{Positive partial state - of - charge: } SOC_{4/5} = \frac{[V^{5+}]}{[V^{4+}]+[V^{5+}]} = \frac{[V^{5+}]}{[V_{total}]} \quad (9)$$

Henceforth, the photometric determination of the  $[V^{2+}]$  and  $[V^{3+}]$  concentrations in the VRFB anolyte is made possible at the commonly applied high total vanadium concentrations. A basic prerequisite is the availability of a UV/Vis/NIR flow-through cell/cuvette with a sufficiently small optical path length as already discussed in chapter 3. In the VRFB catholyte the photometric determination of the  $[V^{4+}]$  and  $[V^{5+}]$  concentration is generally complicated because of two reasons [153].

The first reason is the intermediate formation and subsequent depletion of the mixed-valence binuclear complex. This process prevents the direct photometric determination of the  $V^{4+}$  concentration. The second reason is the need to conduct the  $V^{5+}$  absorbance measurements in the flank of the very strong  $V^{5+}$  absorption at  $\lambda < 450$  nm as displayed in Figure 23. Usually, the measurements performed in the flank of an absorption maximum are less robust compared to peak measurements [153].

Besides, the dilution effect of the used titration technique strongly reduces the concentration of  $V^{4+}$  and  $V^{5+}$  in the current sample solution. Thus in contrast to the concentrated vanadium solutions (see chapter 3), the formed amount of the mixed-valence complex is too low to detect its corresponding absorption peaks. Additionally, the  $V^{5+}$  absorbance flank changes its shape depending on the actual  $V^{5+}$  concentration. Due to the described consequences of the dilution effect on the UV/Vis/NIR spectra a reliable determination of the  $V^{4+}$  and  $V^{5+}$  absorption coefficients for concentrated vanadium solutions by means of the spectral data with dilution effect is prevented.

#### 4.2.5 Conclusions

The a priori presented method couples potentiometric titration with in-situ UV/Vis/NIR spectroscopy. Starting with a partly oxidized  $V^{2+}$  electrolyte sample which contains mostly  $V^{2+}$  and some  $V^{3+}$  nearly the entire oxidation process from pure  $V^{2+}$  to pure  $V^{5+}$  is taking place during the titration. With the simultaneously conducted in-situ UV/Vis/NIR spectroscopy the evolution of the sample's absorbance data is monitored in the course of the complete titration process. Therefore, alterations in the sample's chemical composition can be detected immediately.

Due to knowledge of the amount of added titrant solution for every absorbance spectrum the determination of the oxidation state specific and the total vanadium concentrations is enabled. Besides, the coupling of both measurement techniques allows for reliable determination of the  $V^{2+}$  and  $V^{3+}$  absorption coefficients by means of the corresponding absorbance maxima.

The issue of the  $V^{2+}$  oxidation sensitivity is solved for the determination of its absorption coefficient by an extrapolation procedure. Thus, the measured absorbance of partly oxidized samples (mostly  $V^{2+}$  and some  $V^{3+}$ ) can be extrapolated to the absorbance maxima of pure  $V^{2+}$  samples. For the sample's preparation and its transfer into titration set-up strictly inert conditions are not necessary. Additionally, the  $V^{2+}$  and  $V^{3+}$  absorption coefficients are obtained in the complete range of  $0.2 \text{ mol L}^{-1}$  to  $1.6 \text{ mol L}^{-1}$ . Consequently, by means of Lambert-Beer's law the negative partial state-of-charge  $\text{SOC}_{2/3}$  is accessible for this entire total vanadium concentration range using photometry.

## 5. Comparison of both techniques

The approach of the potentiometric titration combined with in-situ UV/Vis/NIR spectrometry (see chapter 4) determines the  $V^{2+}$  and  $V^{3+}$  absorption coefficients (route 1) for a “conventional” UV/Vis/NIR photometric determination of the  $[V^{2+}]$  and  $[V^{3+}]$  concentrations in the VRFB anolyte. By means of these primary and absolute data together with  $SOC_{2/3} = [V^{2+}]/([V^{2+}] + [V^{3+}])$  (Eq. 8), the negative partial state-of-charge of the anolyte is obtained. Although this  $SOC_{2/3}$  is a secondary, relative quantity, it is specific for the negative half-cell [148,153].

As explained before, route 1 requires the absorption coefficients at the selected wavelengths. For the vanadium electrolyte the commonly used calibration curves (absorbance vs. concentration) are not applicable. In this case the investigated species are only different oxidation states of the same element. Thus, they very easily transmute. Therefore, in route 1 in-situ UV/Vis/NIR spectrometry is combined with potentiometric titration. The determination of the  $V^{2+}$  and  $V^{3+}$  absorption coefficients is conducted with a special extrapolation method described in chapter 4 [148,153].

Besides, the approach explained in chapter 3 deals with the straightforward determination of  $SOC_{2/3}$  by means of UV/Vis/NIR photometry (route 2). It is based on a calibration of the absorbance values to the related OCV data of a VRFB in the balanced state, also described as a pristine VRFB. Only one wavelength needs to be measured [148]. Thus, in the VRFB anolyte only the  $V^{3+}$  species is considered. According to the comparison displayed in Figure 38 both calibration techniques for the anolyte provide the same results.

In case of the VRFB catholyte the commonly applied UV/Vis/NIR spectrometry faces the problem of intermediate  $V^{4+}$ - $V^{5+}$  mixed-valence complex formation at large vanadium concentrations. Its related very intense UV/Vis absorption consequently inhibits the determination of the  $V^{4+}$  concentration [148,153]. Contrarily, the straightforward UV/Vis photometry of route 2 needs the absorbance characteristic of just one species/oxidation state per VRFB half-cell. Therefore, the approach of route 2 is applicable for the  $SOC_{4/5}$  determination of the VRFB catholyte. However, special care is required because the absorbance determination is conducted in the flank of a strong absorption band [148,153].

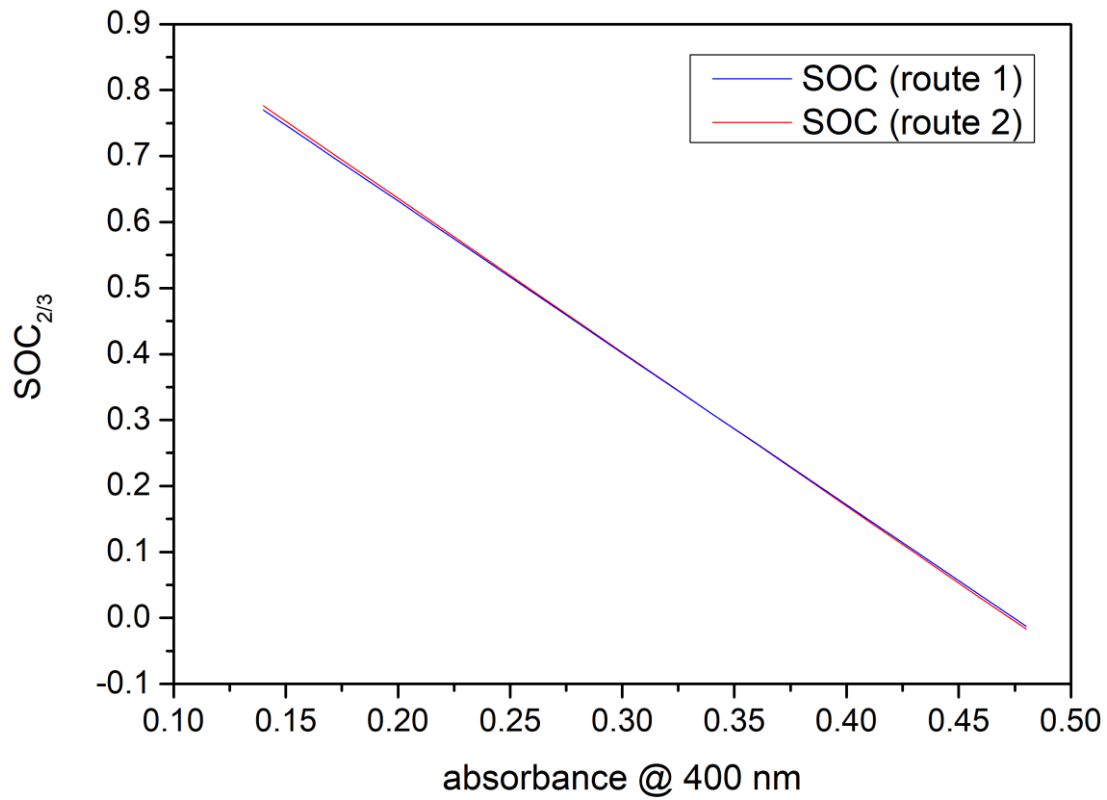


*Fig. 38. Comparison of the UV/Vis/NIR data for the analyte based on different calibrations, see chapter 5 [148].*

## 6. Summary and outlook

The main objective of this PhD thesis was the development of an improved state-of-charge sensor for the all-vanadium redox flow battery. Thereby, the study is focused on the improvement on several fields of the current VRFB technology like the facilitation of in-situ SOC measurements, the accessibility of half-cell specific partial state-of-charge information, the ability to perform vanadium oxidation state specific SOC monitoring and the long-term applicability of the sensor in the electrolyte circuit. Accordingly, two different approaches which address these concerns are introduced.

One approach couples potentiometric titration with in-situ UV/Vis/NIR absorbance spectroscopy. The starting point of the titration is a  $V^{2+}$  solution sample (titrand) produced by fully charging a negative VRFB electrolyte. Due to the practically unavoidable atmospherical oxidation of  $V^{2+}$  during the sample's preparation and transfer into the titration set-up the  $V^{2+}$  sample solution contains a small part of  $V^{3+}$ . Eight sample solutions are investigated with a total vanadium concentration in the range of  $0.2 \text{ mol L}^{-1}$  to  $1.6 \text{ mol L}^{-1}$ . As titrant a  $0.2 \text{ mol L}^{-1}$   $\text{KMnO}_4$  solution is applied.

Simultaneously to the potentiometric titration in-situ UV/Vis/NIR spectroscopy is conducted by means of an optical quartz immersion probe (optical path length = 1 mm). Accordingly, the changes of the sample's absorbance data during the complete titration process are monitored. Thus, alterations in the sample's chemical composition are instantly registered. With the assignment of the volume of added titrant solution to its corresponding absorbance spectrum the oxidation state specific and the total vanadium concentrations are accessible. Besides, the combination of the two measurement techniques enables the accurate determination of the  $V^{2+}$  and  $V^{3+}$  absorption coefficients using their related absorbance maxima (for pure  $V^{2+}$ :  $\lambda = 850 \text{ nm}$ , for pure  $V^{3+}$ :  $\lambda = 400 \text{ nm}$ ).

A crucial challenge is the  $V^{2+}$  oxidation sensitivity. For the determination of the  $V^{2+}$  absorption coefficient this issue is solved by a special extrapolation procedure. Hence, the absorbance maxima of pure  $V^{2+}$  samples are obtained by extrapolating the related absorbance of partly oxidized samples (mostly  $V^{2+}$  and some  $V^{3+}$ ). Therefore, strictly inert conditions are not required for both the sample's preparation and transfer into the titration apparatus. Besides, the absorbance spectra of the commercially available, highly concentrated catholyte exhibit intensive peaks corresponding to the intermediate binuclear  $V^{4+}$ - $V^{5+}$  complex formation [147]. These peaks are absent in case of the diluted samples which are present towards the end of the titration due to the dilution by the  $\text{KMnO}_4$  titrant solution. Thus, the low concentration absorption coefficients are not applicable for the highly concentrated electrolyte.

However, contrarily to the next approach, a complete range of differently concentrated vanadium anolytes is made accessible for SOC sensing. The resulting  $V^{2+}$  and  $V^{3+}$  absorption coefficients are obtained in the entire concentration range of  $0.2 \text{ mol L}^{-1}$  to  $1.6 \text{ mol L}^{-1}$ . Hence, the  $V^{2+}$  absorption coefficient  $\epsilon_{850\text{nm}}(V^{2+})$  is  $3.24 \pm 0.04 \text{ L mol}^{-1} \text{ cm}^{-1}$ . The  $V^{3+}$  absorption coefficient is proportional to the sample's initial total vanadium concentration. Probably, the cause is an equilibrium among different absorbing  $V^{3+}$  complexes which is altered depending on the sample's initial total vanadium and sulfate concentration.

The dependence of the  $V^{3+}$  absorption coefficient is described by  $\epsilon_{400\text{nm}}(V^{3+}) = 2.03 \times \text{conc.}(V_{\text{total}}) + 10.35$ . Thus, the  $V^{2+}$  and  $V^{3+}$  concentrations are simultaneously accessible and accordingly their sum which equals the anolyte's total vanadium concentration can be determined. Consequently, the photometrical determination of the negative partial state-of-charge  $\text{SOC}_{2/3}$  can be conducted in this complete total vanadium concentration range.

The other approach combines in-situ UV/Vis/NIR absorbance spectrometry with in-situ open-circuit-voltage measurements for in-operando half-cell specific SOC monitoring. Vanadium electrolyte in the balanced state with a total vanadium concentration of  $1.6 \text{ mol L}^{-1}$  is applied within the complete measurement process. Initially, the values of an open-circuit-voltage curve are determined during the charging operation of the concentrated vanadium electrolyte in a VRFB single cell. Then, the measured OCV curve is mathematically described by means of a fit function based on Nernst's equation. Thus, each OCV value is related to its corresponding SOC value. Additionally, the fit procedure considers both the absence of standard conditions in the vanadium electrolyte and the proton formation and depletion in the course of the charge-discharge cycling. Due to the simultaneous operation of the UV/Vis/NIR spectroscopy and the OCV measurement, the UV/Vis/NIR spectroscopic sensor's calibration on SOC is conducted using the SOC-related OCV values. This calibration is performed in-operando and separately for both half-cell electrolytes (anolyte and catholyte respectively).

For the state-of-charge monitoring of the anolyte the  $V^{3+}$  absorption maximum at  $\lambda = 400 \text{ nm}$  is selected. The absorbance values at  $400 \text{ nm}$  are linearly proportional to the negative partial state-of-charge  $\text{SOC}_{2/3}$  according to:  $\text{SOC}_{2/3}(\text{abs}) = 1.10 - 2.33 \times \text{abs}(@ 400 \text{ nm})$ . Depending on the concentrated catholyte's actual  $V^{4+}/V^{5+}$  ratio intensive absorption peaks are registered within the range  $500 \text{ nm} \leq \lambda \leq 900 \text{ nm}$ . These absorption peaks correspond to the intermediate binuclear  $V^{4+}-V^{5+}$  complex formation and subsequent depletion during the charge-discharge operation of the VRFB [147]. Accordingly, this circumstance prevents the direct monitoring of the  $V^{4+}$  absorption maximum at  $\lambda = 760 \text{ nm}$ . Therefore, the  $V^{5+}$  absorption flank at  $\lambda = 440 \text{ nm}$  is chosen for the SOC determination of the catholyte instead. The dependence of  $V^{5+}$  absorbances at  $440 \text{ nm}$  on the positive partial state-of-charge  $\text{SOC}_{4/5}$  is described with a third order polynomial as will be shown in the following:  $\text{SOC}_{4/5}(\text{abs}) = 0.09 - 1.06 \times \text{abs} + 3.17 \times \text{abs}^2 - 1.49 \times \text{abs}^3$  (abs = absorbance at  $440 \text{ nm}$ ). Consequently, this SOC sensing technique requires just a single vanadium species specific absorption maximum per VRFB half-cell electrolyte.

This improved spectrometric state-of-charge sensor is particularly suitable for in-situ applications. It allows instant and independent SOC monitoring and protects the oxygen-sensitive  $V^{2+}$  species from atmospheric oxidation. Additionally, the SOC sensor can be applied in the negative and positive vanadium electrolyte. Due to the separate half-cell specific VRFB electrolyte's analysis the negative as well as the positive partial state-of-charge ( $\text{SOC}_{2/3}$  and  $\text{SOC}_{4/5}$ ) is directly accessible. Besides, the different vanadium species in the electrolyte exhibit specific colors according to their current vanadium oxidation state. With the used UV/Vis/NIR spectrometric technique the distinction between the different vanadium oxidation states is enabled and their present concentrations can be determined. Each of the additionally obtained information provides substantially more detailed insights in the vanadium electrolyte's chemical composition and its changes induced by the VRFB's charge-discharge cycling.

Furthermore, a durable quartz flow-through cell/cuvette with optimized path length is applied for the UV/Vis/NIR absorbance spectroscopy. It protects the surrounding sensor hardware against the corrosive electrolyte and guarantees adequate optical conductivity. Thus, with the choice of quartz for the flow-through cuvette the failure probability of the VRFB electrolyte contacting material is minimized and the cuvette's long-term applicability in the electrolyte circuit is ensured. Consequently, longer maintenance intervals and therefore extended operation times of the current SOC sensor are achieved.

Henceforth, with these valuable features of the improved in-situ UV/Vis/NIR SOC sensor arising deviations from the vanadium concentration's target condition are registered in-operando at an early stage as well as half-cell and oxidation-state specifically. Additionally, the electrolyte circuits remain closed during each SOC measurement which preserves the  $V^{2+}$  species from atmospherical oxidation. Thus, an enhancement of the VRFB's energy efficiency during operation is achieved combined with less maintenance effort of the vanadium electrolyte. The application of durable quartz as electrolyte contacting material significantly reduces the SOC sensor's maintenance efforts as well as the related costs and further improves the VRFB's entire operating efficiency.

Although the presented in-situ UV/Vis/NIR SOC sensor clearly improves several crucial specifications of the current SOC monitoring technology some aspects exhibit potential for further investigations. As previously outlined, based on the already conducted measurements the  $V^{2+}$  absorption maximum at 850 nm can be examined more detailed. The yet low absorption intensity results in a weak sensitivity towards slight absorption changes. Thus, slight SOC alterations are hardly detected. This issue can be solved with the adjustment of the flow-through cuvette's optical path length from 200  $\mu\text{m}$  to approximately 1 mm.

Additionally, for the commercialization of the presented in-situ UV/Vis/NIR SOC sensor the related modular UV/Vis/NIR spectrometer set-up can be simplified. The photometry at species-specific wavelength selected in this study will replace the measurement of full UV/Vis/NIR spectra. Therefore, the deuterium/halogen light source can be exchanged by a cheap radiation source e.g. a LED with the appropriate emission wavelength. Similarly, the UV/Vis/NIR spectrometer is replaceable by a simple semiconductor detector like a photodiode. Besides, if the flow-through cuvette is specially constructed for the commercial SOC sensor optical special glass can most likely be applied instead of quartz. With these measures both costs and complexity of the commercial in-situ photometrical SOC sensor are noticeably reduced.

Furthermore, the application of both approaches introduced in this study is not limited to the chemistry of the vanadium electrolyte. The potentiometric titration coupled in-situ UV/Vis/NIR absorbance spectrometry can also be used for absorption coefficient determination of other oxidizable species in solution as long as they absorb in the given UV/Vis/NIR range. Accordingly, the same applies for the described in-situ UV/Vis/NIR SOC sensor. Its field of application is not limited to the all-vanadium redox flow battery. In fact, this SOC sensor can be adopted to different battery chemistries provided that the redox-active species exhibit absorption peaks within the UV/Vis/NIR spectral range. Due to its modular set-up the in-situ SOC sensor is flexible. The set-up components can be adjusted or replaced if the sensor's measuring range is exceeded.



## 7. References

- [1] J.J. Ephraums, G.J.J. Jenkins, *Climate change 1992*, Cambridge University Press (1992) pp. 1–202.
- [2] Gesetz für den Ausbau erneuerbarer Energien (Erneuerbare-Energien-Gesetz – EEG 2014), *Bundesgesetzblatt* 24. Juli 2014 pp. 1066–1132.
- [3] Federal Ministry for Economic Affairs and Energy, *Development of Renewable Energy Sources in Germany 2017*, <https://www.erneuerbare-energien.de/EE/Redaktion/DE/Downloads/development-of-renewable-energy-sources-in-germany-2017.html> (accessed 16th October 2018).
- [4] H. Lund, *Energy* 32 (2007) 912–919.
- [5] W.P. Schill, J. Diekmann, A. Zerrahn, *DIW-Wochenbericht*, 82 (2015) 195–205.
- [6] J. Egerer, C. Gerbaulet, R. Ihlenburg, F. Kunz, B. Reinhard, C. von Hirschhausen, A. Weber, J. Weibezahn, *DIW Data Documentation* 72 (2014) 1–118.
- [7] H. Lund, G. Salgi, *Energ. Convers. Manage.* 50 (2009) 1172–1179.
- [8] J. McDowall, *J. Power Sources* 162 (2006) 959–964.
- [9] T. Kousksou, P. Bruel, A. Jamil, T. El Rhafiki, Y. Zeraouli, *Sol. Energ. Mat. Sol. C.* 120 (2014) 59–80.
- [10] L. Joerissen, J. Garche, C. Fabjan, G. Tomazic, *J. Power Sources* 127 (2004) 98–104.
- [11] J. Baker, *Energy Policy* 36 (2008) 4368–4373.
- [12] Y.K. Zeng, T.S. Zhao, L. An, X.L. Zhou, L. Wei, *J. Power Sources* 300 (2015) 438–443.
- [13] B. Dunn, H. Kamath, J.M. Tarascon, *Science* 334 (2011) 928–935.
- [14] A. Lucas, S. Chondrogiannis, *Int. J. Electr. Power Energy Syst.* 80 (2016) 26–36.
- [15] T. Lepold, D. Goerges, *IEEE CCTA* (2017) 799–805.
- [16] A. Lucas, F. Bonavitacola, E. Kotsakis, G. Fulli, *Electr. Pow. Syst. Res.* 127 (2015) 13–21.
- [17] Á. Cunha, F.P. Brito, J. Martins, N. Rodrigues, V. Monteiro, J.L. Afonso, P. Ferreira, *Energy* 115 (2016) 1478–1494.
- [18] G.J. Osório, J.M. Lujano-Rojas, M. Shafie-khah, J.C.O. Matias, J.P.S. Catalão, *IEEE PESGM* (2015) 1–5.
- [19] C. Minke, U. Kunz, T. Turek, *J. Power Sources* 361 (2017) 105–114.

## References

---

- [20] project network "OptiCharge", <http://projekt-opticharge.de/> (accessed 16th October 2018, picture trimmed).
- [21] J. Noack, N. Roznyatovskaya, T. Herr, P. Fischer, *Angew. Chem. Int. Ed.* 54 (2015) 9776–9809.
- [22] W. Wang, Q. Luo, B. Li, X. Wei, L. Li, Z. Yang, *Adv. Funct. Mater.* 23 (2013) 970–986.
- [23] P. Alotto, M. Guarnieri, F. Moro, *Renew. Sustainable Energy Rev.* 29 (2014) 325–335.
- [24] Z. Yang, J. Zhang, M.C.W. Kintner-Meyer, X. Lu, D. Choi, J.P. Lemmon, J. Liu, *Chem. Rev.* 111 (2011) 3577–3613.
- [25] L. Li, S. Kim, W. Wang, M. Vijayakumar, Z. Nie, B. Chen, J. Zhang, G. Xia, J. Hu, G. Graff, J. Liu, Z. Yang, *Adv. Energy Mater.* 1 (2011) 394–400.
- [26] M. Skyllas-Kazacos, L. Cao, M. Kazacos, N. Kausar, A. Mousa, *ChemSusChem* 9 (2016) 1521–1543.
- [27] T. Shigematsu, *SEI technical review* 73 (2011) 5–13.
- [28] C.P. De Leon, A. Frías-Ferrer, J. González-García, D.A. Szánto, F.C. Walsh, *J. Power Sources* 160 (2006) 716–732.
- [29] A.Z. Weber, M.M. Mench, J.P. Meyers, P.N. Ross, J.T. Gostick, Q. Liu, *J. Appl. Electrochem.* 41 (2011) 1137–1164.
- [30] K. C. Divya, J. Østergaard, *Electr. Power Syst. Res.* 79 (2009) 511.
- [31] M. Skyllas-Kazacos, G. Kazacos, G. Poon, H. Verseema, *Int. J. Energy Res.* 34 (2010) 182–189.
- [32] L.H. Thaller, US Patent 3996064, (1976).
- [33] C.S. Bradley, US-Patent 312802, (1885).
- [34] M. Skyllas-Kazacos, F. Grossmith, *J. Electrochem. Soc.* 134 (1987) 2950–2953.
- [35] A. Hazza, D. Pletcher, R. Wills, *Phys. Chem. Chem. Phys.*, 6 (2004) 1773–1778.
- [36] C. Bae, E.P.L. Roberts, M.H. Chakrabarti, M. Saleem, *Int.J. Green Energy* 8 (2011) 248–264.
- [37] Q. Liu, A.E.S. Sleightholme, A.A. Shinkle, Y. Li, L.T. Thompson, *Electrochem. Commun.*, 11 (2009) 2312–2315.
- [38] T. Janoschka, M.D. Hager, U.S. Schubert, *Adv. Mater.*, 24 (2012) 6397–6409.
- [39] R. Chen, R. Hempelmann, *Electrochem. Commun.*, 70, (2016) 56–59.
- [40] J.J. Lingane, *J. Am. Chem. Soc.* 67 (1945) 182–188.
- [41] D.G. Davis, Jr., *Talanta* 3 (1960) 335–345.

## References

---

- [42] Y. Israel, L. Meites, *J. Electroanal. Chem.* 8 (1964) 99–119.
- [43] W. Kangro, H. Pieper, *Electrochim. Acta* 7 (1962) 435–448.
- [44] M. Skyllas-Kazacos, M. Rychcik, R.G. Robins, A.G. Fane, M.A. Green, *J. Electrochem. Soc.* 133 (1986) 1057–1058.
- [45] E. Sum, M. Skyllas-Kazacos, *J. Power Sources* 15 (1985) 179–190.
- [46] E. Sum, M. Rychcik, M. Skyllas-Kazacos, *J. Power Sources* 16 (1985) 85–95.
- [47] Z. González, A. Sánchez, C. Blanco, M. Granda, R. Menéndez, R. Santamaría, *Electrochem. Commun.* 13 (2011) 1379–1382.
- [48] X. Li, H. Zhang, Z. Mai, H. Zhang, I. Vankelecom, *Energy Environ. Sci.* 4 (2011) 1147–1160.
- [49] A. Parasuraman, T.M. Lim, C. Menictas, M. Skyllas-Kazacos, *Electrochim. Acta* 101 (2013) 27–40.
- [50] B. Sun, M. Skyllas-Kazacos, *Electrochim. Acta* 36 (1991) 513–517.
- [51] B. Sun, M. Skyllas-Kazacos, *Electrochim. Acta* 37 (1992) 1253–1260.
- [52] B. Sun, M. Skyllas-Kazacos, *Electrochim. Acta* 37 (1992) 2459–2465.
- [53] C. Ponce-de-León, G.W. Reade, I. Whyte, S.E. Male, F.C. Walsh, *Electrochim. Acta* 52 (2007) 5815–5823.
- [54] D.J. Suárez, Z. González, C. Blanco, M. Granda, R. Menéndez, R. Santamaría, *ChemSusChem* 7 (2014) 914–918.
- [55] Y. Shao, X. Wang, M. Engelhard, C. Wang, S. Dai, J. Liu, Z. Yang, Y. Lin, *J. Power Sources* 195 (2010) 4375–4379.
- [56] Z. He, L. Shi, J. Shen, Z. He, S. Liu, *Int. J. Energy Res.* 39 (2015) 709–716.
- [57] H.Q. Zhu, Y.M. Zhang, L. Yue, W.S. Li, G.L. Li, D. Shu, H.Y. Chen, *J. Power Sources* 184 (2008) 637–640.
- [58] B. Caglar, P. Fischer, P. Kauranen, M. Karttunen, P. Elsner, *J. Power Sources* 256 (2014) 88–95.
- [59] M. Park, Y.-J. Jung, J. Ryu, J. Cho, *J. Mater. Chem. A* 2 (2014) 15808–15815.
- [60] M. Skyllas-Kazacos, M.H. Chakrabarti, S. a. Hajimolana, F.S. Mjalli, M. Saleem, *J. Electrochem. Soc.* 158 (2011) R55–R79.
- [61] X. Li, K. Huang, S. Liu, L. Chen, *J. Cent. South Univ. Technol.* 14 (2007) 51–56.
- [62] N. Tan, H. Kelong, L. Suqin, L. Xiaogang, C. Zhifeng, *Acta Chim. Sin.* (2006) 64.

## References

---

- [63] X. Li, K. Huang, S. Liu, N. Tan, L. Chen, *Trans. Nonferrous Met. Soc. China* 17 (2007) 195–199.
- [64] S. Zhong, M. Kazacos, R.P. Burford, M. Skyllas-Kazacos, *J. Power Sources* 36 (1991) 29–43.
- [65] M. Kazacos, M. Skyllas-Kazacos, *J. Electrochem. Soc.* 136 (1989) 2759–2760.
- [66] P. Qian, H. Zhang, J. Chen, Y. Wen, Q. Luo, Z. Liu, D. You, B. Yi, *J. Power Sources* 175 (2008) 613–620.
- [67] M.S. Yazici, D. Krassowski, J. Prakash, *J. Power Sources* 141 (2005) 171–176.
- [68] A. Brungs, V. Haddadi-Asl, M. Skyllas-Kazacos, *J. Appl. Electrochem.* 26 (1996) 1117–1123.
- [69] S. Zhong, M. Kazacos, U.S. Patent 5665212 (1997).
- [70] V. Haddadi-Asl, M. Kazacos, M. Skyllas-Kazacos, *J. Appl. Electrochem.* 25 (1995) 29–33.
- [71] V. Haddadi-Asl, M. Kazacos, M. Skyllas-Kazacos, *J. Appl. Polym. Sci.* 57 (1995) 1455–1463.
- [72] K. Schmidt-Rohr, Q. Chen, *Nat. Mater.* 7 (2008) 75.
- [73] H. Prifti, A. Parasuraman, S. Winardi, T.M. Lim, M. Skyllas-Kazacos, *Membranes* 2 275–306.
- [74] D. Chen, M.A. Hickner, E. Agar, C. Kumbur, *Electrochem. Commun.* 26 (2013) 37–40.
- [75] X. Teng, Y. Zhao, J. Xi, Z. Wu, X. Qiu, L. Chen, *J. Power Sources* 189 (2009) 1240–1246.
- [76] J. Xi, Z. Wu, X. Qiu, L. Chen, *J. Power Sources* 166 (2007) 531–536.
- [77] J. Kim, J.D. Jeon, S.Y. Kwak, *Electrochem. Commun.* 38 (2014) 68–70.
- [78] D. Chen, S. Wang, M. Xiao, D. Han, Y. Meng, *J. Power Sources* 195 (2010) 7701–7708.
- [79] J. Pan, S. Wang, M. Xiao, M. Hickner, Y. Meng, *J. Membr. Sci.* 443 (2013) 19–27.
- [80] N. Wang, S. Peng, D. Lu, S. Liu, Y. Liu, K. Huang, *J. Solid State Electrochem.* 16 (2012) 1577–1584.
- [81] J. Zeng, C. Jiang, Y. Wang, J. Chen, S. Zhu, B. Zhao, R. Wang, *Electrochem. Commun.* 10 (2008) 372–375.
- [82] B. Schwenzer, S. Kim, M. Vijayakumar, Z. Yang, J. Liu, *J. Membr. Sci.* 372 (2011) 11–19.

## References

---

- [83] G. Kear, A.A. Shah, F.C. Walsh, *Int. J. Energy Res.* 36 (2012) 1105–1120.
- [84] D.T. Richens, *The Chemistry of Aqua Ions: Synthesis, structure and reactivity*, JOHN WILEY & SONS, Chichester, 1997, pp. 224–243.
- [85] M. Kazacos, *Electrolyte optimization and electrode material evaluation for the vanadium redox battery*, MSc Thesis, University of New South Wales (Australia), 1989.
- [86] R.J.H. Clark, *The Chemistry of Titanium and Vanadium*, Elsevier, New York, 1968.
- [87] M. Benmelouka, S. Messaoudi, E. Furet, R. Gautier, E. Le Fur, J.-Y. Pivan, *J. Phys. Chem. A* 107 (2003) 4122–4129.
- [88] F. Sepehr, S.J. Paddison, *Chem. Phys. Lett.* 585 (2013) 53–58.
- [89] M. Vijayakumar, S.D. Burton, C. Huang, L. Li, Z. Yang, G.L. Graff, J. Liu, J. Hu, M. Skyllas-Kazacos, *J. Power Sources* 195 (2010) 7709–7717.
- [90] S.C. Larsen, *J. Phys. Chem. A* 105 (2001) 8333–8338.
- [91] C.V. Grant, W. Cope, J.A. Ball, G.G. Maresch, B.J. Gaffney, W. Fink, R.D. Britt, *J. Phys. Chem. B* 103 (1999) 10627–10631.
- [92] H. Strehlow, H. Wendt, *Inorg. Chem.* 2 (1963) 6–10.
- [93] A.A. Ivakin, E.M. Voronova, *Russ. J. Inorg. Chem.* 18 (1973) 956.
- [94] F.A. Cotton, G. Wilkinson, P.L. Gaus, *Basic Inorganic Chemistry*, Wiley, New York, 1976.
- [95] M. Bühl, M. Parrinello, *Chem. Eur. J.* 7 (2001) 4487–4494.
- [96] J. Krakowiak, D. Lundberg, I. Persson, *Inorg. Chem.* 51 (2012) 9598–9609.
- [97] M. Vijayakumar, L. Li, G. Graff, J. Liu, H. Zhang, Z. Yang, J. Hu, *J. Power Sources* 196 (2011) 3669–3672.
- [98] C. Choi, S. Kim, R. Kim, Y. Choi, S. Kim, H. Jung, J.H. Yang, H. Kim, *Renew. Sustainable Energy Rev.* 69 (2017) 263–274.
- [99] R. Akesson, L.G.M. Pettersson, M. Sandstrom, U. Wahlgren, *J. Am. Chem. Soc.* 116 (1994) 8691–8704.
- [100] M. Vijayakumar, L. Li, Z. Nie, Z. Yang, J. Hu, *Phys. Chem. Chem. Phys.* 14 (2012) 10233–10242.
- [101] Y.S. Yusfin, T.N. Bazilevich, P.I. Chernousov, A.L. Petelin, V.I. Gubanov, A.Y. Travyanov, *Metallurgist* 42 (1998) 209–211.
- [102] A. Shibata, K. Sato, *Power Eng. J.* 13 (1999) 130–135.

## References

---

- [103] M. Kubata, H. Nakaishi, N. Tokuda, (The Kansai Electric Power Co., Japan), US7258947B2, 2002.
- [104] F. Rahman, M. Skyllas-Kazacos, *J. Power Sources* 189 (2009) 1212–1219.
- [105] P. Zhao, H. Zhang, H. Zhou, J. Chen, S. Gao, B. Yi, *J. Power Sources* 162 (2006) 1416–1420.
- [106] D.G. Oei, *J. Appl. Electrochem.* 15 (1985) 231–235.
- [107] M. Skyllas-Kazacos, M. Kazacos, R.J.C. McDermott, (Unisearch, Australia), WO1989005363A1, 1988.
- [108] M. Kazacos, M. Cheng, M. Skyllas-Kazacos, *J. Appl. Electrochem.* 20 (1990) 463–467.
- [109] M. Skyllas-Kazacos, M. Kazacos, R. McDermott, Patent Application PCT/AU1988/000471, 1988.
- [110] F. Chang, C. Hu, X. Liu, L. Liu, J. Zhang, *Electrochim. Acta* 60 (2012) 334–338.
- [111] K. Ngamsai, A. Arpornwichanop, *J. Power Sources* 282 (2015) 534–543.
- [112] T. Sukkar, M. Skyllas-Kazacos, *J. Membr. Sci.* 222 (2003) 235–247.
- [113] M. Kazacos, M. Skyllas-Kazacos, (Unisearch, Australia), WO1996035239A1, 1996.
- [114] M. Skyllas-Kazacos, US20040241552A1, 2004.
- [115] Y. Tanaka, K. Horikawa, M. Mita, N. Tokuda, M. Kubata, US6613298B2, 2001.
- [116] M. Keshavarz, G. Zu, (Deeya Energy, USA) US20130095362A1, 2013.
- [117] F. Rahman, M. Skyllas-Kazacos, *J. Power Sources* 72 (1998) 105–110.
- [118] M. Cheng, Electrolyte optimization and studies for the vanadium redox battery, MSc Thesis, University of New South Wales (Australia), 1991.
- [119] Y. Wen, Y. Xu, J. Cheng, G. Cao, Y. Yang, *Electrochim. Acta* 96 (2013) 268–273.
- [120] J. Xi, Z. Wu, X. Teng, Y. Zhao, L. Chen, X. Qiu, *J. Mater. Chem.* 18 (2008) 1232–1238.
- [121] Z. Tang, D.S. Aaron, A.B. Papandrew, T.A. Zawodzinski Jr, *ECS Trans.* 41 (2012) 1–9.
- [122] I. Derr, M. Bruns, J. Langner, A. Fetyan, J. Melke, C. Roth, *J. Power Sources* 325 (2016) 351–359.
- [123] I. Derr, D. Przyrembel, J. Schweer, A. Fetyan, J. Langner, J. Melke, M. Weinelt, C. Roth, *Electrochim. Acta* 246 (2017) 783–793.
- [124] S. Corcuera, M. Skyllas-Kazacos, *Eur. Chem. Bull.* 1 (2012) 511–519.
- [125] M.R. Mohamed, H. Ahmad, M.N. Abu Seman, *Elektron. Elektrotech.* 19 (2013) 37–42.

## References

---

- [126] S. Ressel, F. Billa, L. Holtz, N. Janshen, A. Chica, T. Flower, C. Weidlich, T. Struckmann, *J. Power Sources* 378 (2018) 776–783.
- [127] A. Ejigu, M. Edwards, D.A. Walsh, *ACS Catal.* 5 (2015) 7122–7130.
- [128] K.W. Kim, S.M. Kim, S. Choi, J. Kim, I.S. Lee, *ACS Nano* 6 (2012) 5122–5129.
- [129] C.T.J. Grothuis, *Ann. Chem.* LVIII (1806) 54.
- [130] N. Kausar, *Studies of V<sup>IV</sup> and V<sup>V</sup> Species in Vanadium Cell Electrolyte*, PhD Thesis, University of New South Wales (Australia), 2002.
- [131] A. Mousa, *Chemical and Electrochemical Studies of V<sup>III</sup> and V<sup>II</sup> Solutions in Sulfuric Acid Solution for Vanadium Battery Applications*, PhD Thesis, University of New South Wales (Australia), 2003.
- [132] M. Skyllas-Kazacos, M. Kazacos, *J. Power Sources* 196 (2011) 8822–8827.
- [133] J.E. Huheey, E.A. Keiter, R.L. Keiter, *Anorganische Chemie: Prinzipien von Struktur und Reaktivität*, Walter de Gruyter GmbH, Berlin/Boston, 2014, pp. 579–580.
- [134] H.A. Jahn, E. Teller, *Stability of Polyatomic Molecules in Degenerate Electronic States. I. Orbital Degeneracy*. *Proceedings of the Royal Society of London. Series A, Mathematical and Physical Sciences*, 161 (1937) 220–235.
- [135] L. Liu, J. Xi, Z. Wu, W. Zhang, H. Zhou, W. Li, X. Qiu, *J. Appl. Electrochem.* 42 (2012) 1025–1031.
- [136] W. Zhang, L. Liu, L. Liu, *RSC Adv.* 5 (2015) 100235–100243.
- [137] D.N. Buckley, X. Gao, R.P. Lynch, N. Quill, M.J. Leahy, *J. Electrochem. Soc.* 161 (2014) A524–A534.
- [138] C. Petchsingh, N. Quill, J.T. Joyce, D. Ní Eidhin, D. Oboroceanu, C. Lenihan, X. Gao, R.P. Lynch, D.N. Buckley, *JES* 163 (2016) A5068–A5083.
- [139] N. Quill, C. Petchsingh, R.P. Lynch, X. Gao, D. Oboroceanu, D. Ní Eidhin, M. O'Mahony, C. Lenihan, D.N. Buckley, *ECS Trans.* 64 (2015) 23–39.
- [140] D.N. Buckley, X. Gao, R.P. Lynch, M.J. Leahy, A. Bourke, G. Flynn, *Method for Determining the State of Charge of a Vanadium Redox Flow Battery*, WO 2015/082475 A1, 2015.
- [141] L. Li, Y. Liu, C. Sun, *Method for determining and/or adjusting redox-active element concentrations in redox flow batteries*, US 2015/0303504 A1, 2015.
- [142] S. Helmle, N. Bredemeyer, G. Polcyn, N. Tenhumberg, WO 2018/050547 A1, 2016.
- [143] S. Rudolph, U. Schröder, I.M. Bayanov, K. Blenke, D. Hage, *J. Electroanal. Chem.* 694 (2013) 17–22.

## References

---

- [144] C. Jia, Q. Liu, C.J. Sun, F. Yang, Y. Ren, S.M. Heald, Y. Liu, Z.F. Li, W. Lu, J. Xie, *ACS Appl. Mater. Interfaces* 6 (2014) 17920–17925.
- [145] Y.S. Chou, N.Y. Hsu, K.T. Jeng, K.H. Chen, S.C. Yen, *Appl. Energy* 182 (2016) 253–259.
- [146] A. Mousa, M. Skyllas-Kazacos, Physical properties of negative half-cell electrolytes in the vanadium redox flow battery. *Electrochemically Enabled Sustainability: Devices, Materials and Mechanisms for Energy Conversion*, CRC Press, Boca Raton/FL, 2014, pp. 397–399.
- [147] P. Blanc, C. Madic, J.P. Launay, *Inorg. Chem.* 21 (1982) 2923–2928.
- [148] J. Geiser, H. Natter, R. Hempelmann, B. Morgenstern, K. Hegetschweiler, Photometrical Determination of the State-of-Charge in Vanadium Redox Flow Batteries Part II: In Combination with Open-Circuit-Voltage, *Z. Phys. Chem.* (2019), <https://doi.org/10.1515/zpch-2019-1380>.
- [149] Manufacturer's official website. <https://oceanoptics.com/product/dh-2000-bal/>, 2017 (accessed 02 October 2017).
- [150] A. Ruland, U. Ruland, F. W. Küster, A. Thiel, K. Fischbeck, *Rechentafeln für die Chemische Analytik: Basiswissen für die Analytische Chemie*, 107. Auflage, Walter de Gruyter & Co. KG, Berlin, New York (2011), p. 226.
- [151] K. Rauscher, J. Voigt, I. Wilke, K. T. Wilke, R. Friebe, *Chemische Tabellen und Rechentafeln für die analytische Praxis*, 11. Auflage, Verlag Europa-Lehrmittel, Nourney, Vollmer GmbH & Co. KG, Haan-Gruiten (2000), p. 188.
- [152] R.P. Brooker, C.J. Bell, L.J. Bonville, H.R. Kunz, J.M. Fenton, *J. Electrochem. Soc.* 162 (2015) A608–A613.
- [153] J. Geiser, H. Natter, R. Hempelmann, B. Morgenstern, K. Hegetschweiler, Photometrical Determination of the State-of-Charge in Vanadium Redox Flow Batteries Part I: In Combination with Potentiometric Titration, *Z. Phys. Chem.* (2019), <https://doi.org/10.1515/zpch-2019-1379>.
- [154] L.S.A. Dikshitulu, G.G. Rao, *Talanta* 9 (1962) 857–862.
- [155] K. Sriramam, B.S.R. Sarma, B.S. Sundar, N.R. Sastry, *Talanta* 28 (1981) 287–293.
- [156] G.G. Rao, P.K. Rao, *Talanta* 13 (1966) 1335–1340.
- [157] D. Wang, H.H. Kung, M.A. Barteau, *Appl. Catal. A-Gen.* 201 (2000) 203–213.
- [158] L.S.A. Dikshitulu, G.G. Rao, *Fresen. J. Anal. Chem.* 189 (1962) 421–426.
- [159] G. J. van Kolmeschate, *Handbuch der Analytischen Chemie, Elemente der Fünften Nebengruppe*, Springer-Verlag, Berlin Heidelberg (1957), pp. 1–298.
- [160] J. C. Dobson, M. Sano, H. Taube, *Inorg. Chem.* 30 (1991) 456.

## 8. Appendix

### A. List of figures

Fig. 1. Development of the renewable energy share of the gross electricity consumption in Germany (above), contributions of the miscellaneous renewable sources (below) [3].	2
Fig. 2. Evolution of avoided greenhouse gas emissions by means of renewable energies [3].	3
Fig. 3. EV charging station "OptiCharge" at Saarbrücken/Burbach in Germany [20].	5
Fig. 4. General structure and working principle of a redox flow battery [22].	8
Fig. 5. Schematical set-up of an all-vanadium redox flow battery with expiring redox reactions for the discharging process [24].	11
Fig. 6. Geometrical structures of the vanadium aqua complexes from $V^{2+}$ to $V^{5+}$ . For $V^{2+}$ to $V^{4+}$ octahedrally shaped complexes are obtained. In case of $V^{5+}$ the bipyramidal structure is preferred over the octahedral complex geometry (see second row). The complex structures of $V^{3+}$ to $V^{5+}$ exhibit geometrical distortions from the ideal octahedron of the $V^{2+}$ complex [87-91,95-100].	17
Fig. 7. Exploded-view drawing of the applied VRFB single cell.	32
Fig. 8. Experimental laboratory set-up for the online in-situ absorbance measurements (above) and the corresponding schematical layout (below) [148].	34
Fig. 9. Flow-through supporting cuvette cover incorporating a flow-through cuvette in the assembled state (left); the corresponding exploded-view drawing of the cover (right).	35
Fig. 10. Experimental OCV values (green crosses) plotted versus SOC (determined by Coulomb counting) and fitted with equation (27) shown in red. The measurement uncertainties (and the related error bars) are smaller than the size of the green crosses [148].	40
Fig. 11. Negative half-cell electrolyte (anolyte): In-situ UV/Vis/NIR spectral data as a function of increasing $SOC_{2/3}$ (above) [148] and of decreasing $SOC_{2/3}$ (below).	42
Fig. 12. Negative half-cell electrolyte (anolyte): Linear fit of the measured absorbance values at 400 nm as a function of the negative partial $SOC_{2/3}$ (according to the OCV cell voltage). The measurement uncertainties (error bars) are smaller than the size of the black dots [148].	43
Fig. 13. Negative half-cell electrolyte (anolyte): Trend of the measured absorbance values at 850 nm as a function of the negative partial $SOC_{2/3}$ (according to the OCV cell voltage). The measurement uncertainties are smaller than the size of the black dots.	44
Fig. 14. Positive half-cell electrolyte (catholyte): In-situ UV/Vis/NIR spectral data as a function of increasing $SOC_{4/5}$ (above) [148] and of decreasing $SOC_{4/5}$ (below).	46

Fig. 15. Positive half-cell electrolyte (catholyte): Third order polynomial fit of the measured absorbance values at 440 nm depending on the positive partial SOC <sub>4/5</sub> according to the OCV cell voltage. The measurement uncertainties (error bars) are smaller than the size of the black dots [148].	47
Fig. 16. Scheme for the spectroscopic-coupled potentiometric titration set-up.	51
Fig. 17. Potentiometric titration of a vanadium sample solution with [V <sub>total</sub> ] = 0.2 mol L <sup>-1</sup> (above) and [V <sub>total</sub> ] = 0.4 mol L <sup>-1</sup> (below) using a 0.2 mol L <sup>-1</sup> KMnO <sub>4</sub> titrant solution. At the starting point of the titration process a nominal V <sup>2+</sup> sample solution with mainly V <sup>2+</sup> and a small V <sup>3+</sup> content is applied [153].	53
Fig. 18. Potentiometric titration of a vanadium sample solution with [V <sub>total</sub> ] = 0.6 mol L <sup>-1</sup> (above) and [V <sub>total</sub> ] = 0.8 mol L <sup>-1</sup> (below) using a 0.2 mol L <sup>-1</sup> KMnO <sub>4</sub> titrant solution. At the starting point of the titration process a nominal V <sup>2+</sup> sample solution with mainly V <sup>2+</sup> and a small V <sup>3+</sup> content is applied.	54
Fig. 19. Potentiometric titration of a vanadium sample solution with [V <sub>total</sub> ] = 1.0 mol L <sup>-1</sup> (above) and [V <sub>total</sub> ] = 1.2 mol L <sup>-1</sup> (below) using a 0.2 mol L <sup>-1</sup> KMnO <sub>4</sub> titrant solution. At the starting point of the titration process a nominal V <sup>2+</sup> sample solution with mainly V <sup>2+</sup> and a small V <sup>3+</sup> content is applied.	55
Fig. 20. Potentiometric titration of a vanadium sample solution with [V <sub>total</sub> ] = 1.4 mol L <sup>-1</sup> (above) and [V <sub>total</sub> ] = 1.6 mol L <sup>-1</sup> (below) using a 0.2 mol L <sup>-1</sup> KMnO <sub>4</sub> titrant solution. At the starting point of the titration process a nominal V <sup>2+</sup> sample solution with mainly V <sup>2+</sup> and a small V <sup>3+</sup> content is applied.	56
Fig. 21. Evolution of the UV/Vis/NIR spectral data during the oxidation of V <sup>2+</sup> to V <sup>3+</sup> for an initial total vanadium concentration [V <sub>total</sub> ] = 1.6 mol L <sup>-1</sup> . Four isosbestic points are situated at the wavelengths 330 nm, 470 nm, 620 nm and 690 nm [153].	58
Fig. 22. Evolution of the UV/Vis/NIR spectral data during the oxidation of V <sup>3+</sup> to V <sup>4+</sup> for an initial total vanadium concentration [V <sub>total</sub> ] = 1.6 mol L <sup>-1</sup> . A single isosbestic point is located at 640 nm [153].	58
Fig. 23. Evolution of the UV/Vis/NIR spectral data during the oxidation of V <sup>4+</sup> to V <sup>5+</sup> for an initial total vanadium concentration [V <sub>total</sub> ] = 1.6 mol L <sup>-1</sup> . An isosbestic point does not occur [153].	60
Fig. 24. Evolution of the UV/Vis/NIR spectral data during the oxidation of V <sup>4+</sup> to V <sup>5+</sup> for an initial total vanadium concentration [V <sub>total</sub> ] = 0.2 mol L <sup>-1</sup> . An isosbestic point seems to be existent [153].	60
Fig. 25. Evolution of the UV/Vis/NIR spectral data during the oxidation of V <sup>2+</sup> to V <sup>3+</sup> (top), V <sup>3+</sup> to V <sup>4+</sup> (center) and V <sup>4+</sup> to V <sup>5+</sup> (bottom) for the initial total vanadium concentration [V <sub>total</sub> ] = 0.2 mol L <sup>-1</sup> .	62
Fig. 26. Evolution of the UV/Vis/NIR spectral data during the oxidation of V <sup>2+</sup> to V <sup>3+</sup> (top), V <sup>3+</sup> to V <sup>4+</sup> (center) and V <sup>4+</sup> to V <sup>5+</sup> (bottom) for the initial total vanadium concentration [V <sub>total</sub> ] = 0.4 mol L <sup>-1</sup> .	63
Fig. 27. Evolution of the UV/Vis/NIR spectral data during the oxidation of V <sup>2+</sup> to V <sup>3+</sup> (top), V <sup>3+</sup> to V <sup>4+</sup> (center) and V <sup>4+</sup> to V <sup>5+</sup> (bottom) for the initial total vanadium concentration [V <sub>total</sub> ] = 0.6 mol L <sup>-1</sup> .	64
Fig. 28. Evolution of the UV/Vis/NIR spectral data during the oxidation of V <sup>2+</sup> to V <sup>3+</sup> (top), V <sup>3+</sup> to V <sup>4+</sup> (center) and V <sup>4+</sup> to V <sup>5+</sup> (bottom) for the initial total vanadium concentration [V <sub>total</sub> ] = 0.8 mol L <sup>-1</sup> .	65

---

Fig. 29. Evolution of the UV/Vis/NIR spectral data during the oxidation of $V^{2+}$ to $V^{3+}$ (top), $V^{3+}$ to $V^{4+}$ (center) and $V^{4+}$ to $V^{5+}$ (bottom) for the initial total vanadium concentration $[V_{\text{total}}] = 1.0 \text{ mol L}^{-1}$ . .....	66
Fig. 30. Evolution of the UV/Vis/NIR spectral data during the oxidation of $V^{2+}$ to $V^{3+}$ (top), $V^{3+}$ to $V^{4+}$ (center) and $V^{4+}$ to $V^{5+}$ (bottom) for the initial total vanadium concentration $[V_{\text{total}}] = 1.2 \text{ mol L}^{-1}$ . .....	67
Fig. 31. Evolution of the UV/Vis/NIR spectral data during the oxidation of $V^{2+}$ to $V^{3+}$ (top), $V^{3+}$ to $V^{4+}$ (center) and $V^{4+}$ to $V^{5+}$ (bottom) for the initial total vanadium concentration $[V_{\text{total}}] = 1.4 \text{ mol L}^{-1}$ . .....	68
Fig. 32. Evolution of the UV/Vis/NIR spectral data during the oxidation of $V^{2+}$ to $V^{3+}$ (top), $V^{3+}$ to $V^{4+}$ (center) and $V^{4+}$ to $V^{5+}$ (bottom) for the initial total vanadium concentration $[V_{\text{total}}] = 1.6 \text{ mol L}^{-1}$ . .....	69
Fig. 33. Evolution of the UV/Vis/NIR spectra during the entire oxidation of $V^{2+}$ to $V^{5+}$ for the initial total vanadium concentration $[V_{\text{total}}] = 1.6 \text{ mol L}^{-1}$ as a function of the added volume of $0.2 \text{ mol L}^{-1} \text{ KMnO}_4$ titrant solution. ....	70
Fig. 34. Evolution of the absorbance at 400 nm during the oxidation of $V^{2+}$ to $V^{5+}$ plotted as a function of the dispensed volume of $0.2 \text{ mol L}^{-1} \text{ KMnO}_4$ titrant solution for $[V_{\text{total}}] = 1.6 \text{ mol L}^{-1}$ (black rectangles: experimental data with dilution effect; red circles: experimental data after removal of dilution effect) [153]. .....	72
Fig. 35. Evolution of the absorbance at 850 nm during the oxidation of $V^{2+}$ to $V^{5+}$ plotted as a function of the dispensed volume of $0.2 \text{ mol L}^{-1} \text{ KMnO}_4$ titrant solution for $[V_{\text{total}}] = 1.6 \text{ mol L}^{-1}$ (black rectangles: experimental data with dilution effect; red circles: experimental data after removal of dilution effect) [153]. .....	73
Fig. 36. Pure $V^{2+}$ absorbances at 850 nm (red rectangles) and pure $V^{3+}$ absorbances at 400 nm (black rectangles) as a function of the $V^{2+}$ and $V^{3+}$ concentration, respectively [153]. .....	74
Fig. 37. Absorption coefficients for pure $V^{2+}$ at 850 nm (red rectangles) and pure $V^{3+}$ at 400 nm (black rectangles) as a function of the $V^{2+}$ and $V^{3+}$ concentration, respectively. ....	76
Fig. 38. Comparison of the UV/Vis/NIR data for the analyte based on different calibrations, see chapter 5 [148]. .....	80

---

---

---

## B. List of abbreviations

ABS	absorbance
BMWi	Bundesministerium für Wirtschaft und Energie
BMS	battery management system
CFC	chlorofluorocarbons
EDTA	ethylenediaminetetraacetic acid
EES	electrical energy storage
EMS	energy management system
EV	electric vehicle
GfE	Gesellschaft für Elektrometallurgie mbH
ICP-OES	inductively coupled plasma optical emission spectrometry
IPCC	Intergovernmental Panel on Climate Change
IR	infrared
IZES	Institut für ZukunftsEnergie- und Stoffstromsysteme gGmbH
LED	light-emitting diode
NASA	National Aeronautics and Space Administration
OCP	open-circuit-potential
OCV	open-circuit-voltage
PEMFC	polymer electrolyte membrane fuel cell
PFSA	perfluorosulfonic acid
PtJ	Projektträger Jülich
RFB	redox flow battery
SCHMID	SCHMID Group GmbH – SCHMID Energy Systems GmbH
SOC	(global, overall) state-of-charge
SOC <sub>2/3</sub>	negative partial state-of-charge
SOC <sub>4/5</sub>	positive partial state-of-charge

## List of abbreviations

---

UV/Vis	ultraviolet/visible
UV/Vis/NIR	ultraviolet/visible/near-infrared
VRFB	all-vanadium redox flow battery
XANES	X-ray near-edge absorption spectroscopy

## C. Scientific publications

### Published Papers

J. Geiser, H. Natter, R. Hempelmann, B. Morgenstern, K. Hegetschweiler, Photometrical Determination of the State-of-Charge in Vanadium Redox Flow Batteries Part I: In Combination with Potentiometric Titration, *Z. Phys. Chem.* (2019), <https://doi.org/10.1515/zpch-2019-1379>.

J. Geiser, H. Natter, R. Hempelmann, B. Morgenstern, K. Hegetschweiler, Photometrical Determination of the State-of-Charge in Vanadium Redox Flow Batteries Part II: In Combination with Open-Circuit-Voltage, *Z. Phys. Chem.* (2019), <https://doi.org/10.1515/zpch-2019-1380>.

### Oral presentations

J. Geiser, K. Weißhaar, H. Natter, R. Hempelmann, B. Groß, S. Schulte, J. Langner, I. Derr, D. Görges, T. Lepold, Fotovoltaik + Vanadium-Redox-Flow-Batterie: autark, regenerativ betriebene Stromparkplätze, Jahrestreffen der ProcessNet-Fachgruppe Energieverfahrenstechnik (2018), Frankfurt am Main (Germany).

J. Geiser, H. Natter, R. Hempelmann, B. Morgenstern, K. Hegetschweiler, Entwicklung eines neuartigen State-of-Charge-Indikators für die Vanadium-Redox-Flow-Batterie, Aktionswoche „Das Saarland voller Energie“ (2017), IZES gGmbH Saarbrücken (Germany).

### Poster presentations

J. Geiser, H. Natter, R. Hempelmann, B. Morgenstern, K. Hegetschweiler, Investigations on an improved state-of-charge indicator for the all-vanadium redox flow battery, Bunsentagung (2018), Hannover (Germany).

J. Geiser, H. Natter, B. Morgenstern, R. Hempelmann, Investigations on an improved state-of-charge indicator for the all-vanadium redox flow battery, GDCh-Wissenschaftsforum Chemie (2017), Berlin (Germany).

J. Geiser, H. Natter, B. Morgenstern, R. Hempelmann, Investigations on an improved state-of-charge indicator for the all-vanadium redox flow battery, Bunsentagung (2017), Kaiserslautern (Germany).

J. Geiser, H. Natter, R. Hempelmann, Investigations on an improved state-of-charge indicator for the all-vanadium redox flow battery, *Electrochemistry* (2016), Goslar (Germany).

J. Geiser, H. Natter, R. Hempelmann, Development of an improved state-of-charge indicator for the all-vanadium redox flow battery, Bunsentagung (2016), Rostock (Germany).



## Acknowledgements

Finally, particular thanks are due to everyone who made an essential contribution to the success of this PhD thesis and provided scientific advice and support.

I would like to express my special thanks to:

Prof. Dr. Dr. h. c. Rolf Hempelmann for the highly topical and particularly interesting research subject, his appreciated guidance and support, his valuable suggestions and impulses during this entire PhD study as well as the opportunity to present my scientific results on several international conferences and in peer-review journal articles.

Prof. Dr. Michael Springborg for taking over the second examination.

Prof. Dr. Kaspar Hegetschweiler for generous provision of his laboratory work spaces, measuring equipment and chemicals as well as for the fruitful discussions.

PD Dr. Harald Natter for his support and valued advices in the course of this thesis.

Dr. Bernd Morgenstern for the introduction in his measuring equipment and the important discussions about the measurement results.

all project partners for the productive and collegial cooperation within the BMWi-funded project "OptiCharge", our beneficial exchange of knowledge and the related interesting insights in their research, in particular:

Dr. Bodo Groß, M. Sc. Stephan Schulte and M. Sc. Alexander Berhardt from IZES gGmbH,

Dr. Joachim Langner, Dr. Igor Derr, Dr. Melanie Schröder, Dr. Hannes Barsch, Dipl. Ing. Peter Schauer and Dipl. Chem. Christian Fuhrmann from SCHMID Energy Systems GmbH,

as well as Prof. Dr. Daniel Görge and Dipl. Ing. Tobias Lepold from the Technical University of Kaiserslautern.

M. Sc. Roland Serwas and Dipl. Ing. Susanne Neurohr for their help and technical support.

Dipl. Ing. Rudolf Richter and the complete mechanical workshop staff, particularly Jens Wiegert for the design engineering and the construction of several parts for my measurement set-ups.

all members of the research group of Prof. Dr. Dr. h. c. Rolf Hempelmann for the excellent and productive working atmosphere, especially: Dr. Ruiyong Chen, Dr. Sangwon Kim, Dr. Dan Durneata, Dipl. Chem. Daniel Rauber, Dipl. Chem. Dina Klippert, M. Sc. Zhenzhen Wang, M. Sc. Yonglai Zhang, M. Sc. Zhifeng Huang, Dr. Konstantin Weißhaar, M. Sc. Angelo Stephan and M. Sc. Nils-Frederik Schumacher.

my parents, my grandparents and the whole family for their unlimited and highly esteemed support and caring.

## Acknowledgements

---